Kinematic partitioning of deformation in the Southern Andes inferred from remote sensing, thermochronology, scaled analogue modelling, and field observations

Dissertation

with the aim of achieving a doctoral degree

at the Faculty of Mathematics, Informatics and Natural Sciences

Department of Earth Sciences

at Universität Hamburg

Submitted by Paul Leon Göllner

from Kassel, Germany

Hamburg, 2021

Accepted as Dissertation at the Department of Earth Sciences

Day of oral defense:	28.04.2021
Reviewers:	Prof. Dr. Ulrich Riller
	Dr. Matthias Rosenau
Chair of the Subject Doctoral Committee:	Prof. Dr. Dirk Gajewski
Dean of Faculty of MIN:	Prof. Dr. Heinrich Graener

Abstract

Upper-plate deformation along the Southern Andean obliquely convergent plate margin is perceived to be kinematically partitioned into margin-normal shortening accommodated in the forearc and margin-parallel strike-slip in the arc-region. Here, margin-parallel strike-slip is mainly attributed to the margin-parallel Liquiñe-Ofqui fault zone (LOFZ) which is interpreted to northwardly displace a portion of the forearc. In light of recent studies providing evidence for intra-arc displacement on, notably, margin oblique faults, this thesis revisits deformation and kinematic partitioning in the Southern Andes with an integrated approach involving remote sensing, reassessment of exhumation rates, analogue modelling, and field-based study of dikes.

Morphological lineaments extracted from digital elevation models of the Southern Andes, corroborated by mapped faults provide evidence for distributed deformation in the Southern Andes on a network of predominately NW-, NE-, and N-S-striking faults. Exhumation rates, calculated from published apatite fission track and (U-Th)/He ages, show Miocene to Pliocene maximal exhumation in the central portion of the Southern Andes. Changes in exhumation rate across extracted lineaments indicate vertical offset along first-order margin-parallel and -oblique faults. Contrary to pure strike-slip attributed to the Southern Andes, these observations provide evidence for distributed transpressive deformation with the maximal vertical extrusion of rocks in the arc-region.

Analogue models simulating deformation in the Southern Andes indicate an evolution in intra-arc deformation in an early phase defined by reverse faults oriented perpendicular to the convergence vector and a late phase characterized by reverse displacement on margin-parallel faults. In contrast to proposed northward translation of a rigid forearc-portion along the LOFZ, model results corroborated by fault-slip data provide evidence for northward displacement of crust on an intra-arc dextral transpressive zone involving clockwise rotation of upper crust, sinistral-reverse displacement on WNW-striking faults, and reverse displacement on N-S-striking faults.

Trace-element ratios of Pliocene to Pleistocene dikes located at the northern terminus of the LOFZ are consistent with proposed late Miocene to Pliocene slab-steepening and resulting crustal extension along the eastern flank of the Southern Andes. Conversely, roughly E-W-oriented maximum compressive stress-axes (σ_{1H}) inferred from dike trends, consistent with arc-orthogonal compression, indicate that Miocene to Pliocene changes in the subduction geometry did not result in a reorientation of σ_{1H}-axes.

Zusammenfassung

Die Deformation entlang des schief konvergenten Kontinentalrandes der Südanden wird als kinematisch partitioniert beschrieben. Hier soll kontinentalrand-orthogonale Einengung im Forearc-Bereich und Kontinentalrand-parallele Horizontalverschiebung hauptsächlich durch die Liquiñe-Ofqui Störungszone (englisch Liquiñe-Ofqui fault zone, kurz LOFZ) aufgenommen werden, welche einen Teil des Forearc in nördlicher Richtung verschieben soll. Neueste Forschungsergebnisse liefern hingegen Hinweise auf Horizontal-verschiebung innerhalb des vulkanischen Bogens entlang von Störungen mit schiefer Ausrichtung zum Kontinentalrand. In Anbetracht dieser Ergebnisse, ist das Ziel dieser Arbeit die erneute Untersuchung der kinematischen Partitionierung der Deformation in den Südanden mit Hilfe von Fernerkundung, Neubewertung von Exhumierungsraten, Analogmodellierung und der Untersuchung von magmatischen Gängen.

Morphologische Lineamente, die auf digitalen Höhenmodellen der Südanden identifieziert und durch kartierte Störungen bestätigt werden, liefern Hinweise auf verteilte Deformation in den Südanden entlang eines Netzwerkes aus NW- NE- und N-S-streichenden Störungen. Aus publizierten Apatit fission track- und (U/Th)/He-Altern errechnete Exhumierungsraten zeigen eine maximale miozäne bis pliozäne Exhumierung im Zentrum der Südanden. Veränderungen der Exhumierungsrate über identifizierte Lineamente deuten hier auf einen vertikalen Versatz entlang von Störungen erster Ordnung mit Kontinentalrand-paralleler und schiefer Orientierung zum Kontinentalrand hin. Im Gegensatz zu reiner Horizontal-verschiebung innerhalb der Südanden liefern diese Ergebnisse Hinweise auf eine verteilte, transpressive Deformation des magmatischen Bogens.

Simulationen der Deformation in den Südanden mittels skalierter Analogmodelle zeigen die Entwicklung von Deformation innerhalb des magmatischen Bogens von einer initialen Phase, definiert durch Aufschiebungen mit einer orthogonalen Ausrichtung zum Konvergenzvektor, zu einer späten Phase, charakterisiert durch kontinentalrand-parallele Aufschiebungen. Entgegen der verbreiteten Annahme von nordwärts gerichteter Translation eines rigiden Forearc-Teils entlang der LOFZ,

liefern Ergebnisse der Analogmodelle, unterstützt von Störungsflächen-Analysen, Hinweise auf eine nordwertige Verschiebung von Erdkruste entlang einer dextralen transpressiven Zone mit Hilfe der Rotation von Erdkruste im Uhrzeigersinn, WNW-streichenden sinistralen schiefen Aufschiebungen und N-S-streichenden Aufschiebungen.

Spurenelement-Verhältnisse pliozäner bis pleistozäner magmatischer Gänge am nördlichen Ende der LOFZ stimmen mit einer angenommenen miozänen bis pliozänen Steigerung des Winkels der subduzierten Platte und der daraus resultierenden Extension der Oberkruste überein. Eine circa E-W-orientierte Achse der maximalen horizontalen Hauptspannung (σ_{1H}), abgeleitet von der Orientierung magmatischer Gänge weist hingegen auf eine Kompression orthogonal zum magmatischen Bogen hin. Folglich haben miozäne bis pliozäne Änderungen der Subduktionszonen-Geometrie nicht zu einer Reorientierung der σ_{1H}-Achse geführt.

Table of Contents

List of derived publications

Göllner P, Eisermann JO, Balbis C, Petrinovic IA, Riller U, Kinematic partitioning in the Southern Andes (39°S - 46°S) inferred from lineament analysis and reassessment of exhumation rates. International Journal of Earth Sciences (in review)

Göllner P, Eisermann JO, Rosenau M, Galland O, Riller U, Revisiting the sliver hypothesis of kinematic partitioning at the Southern Andean obliquely convergent margin (in preparation for submission to Geology)

Göllner P, Eisermann JO, Jung S, Petrinovic IA, Riller U, Constraints on the Plio-Pleistocene stress field and regional volcanism from dikes surrounding the Copahue Caviahue volcanic complex, Andean Southern Volcanic Zone (in preparation)

1 Introduction

The development of the theory of plate tectonics represents one of the major scientific achievements of the 20th century. Even though the initial proposal of continental drift by Alfred Wegener (1912) was rejected by the scientific community due to a lack of plausible driving-forces, the theory of rigid lithospheric plates drifting on the mechanically weaker asthenosphere gained acceptance after the discovery of seafloor spreading as a driving factor for plate motion (Dietz, 1961; Hess, 1962; Vine and Matthews, 1963). Now, several decades later, we know that the solid outer layer of our planet consists of 14 major plates and a growing number of newly identified microplates moving across Earth's surface (Fig. 1.1; Bird, 2003; DeMets et al., 2010). Aside from seafloor spreading, which describes the rise of magma at oceanic ridges, pushing lithospheric plates apart, the slab-pull force of sinking oceanic crust into the asthenosphere and drag forces at the lithosphere-asthenosphere boundary are viewed as the main drivers of plate motion (Forsyth and Uyeda, 1975; Richardson, 1992). Based on the relative motion of plates with respect to each other, three types of plate boundaries are defined: Divergent plate boundaries are characterized by two plates drifting away from each other producing new crustal material. Transform margins describe plate boundaries where adjacent plates slide past each other. Plate margins where two plates move towards each other are termed convergent margins. Most convergent plate margins are associated with a destruction of crustal material through subduction.

A subduction zone is a convergent plate boundary characterized by the sinking of mostly oceanic lithosphere beneath a continental or oceanic plate (Fig. 1.2a; Stern, 2002). With increasing temperature and pressure, the sinking lithosphere, referred to as subducting slab, releases volatiles and fluids which lead to melting of the overlying asthenosphere. The generated melts cause extensive volcanism in the overriding (upper) plate which commonly results in the formation of a volcanic arc trending parallel to the plate boundary (Fig. 1.2a). Additionally, major earthquakes are concentrated at subduction zones (Heaton and Hartzell, 1987; Bilek, 2010; Wang et al., 2012). Here, friction between the upper and subducted plate have induced some of the strongest recorded earthquakes such as the M_w 9.5 Valdivia

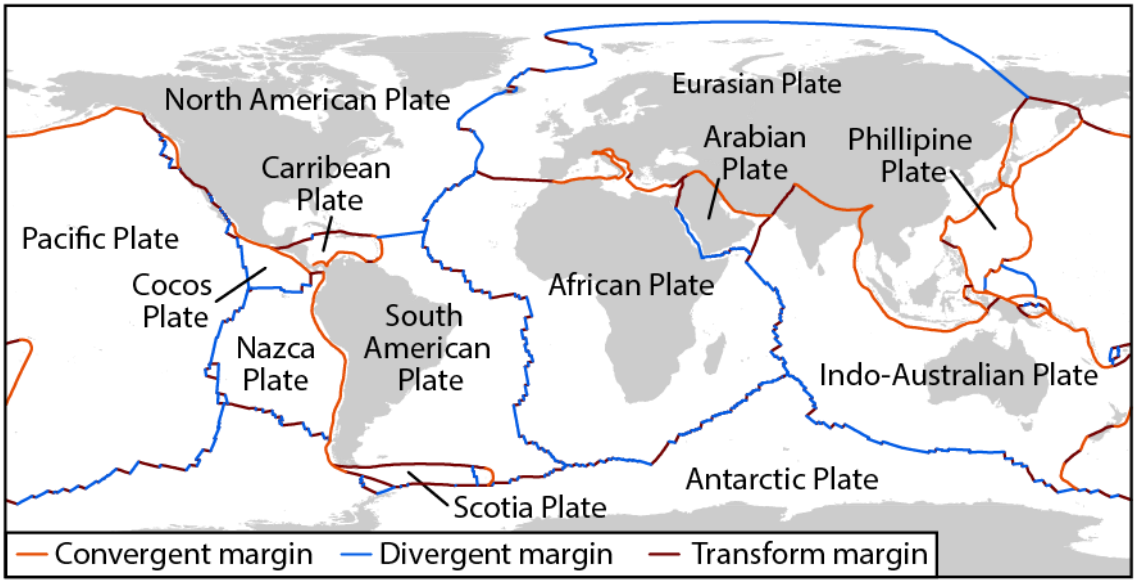

Figure 1.1: Major lithospheric plates and plate boundaries. Simplified after Bird (2003).

earthquake which recorded in southern Chile in 1960 (Plafker and Savage, 1970; Barrientos and Ward, 1990). The dynamics of subduction systems are influenced by a variety of factors such as the age of subducted lithosphere, relative plate velocities and mechanical properties of the subducted slab (Jarrard, 1986; Stern, 2002; Ramos, 2010). As a result, subduction zones show great variation with respect to their geometry and the deformation of the upper plate.

The age of the subducted lithosphere is often regarded as the prime factor controlling the geometry of subduction zones (Jarrard, 1986; Stern, 2002). Subduction of old, less buoyant lithosphere is interpreted to result in a steep dip of the subducting slab (>30°) whereas the subduction of young and relatively buoyant lithosphere apparently results in shallower subduction angles (<30°). Conversely, Lallemmand et al. (2005) demonstrate the slab-dip controlled by the absolute motion of the upper plate. According to the latter study, advancing upper plates towards the subduction interface result in shallow subduction angles while retreating upper plates are associated with steeper subduction angles. In addition to these primary controlling factors, the subduction angle may be influenced by the subduction of domains of increased buoyancy within the subducted slab such as intraplate island-seamounts and oceanic plateaus (Cross and Pilger, 1982; Gutscher et al., 1999; Gutscher, 2002). Here, subduction of highly buoyant slabs is interpreted to result in a subhorizontal angle of subduction which is commonly referred to as flat slab subduction (Gutscher et al., 2000; Gutscher, 2002; Ramos

and Folguera, 2009). Flat slab subduction zones are accompanied by a cessation of volcanic activity as the subducted slab remains at shallower depth underneath the overriding plate before finally descending into the asthenosphere, thus preventing melting of the asthenosphere.

Based on deformation within the upper plate, Jarrard (1986) classified subduction zones in seven strain classes. Strain classes form a continuum from strongly extensional to strongly compressional. Strongly extensional subduction zones, termed Mariana type, are characterized by extension within the upper plate resulting in the crustal attenuation on the far side of volcanic arcs which may culminate in the formation of back-arc basins. Strongly compressional subduction zones, termed Chile type, are characterized by pervasive shortening of the upper plate producing a mountain chain parallel to the plate interface, termed subduction orogen.

Deformation within the upper plate is controlled by a variety of factors. Among others, the shear coupling between the subducting and the upper plate, the length of the mechanically coupled plate interface, the rate of plate-convergence, the dip of the subducting slab, the direction of flow in the underlying mantle, and the absolute motion of the upper plate are discussed (Jarrard, 1986; Sobolev and Babeyko, 2005; Oncken et al., 2006; Doglioni et al., 2007; Ramos, 2010). Among those, the absolute motion of the upper plate is regarded as the primary factor controlling upper-plate deformation (Jarrard, 1986; Heuret and Lallemand, 2005; Oncken et al., 2006).

Aside from the aforementioned factors, which mainly govern extension or shortening, upper-plate deformation is also influenced by the angle at which the downgoing slab is subducted with respect to the plate interface. At numerous subduction zones, subduction occurs at an oblique angle. The obliquity of a subduction zone is described by the angle between the convergence vector of both plates, and the normal to the plate interface, commonly referred to as obliquity angle (Fig. 1.2b). Upper-plate deformation imparted through oblique subduction may be simply resolved through oblique slip at the plate interface, or through a kinematic partitioning of deformation, commonly termed strain partitioning (e. g. Fitch, 1972; Beck, 1983; Jarrard, 1986; Beck, 1991). At kinematically partitioned

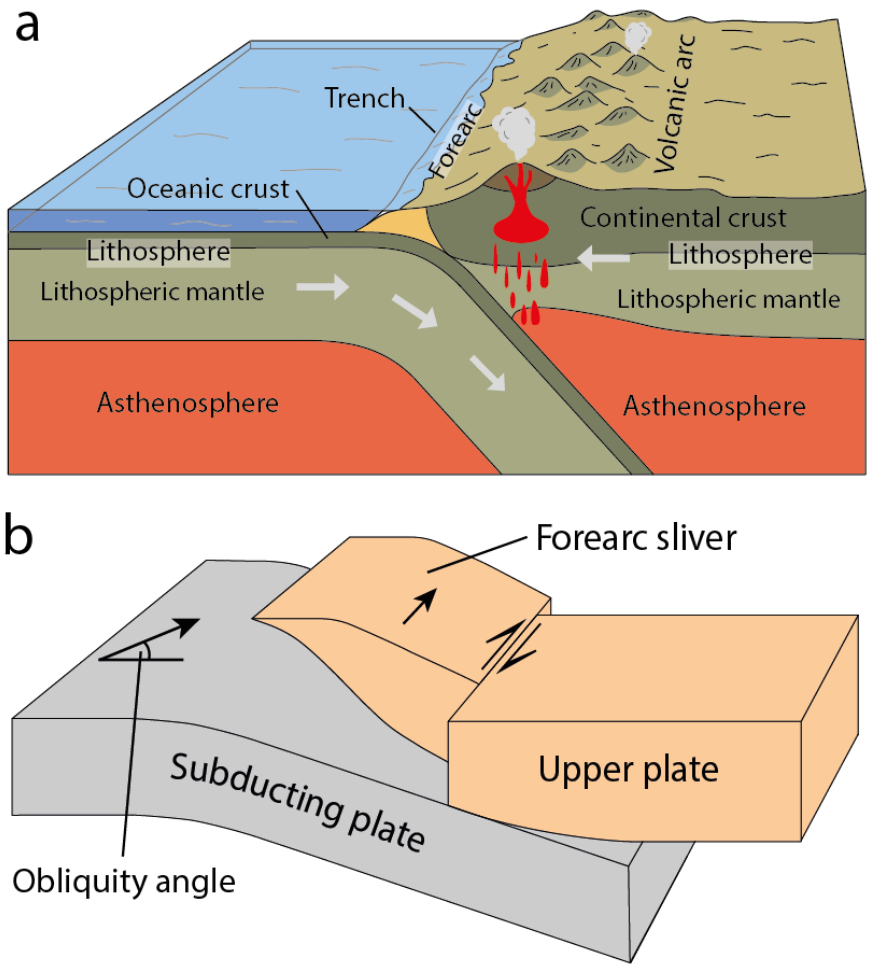

Figure 1.2: Schematic illustration of a subduction zone. (a) Simplified block diagram. (b) Tectonic model of deformation partitioning at obliquely convergent plate margins.

subduction zones, oblique convergence is interpreted to be resolved through margin-orthogonal slip at the plate interface and arc parallel displacement within the upper plate resolving the margin-parallel component of oblique convergence (Fig. 1.2b; McCaffrey, 1992; Chemenda et al., 2000). Arc-parallel slip is thereby interpreted to result in the displacement of a frontal portion of the upper plate, termed forearc-sliver (Jarrard, 1986; Beck, 1991; Nocquet et al., 2014).

Over the past decades, deformation partitioning at obliquely convergent subduction zones has been subject of numerous studies (e. g. Fitch, 1972; Jarrard, 1986; Beck, 1991; McCaffrey, 1992; Beck et al., 1993; McCaffrey et al., 2000; Hoffmann-Rothe et al., 2006). Most attention has thereby been paid to the governing factors controlling partitioning. In this regard, studies of the plate kinematic parameters at obliquely convergent margins lead Jarrard (1986) to

propose plate coupling at the subduction interface as the main controlling factor of deformation partitioning. Based on slip vector modelling, McCaffrey (1992) demonstrated the importance of the obliquity angle as primary controlling factor. Finally, Chemenda et al. (2000) and Hoffmann-Rothe et al. (2006) emphasized the importance of mechanical weakening of the upper plate.

Despite decades of research, the mechanism by which the margin-parallel slip is accommodated in the upper plate is still subject of debate. The traditional model of deformation partitioning focusses on major margin-parallel fault zones such as the Great Sumatra fault in Indonesia (McCaffrey, 1992; McCaffrey et al., 2000) or the Liquiñe-Ofqui fault zone in Chile (Cembrano et al., 1996; Lavenu and Cembrano, 1999) accommodating the majority of margin-parallel slip (Cembrano et al., 1996; McCaffrey et al., 2000; Hoffmann-Rothe et al., 2006). Beck (1993), however, recognized a space problem occurring at the leading edge of fore-arc slivers during margin-parallel displacement on a single margin-parallel fault zone. The so-called "buttressing effect" should hamper or inhibit fore-arc sliver translation at linear or concave convergent margins, resulting in arc-parallel shortening (Wang, 1996) which is not accounted for in the traditional model of deformation partitioning.

The western margin of South America provides ideal conditions to study the kinematic partitioning of deformation at obliquely convergent plate margins. Here, subduction of the Nazca Plate, a segment of the former Farallon Plate, at velocities of around 5-7 cm/a occurs at oblique angles along most of the plate margin (Fig. 1.3; Dewey and Lamb, 1992; Somoza et al., 1998; Stern, 2004; Somoza and Ghidella, 2012; Chen et al., 2019). Continuous subduction of the Nazca Plate, during the Mesozoic and Cenozoic, has resulted in the formation of the Andean mountains. Stretching along the western margin of South America for over 8000 km with a maximum elevation above 7000 m, the Andes are the longest and second highest mountain chain on Earth (Ramos, 1999; Stern, 2004). Based on plate tectonic factors, geology, topography, and crustal parameters, several studies attempt a segmentation of the Andes into various subdivisions (e. g. Gansser, 1973; Ramos, 1999; Tassara and Yáñez, 2003; Ramos, 2009; Folguera et al., 2016). On the basis of topography and crustal parameters, a commonly accepted segmentation divides the Andes into four segments (Fig. 1.3; Tassara and Yáñez, 2003): The Northern (5° N to 15°S), Central (15°S to 33°S), Southern (33°S to 47°S), and Austral Andes (47°S to

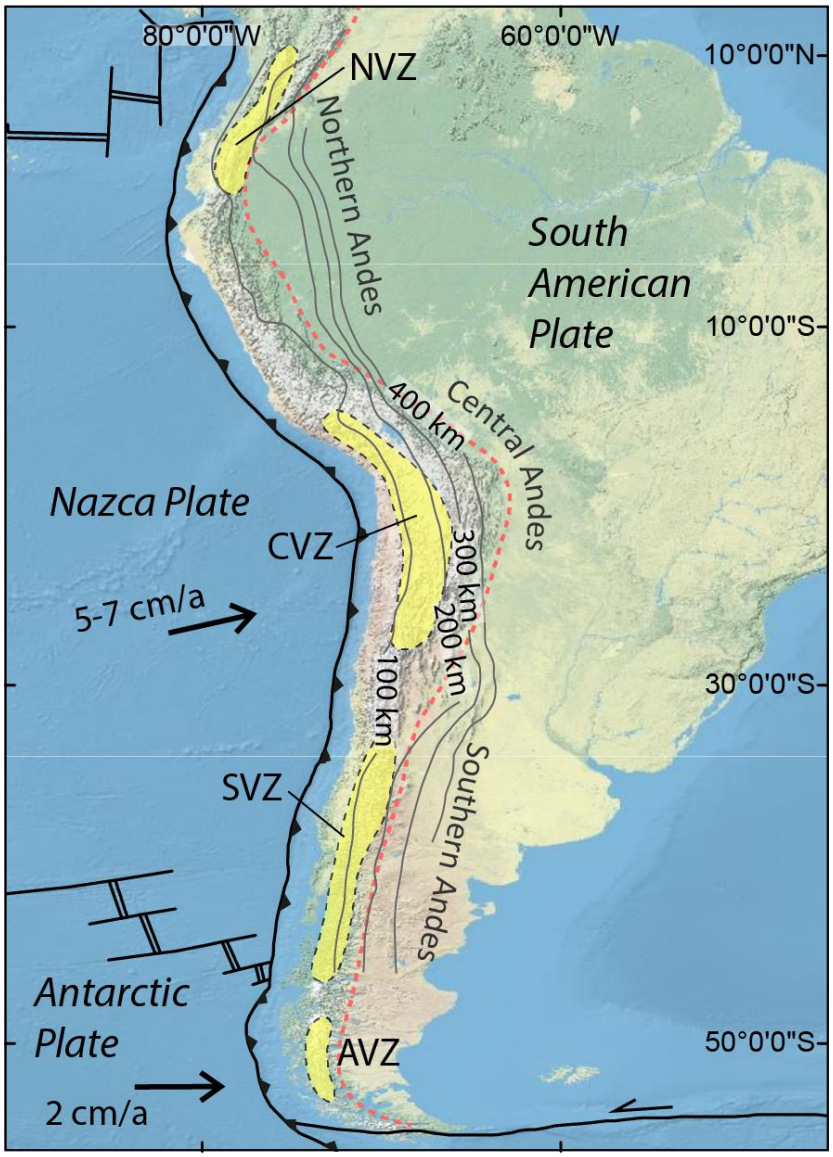

Figure 1.3: Tectonic setting of South America. Grey lines indicate depth contour of the subducting Nazca Plate (modified after Tassara et al. 2006 and Hayes et al. 2012). Red dashed line marks the eastern boundary of the Andes. NVZ: Northern Volcanic Zone, CVZ: Central Volcanic Zone, SVZ: Southern Volcanic Zone, AVZ: Austral Volcanic Zone.

57°S). Tectonic studies of the Southern Andes thereby invoke a Central to Southern Andean transition zone between 33°S and around 39°S (e. g. Rojas Vera et al., 2016; Horton, 2018). Volcanic activity along the Andes is concentrated in four volcanic zones (Fig. 1.3) termed Northern (5°N to 2°S), Central (16°S to 26°S), Southern (34°S to 46°S), and Austral Volcanic Zone (south of 47°S; Ramos, 1999; Stern, 2002, 2004). Gaps between the four volcanic zones coincide with the Peruvian and Pampean flat

slab segments and the subduction of the Chile Ridge, the active spreading center between the Nazca and Antarctic Plates (Fig. 1.3).

Since the Mesozoic, kinematic partitioning of deformation along the western margin of South America has allegedly resulted in the detachment and translation of several fore-arc domains on major arc-parallel strike-slip faults (Dewey and Lamb, 1992; Cembrano et al., 1996; Reutter et al., 1996; Tomlinson and Blanco, 1997; Scheuber and González, 1996; Brooks et al., 2003; Cembrano et al., 2005; Hoffmann-Rothe et al., 2006; Wang et al., 2008; Noquet et al., 2014). Particularly, the Southern Andes of Chile and Argentina are often regarded as a prime example of deformation partitioning (Cembrano et al., 1996, 2000; Rosenau, 2004; Rosenau et al., 2006; Lange et al., 2008).

With a mean elevation around 1000 m and an across-strike width of about 300 km, the Southern Andes are narrow and characterized by decreased elevation compared to the broad (800 km across-strike width) and elevated (mean elevation >3000 m) Central Andes. Similar to orogen-width and elevation, the crustal thickness deceases southward from a maximum of 70 km below the Central Andes to an average thickness of 40 km below the Southern Andes (Bohm et al., 2002; Tassara et al., 2006; Heit et al., 2008; Assumpção et al., 2013). The plate tectonic setting along the Southern Andes (39°S to 47°S) is characterized by subduction of the Nazca Plate at an inclination of roughly 30° with a velocity of 66 mm/yr in N80°E direction, corresponding to an obliquity angle of 20° (Fig. 1.4; Pardo-Casas and Molnar, 1987; Angermann et al., 1999; Bohm et al., 2002). south of the Chile Triple Junction, the Antarctic Plate is subducted orthogonal to the plate margin at 20 mm/a (Fig. 1.4; Cande and Leslie, 1986; Gripp and Gordon, 1990; DeMets et al., 1994; Breitsprecher and Thorkelson, 2009). Despite an overall decrease in convergence rate and a northward migration of the Chile Triple Junction, this plate tectonic setup has remained constant for the past 25 Ma (Pardo-Casas and Molnar, 1987; Somoza, 1998; Somoza and Ghidella, 2012).

The onshore region of the Southern Andean plate margin is generally subdivided into four roughly margin-parallel morphotectonic units (Fig. 1.4): The Coastal Cordillera, the Central Depression or Longitudinal Valley, the Main Cordillera, and the Argentinian Basement. The elevated mountains of the Coastal Cordillera are composed of high-pressure/low-temperature metamorphic rocks of the so-called

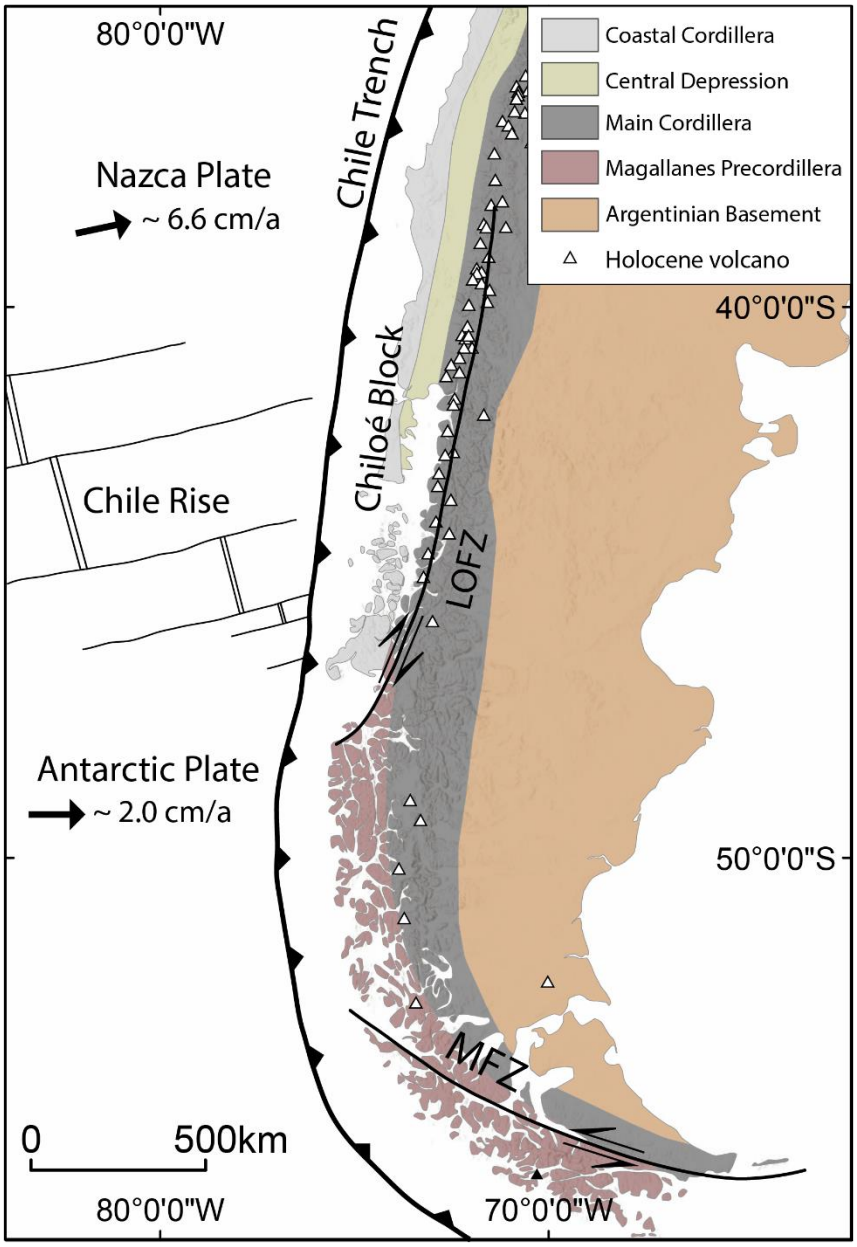

Figure 1.4: Tectonic setting and morphotectonic units of the Southern and Austral Andes (after Lavenu and Cembrano, 1999).

Western Series, interpreted as a former accretionary wedge (Aguirre et al., 1972; Wilner et al., 2003; Willner et al., 2004) and low-pressure/high-temperature metamorphic rocks of the Easter Series, which resemble a relic magmatic arc (Martin et al., 1999; Wilner et al., 2000). NW-SE-striking faults, interpreted as of pre-Andean origin cut the Coastal Cordillera (Glodny et al., 2008; Melnick et al., 2009). An arc-parallel depression between the Coastal Cordillera and the Main Cordillera marks the Central Depression which represents a Paleogene to

Quaternary extensional basin composed of volcano-sedimentary rocks (Stern et al., 2000; Jordan et al., 2001; Encinas et al., 2020). The Main Cordillera, located East of the Central Depression (Fig. 1.4), hosts the present-day volcanic arc, which emplaced above Jurassic to Neogene plutonic rocks of the Patagonian Batholith (Pankhurst et al., 1992, 1999; Hervé et al., 2007). North of 39°S and along its eastern slope, the Main Cordillera is composed of Paleogene to Pleistocene sedimentary, volcanic and volcano-sedimentary rocks (Jordan et al., 2001; Burns et al., 2006; Bechis et al., 2014).

Neogene deformation along the Southern Andes is mainly focused on the Coastal and Main Cordillera. Based on syn-tectonic strata, mountain building in the Main Cordillera is attributed to two compressional phases during the late Cretaceous and the late Miocene (Orts et al., 2012, 2015; Echaurren et al., 2016). The latter phase corresponds to enhanced exhumation recorded within the Southern Andes (Thomson, 2002). Along the Eastern slope of the Main Cordillera, Cretaceous to Neogene inversion of sedimentary basins resulted in the formation of the NNW-SSE-trending North Patagonian fold-and-thrust belt which is mainly composed of E- to NE-vergent thrust faults (Diraison et al., 1998; Giacosa and Heredia, 2004; Orts et al., 2012). Based on deformed sedimentary strata, the fold-and-thrust belt is divided into a western series developed in pre-tertiary rocks and an eastern series deforming Tertiary strata (Giacosa and Heredia, 2004). The volcanic arc in the center of the Main Cordillera hosts the Liquiñe-Ofqui Fault Zone, one of the most prominent intra-arc fault zones on Earth (LOFZ; Hervé, 1976; Cembrano et al., 1996, 2000, 2002; Rosenau et al., 2006). The LOFZ stretches from the current position of the Chile Triple Junction to the Malargüe fold-and-thrust belt in the Southern Central Transition Zone (Fig. 1.4). Initially, this fault zone was described as two prominent N-S- to NNE-trending lineaments, connected through numerous stepover faults (Hervé, 1976; Cembrano et al., 1996). Based on the tectonic setting, the LOFZ has been interpreted to solely accommodate margin-parallel slip resulting from partitioned deformation along the Southern Andes which led to the dislocation and northward translation of a crustal sliver, termed Cholié Block (Fig. 1.4; Cembrano et al., 1996, 2000; Rosenau et al., 2006). In accordance with the obliquity of convergence, dextral strike-slip displacement has been initially attributed to the LOFZ (Hervé, 1976; Cembrano et al., 1996). Recent structural studies are however at odds with this simple concept of kinematic partitioning at the Southern Andes: Fault-slip kinematic studies (Lavenu and Cembrano, 1999;

Cembrano et al., 2002; Lara et al., 2008) and thermochronological studies (Thomson, 2002; Adirasola et al., 2005) document vertical displacement along major faults in the Southern Andes, including the LOFZ. Additionally, Rosenau et al. (2006), Stanton-Yonge et al. (2016), and Sielfeld et al. (2019a, b) provide evidence for deformation of the outhern Andean Main Cordillera involving major NE- and NW- striking faults aside from the main LOFZ.

In light of previous studies addressing deformation in the Southern Andes, goal of this thesis is to revisit kinematic partitioning of deformation in the Southern Andes. With an integrated approach involving remote sensing, the reassessment of exhumation rates, and analogue modelling the attempt is made to investigate the development, overall distribution, and kinematics of major faults in the Southern Andes. Additionally, field-based study of dikes at the northern terminus of the LOFZ is used to examine the Neogene upper-crustal stress field.

1.1 Outline of this thesis

Chapter 2 of this thesis addresses intra-arc deformation in the Southern Andes by means of lineament analysis and a reassessment of low-temperature thermochronology data. In accordance with recent studies of Southern Andean deformation, it is shown that NE, N-S, and NW-trending lineaments demarcating the trace of major faults, cut the Southern Andean Main Cordillera between 39°S and 46°S. On the basis of exhumation rates calculated from apatite fission track and apatite (U-Th)/He ages, maximal exhumation in the central parts of the orogen is illustrated. Here, spatial coincidence of discontinuities with gradients in Neogene exhumation rate are used to infer vertical displacement on faults striking parallel to major lineaments. Based on result of this chapter, in agreement with Neogene shortening in the Southern Andes, a tectonic model involving orogen-wide transpression with maximal vertical extrusion of rocks in the center of the transpression zone is proposed.

In Chapter 3, the hypothesis of pure margin-parallel displacement in the Southern Andes resolved on the LOFZ is investigated based on results of scaled analogue experiments. Analogue models simulating deformation along the Southern Andean plate margin show the development of intra-arc deformation in an early

phase, characterized by the formation of reverse faults perpendicular to the plate convergence vector, followed by a late phase defined by margin-parallel reverse faults. Contrary to northward translation of a rigid forearc-portion, northward displacement of crust through clockwise rotation, margin-oblique sinistral-reverse faults, and margin-parallel dextral-reverse faults, collectively forming an intra-arc transpressive zone is proposed based on kinematic and structural similarities between analogue models and the Southern Andes.

Chapter 4 addresses the emplacement of Pliocene to Pleistocene dikes at the northern terminus of the LOFZ. On the basis of trace element ratios of dikes associated with the Copahue Caviahue volcanic complex (CCVC) a decrease in the degree of mantle melting interpreted as evidence for reduced slab-derived fluid flux coeval with proposed Miocene to Pliocene slab-steepening is inferred. Trends of dikes surrounding the CCVC are used to infer the orientation of the maximum horizontal compressive stress-axes. Based on roughly constant Miocene to present E-W-oriented maximal horizontal compression, it is demonstrated that proposed Miocene to Pliocene transition from upper crustal compression to extension was likely accomplished through transition in the orientation of the minimal compressive stress-axis from vertical to horizontal.

2 Kinematic partitioning in the Southern Andes (39°S - 46°S) inferred from lineament analysis and reassessment of exhumation rates

2.1 Abstract

The Southern Andes are often viewed as a classic example for kinematic partitioning of oblique plate convergence into components of continental margin-parallel strike-slip and transverse shortening. In this regard, the Liquiñe-Ofqui Fault Zone, one of Earth's most prominent intra-arc deformation zones, is believed to be the most important crustal discontinuity in the Southern Andes taking up margin-parallel dextral strike-slip. Recent structural studies, however, are at odds with this simple concept of kinematic partitioning, due to the presence of margin-oblique and a number of other margin-parallel intra-arc deformation zones. However, knowledge on the extent of such zones in the Southern Andes is still limited. Here, we document traces of prominent structural discontinuities (lineaments) from the Southern Andes between 39°S and 46°S. In combination with compiled low-temperature thermochronology data and interpolation of respective exhumation rates, we revisit the issue of kinematic partitioning in the Southern Andes. Exhumation rates are maximal in the central parts of the orogen and discontinuity traces, trending predominantly N-S, WNW-ESE and NE-SW, are distributed across the entire width of the orogen. Notably, discontinuities coincide spatially with large gradients in Neogene exhumation rates and separate crustal domains characterized by uniform exhumation. Collectively, these relationships point to significant components of vertical displacement on these discontinuities, in addition to horizontal displacements known from published structural studies. Our results agree with previously documented Neogene shortening in the Southern Andes and indicate orogen-scale transpression with maximal vertical extrusion of rocks in the center of the transpression zone. The lineament and thermochronology data call into question the traditional view of kinematic partitioning in the Southern Andes, in which deformation is focused on the Liquiñe-Ofqui Fault Zone.

2.2 Introduction

Kinematic partitioning of deformation at obliquely convergent plate margins into margin-orthogonal shortening and margin-parallel strike-slip components in the upper plate is a well-accepted tectonic model for many subduction and collisional orogens (e.g. Fitch, 1972; Beck, 1983; Kimura, 1986; McCaffrey, 1992). In these models, margin-parallel slip is thought to be resolved either on distributed strike-slip faults or on a limited number of prominent wrench faults, often localized within magmatic arcs and leading to the horizontal detachment and margin-parallel displacement of one or more elongate crustal slivers in the forearc (Jarrard, 1986; Beck, 1991; Tikoff and Teyssier, 1994; Chemenda et al., 2000; Hoffmann-Rothe et al., 2006).

In the Central and Southern Andes, prominent margin-parallel fault zones have been attributed to kinematic partitioning (Dewey and Lamb, 1992; Scheuber and González, 1999; Reutter et al., 1996; Cembrano et al., 2000, 2002; Hoffmann-Rothe et al., 2006) caused by oblique subduction of the Farallon and Nazca plates below the South American plate at angles between 10° and 30° (Pardo-Casas and Molnar, 1987; Somoza, 1998; Chen et al., 2019). Among those fault zones, the 1200 km long Liquiñe-Ofqui Fault Zone (LOFZ) in the Southern Andes is commonly viewed as the prime example of a highly localized intra-arc fault zone accommodating margin-parallel slip between 39°S and 47°S (Fig. 2.1; Hervé, 1976; Cembrano et al., 1996). Located within the Southern Andean Volcanic Zone (SVZ), the LOFZ separates the Chiloé area, commonly regarded as a forearc sliver, from the rest of the Andean orogen to the east of this fault zone (Fig. 2.1; Hervé, 1976; Cembrano et al., 1996; Lavenu and Cembrano, 1999; Cembrano et al., 2000). Due to the apparent northward displacement of crust underlying this area with regard to rocks east of the LOFZ (Wang et al., 2008), a major component of dextral strike-slip is attributed to the LOFZ (Cembrano et al., 1996, 2000; Wang et al., 2008). This slip component agrees with the obliquity in plate convergence (Pardo-Casas and Molnar, 1987; Angermann et al., 1999; Wang et al., 2008), the GPS velocity field (Klotz et al., 2001; Moreno et al., 2011), earthquake focal mechanisms (Lange et al., 2008; Sielfeld et al., 2019a) and principal directions of paleostress inferred form fault-slip analysis (Cembrano et al., 1996; Lavenu and Cembrano, 1999; Potent, 2003; Rosenau et al., 2006). In the context of this tectonic framework, the LOFZ is commonly regarded as a sub-vertically dipping, narrow fault zone consisting of two NNE-trending

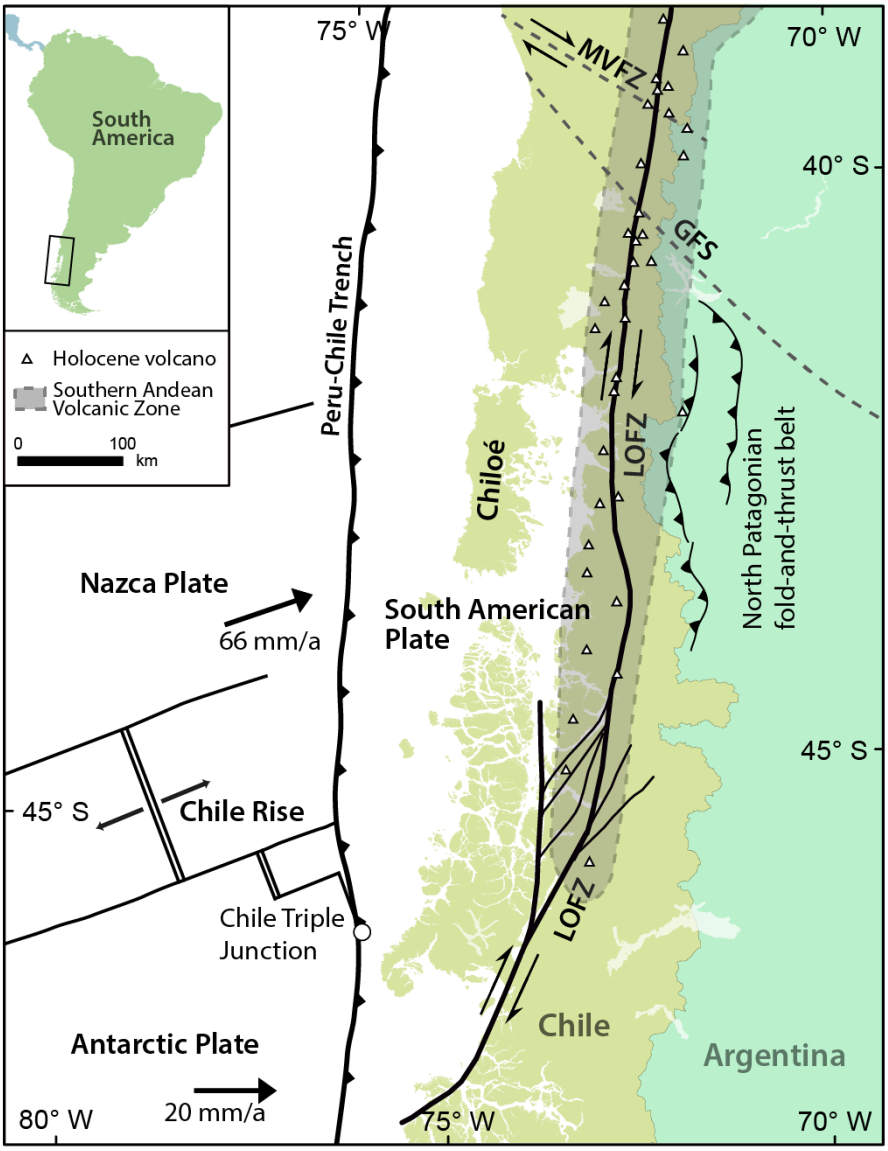

Figure 2.1: Tectonic setting of the Southern Andes between 40°S and 48°S. Black arrows indicate plate motions of the Nazca and Antarctic plates relative to the South America. LOFZ: Liquiñe- Ofqui Fault Zone, MVFZ: Mocha Villarica Fault Zone, GFS: Gaste Fault System.

lineaments that are connected through a number of step-over faults south of 43°S (Fig. 2.1; Lavenu and Cembrano, 1999; Cembrano et al., 2000, 2002; Catalán et al., 2017).

Traditionally, kinematic models of intra-arc deformation in the Southern Andes strongly focus on the strike-slip kinematics of the LOFZ as the main, or even the only, fault zone accommodating margin-parallel slip in this region (Cembrano et al., 1996, 2000; Lavenu and Cembrano, 1999). Recent paleomagnetic and kinematic studies, however, are at variance with the hypothesis of a single fault taking up

most of the margin-parallel slip component (Rosenau et al., 2006; Hernandez-Moreno et al., 2014; Stanton-Yonge et al., 2016). Testing models of kinematic partitioning in the Southern Andes, notably within the SVZ, is hampered by a lack of comprehensive structural data, especially from the southern portion of the LOFZ, as this area is most difficult to access. Here, we address intra-arc deformation in the southern portion of the SVZ by integrating new data on traces of prominent structural discontinuities (lineaments) inferred from remote sensing with exhumation rates compiled from published low-temperature thermochronology studies. We find that kinematic partitioning in the Southern Andes is more complex than accounted for by the traditional partitioning hypothesis and is in agreement with orogen-scale transpression. This tectonic scenario sheds new light on the role of the LOFZ in the SVZ.

2.2.1 Previous structural studies of the SVZ

2.2.1.1 The Liquiñe-Ofqui fault zone and forearc

Initially, the LOFZ was viewed as two co-linear, continental margin-parallel morphologic lineaments representing prominent faults, connected through NE-SW-striking step-over faults south of 43°S (Fig. 2.1; Hervé, 1976). Cembrano and Hervé (1993) interpreted the en-échelon geometry of the step-over faults as a crustal-scale duplex. Micro-fabric analysis of rocks from three transects across the main LOFZ-lineaments revealed (1) mylonites indicating sinistral oblique-reverse step-over faults at 39°S, (2) brittle faults formed by shortening and dextral strike-slip faults at 41°S - 42°S, and (3) a dextral mylonite zone at 42°S - 43°S (Cembrano et al., 2000). Similarly, Cembrano et al. (2002) provided microstructural evidence from the western master lineament and duplex shear zones for dextral displacement, but pointed out that displacement on these ductile deformation zones is also characterized by dip-slip, collectively amounting to dextral transpression south of 43°S. Furthermore, geochronological and fault-slip studies provide evidence for Neogene dextral displacement on the LOFZ (Hervé et al., 1993; Cembrano et al., 2000, 2002; Lagabrielle et al., 2004). Thermochronological studies, in particular, point to the presence of thrust faults that are kinematically associated with Miocene transpression at the southernmost LOFZ (Thomson, 2002; Georgieva et al., 2016). Finally, Lara et al. (2008) attributed significant shortening

and dextral strike-slip to transpression, based on geomorphologic and kinematic studies.

Paleomagnetic studies indicate mainly counter-clockwise vertical-axes rotations of up to 170° west of the LOFZ and predominantly clockwise rotation up to 150° to 170° east of the LOFZ (Beck, 1991; Cembrano et al., 1992; Rojas et al., 1994; Beck et al., 1998, 2000; Garcia et al., 2011; Hernandez-Moreno et al., 2014). Regional fault-kinematic studies by Potent (2003), Potent and Reuther (2001), Rosenau (2004) and Rosenau et al. (2006) revealed a number of first-order faults with variable kinematics, collectively pointing to complex intra-arc deformation in the northern SVZ. Following the tectonic concept of Riller and Oncken (2003) for the Central Andes, Rosenau et al. (2006) proposed a kinematic model explaining up to 120 km of margin-parallel displacement through segmentation of upper crust into rhomb-shaped domains defined by margin-parallel dextral and WNW-ESE-striking sinistral faults. Recent identification of morphological lineaments and paleomagnetic studies by Hernandez-Moreno et al. (2014) corroborate the large heterogeneity of deformation in the SVZ. These authors attribute differential counter-clockwise vertical-axis rotations of fault-bound domains to distributed deformation in the Chiloé area.

2.2.1.2 The Southern Andean retroarc

The retroarc zone of the Southern Andes comprises the eastern slopes of the Main Cordillera. Between 41°S and 44°S, deformation in this zone formed the North Patagonian fold-and-thrust belt (Fig. 2.1), characterized by N-S- and NW-striking faults (e.g. Diraison et al., 1998; Giacosa and Heredia, 2004; Orts et al., 2012; Echaurren et al., 2016). At 41°S, fault-slip analyses indicate reverse displacement on NW-striking faults and right-lateral displacement N-striking faults (Diraison et al., 1998). South of 44°S, the retroarc is segmented by Cretaceous to Cenozoic NW-striking sinistral strike-slip and reverse faults, and N-striking dextral strike-slip faults (Diraison et al., 2000; Lagabrielle et al., 2004). Based on microtectonic analyses, Lagabrielle et al. (2004) infer a Miocene phase of horizontal shortening accomplished on NW-striking thrust faults. In summary, the formation of the North Patagonian fold-and-thrust belt is attribute to two phases, one spanning from the late Cretaceous to early Paleocene and the other in the Miocene (Orts et al., 2012, 2015; Echaurren et al., 2016).

2.3 Methods

2.3.1 Lineament extraction

Morphological traces of planar structural discontinuities, i.e., lineaments, in the Southern Andes between 39°S and 46°S were extracted from high-resolution ASTER GDEM 2 digital elevation models (DEMs) with 30 m horizontal resolution, provided as 1 degree squares. Therefore, we developed a workflow tailored for data preparation and lineament extraction (Fig. 2.2). Individual DEMs were first merged to a single continuous DEM covering the entire study area. In order to precisely identify lineaments from the elevation models, three derivative datasets, each of which highlighting different attributes of the DEM, were calculated from the merged elevation model using the Spatial Analyst toolbox in ArcGIS (Esri). A hillshade model was calculated to enhance the contrast of elevation changes utilizing the tool Hillshade. Next, an aspect map, illuminating the directions facing individual slopes, was calculated using the tool Aspect and served to identify lineaments defined by uniform slope orientations. As erosion enhances the morphology of lithological and structural elements, a drainage map was included in the workflow. The drainage network was derived from the DEM using a combination of the tools Fill and Flow accumulation. Lineaments were then extracted from shaded relief models, drainage and aspect maps. Lineament extraction from high-resolution base maps as used in this study may easily result in oversampling of an enormous number of small-scale lineaments, which are difficult to interpret in terms of orogen-scale deformation. Lineament extraction was thus restricted to lineaments defined by major changes in the morphology within the Main Cordillera, such as steep valleys and prominent ridge lines with a length exceeding few tens of kilometers. In many cases, multiple datasets returned identical lineaments, which enhanced the confidence in the extraction procedure. As rivers and glaciers in the Southern Andes drain predominantly to the West and to the East, E-W trending escarpments are morphologically exaggerated. Therefore, we chose to exclude these escarpments from our lineament analysis.

2.3.2 Exhumation rates in the SVZ

In order to better understand the variation in extrusion of rocks and the possible presence of vertical displacements of structural discontinuities inferred from remote sensing in the Southern Andes, we compiled published fission track (FT) and (U-Th)/He apatite ages from Thomson et al. (2010), Georgieva et al. (2016) and Christeleit et al. (2017). Ages were converted to rock exhumation rates, which we regard as proxy to rock extrusion, applying the eroding half-space model by Willet and Brandon (2013). This model accounts for the cooling rate-dependence of closure temperatures, the advection of heat during exhumation of rocks and the

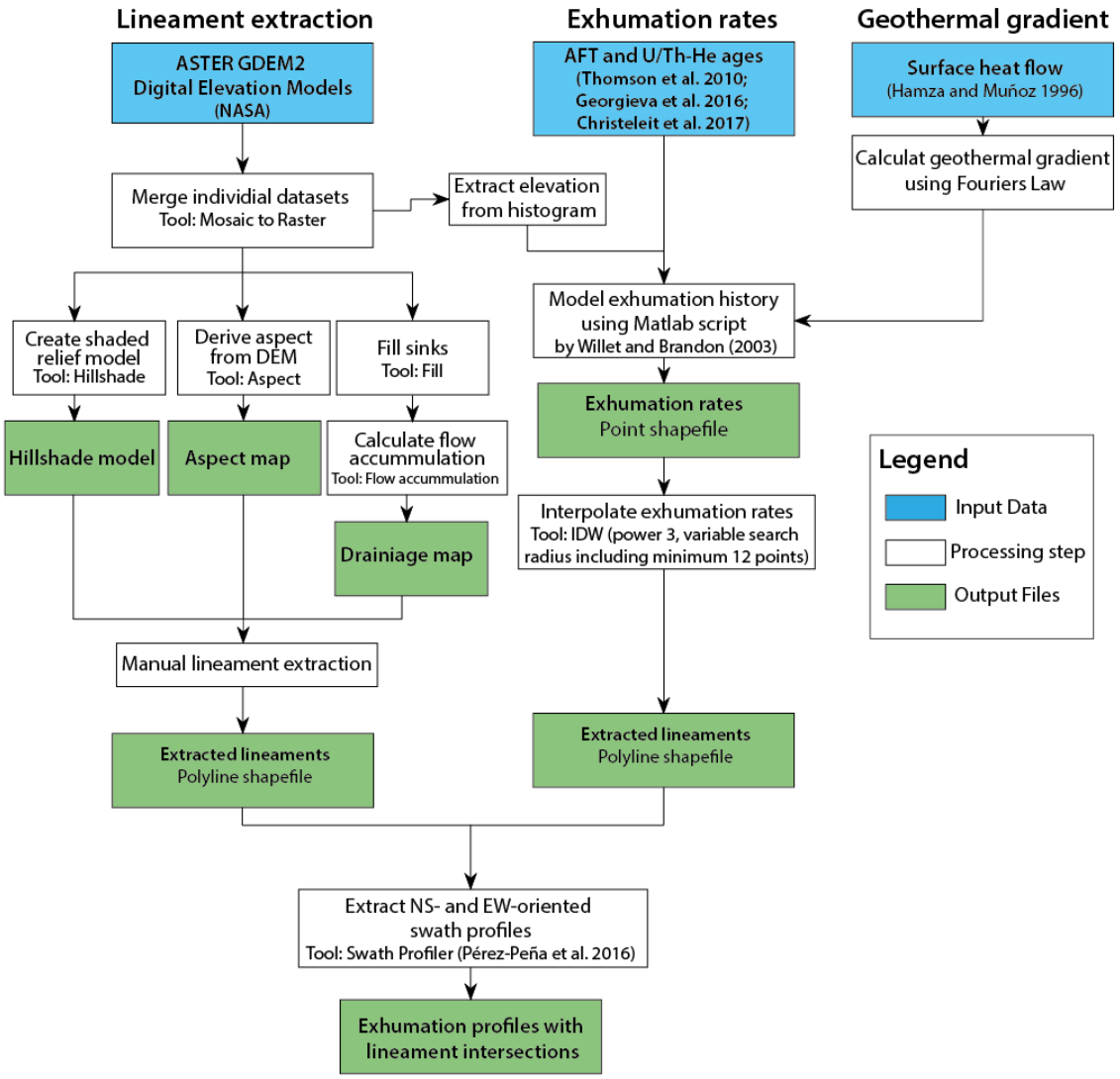

Figure 2.2: Diagram illustrating the applied workflow for lineament extraction and interpolation of exhumation rates from apatite fission track and (U-Th)/He ages. For explanation see text.

transient increase of the geothermal gradient with erosion. To convert thermochronology data to exhumation rates, knowledge of the surface temperature, geothermal gradient, mean elevation of the area of interest and the elevation, at which the sample was obtained, are required. Furthermore, the age of onset of erosion needs to be specified. In our case, the onset of erosion was set to 130 Ma, in order to include all measured AFT and (U-Th)/He ages and a mean surface temperature of 7°C (Fick and Hijmans, 2017) was used for our calculation of exhumation rates. Following Thomson (2002), the geothermal gradient is estimated at 23-45 °C/km, based on an average surface heat flow of 80-112 mW/m2 and the thermal conductivity of granite. The latter approximates well felsic intrusive rocks of the Patagonian Batholith. A mean geothermal gradient of 34° C/km was, therefore, applied to the model. In order to obtain representative mean elevation values, the study area was divided into six sectors (Fig. 2.3). Mean elevations were calculated for each from DEMs. In the cases, in which multiple apatite grains were used to obtain (U-Th)/He ages, the unweighted mean age was used for conversion to exhumation rates. Calculated exhumation rates were subsequently interpolated by means of inverse-distance weighting (Watson and Philip, 1985) using the respective errors in the underlying age as weighting factor. In order to highlight the variation in exhumation rates across prominent lineaments, swath profiles in E-W- and N-S-directions with a width of 10 km, each consisting of 50 individual, evenly spaced profile lines, were generated.

2.3.3 Model limitations

We note that the calculation of exhumation rates from a large dataset, as presented in this study, requires some assumptions regarding the constancy of exhumation and the geothermal gradient that may affect the magnitude of calculated exhumation rates. The eroding half space model applied in this study implies a constant erosion rate from the time of closure of the respective thermochronometric system. Based on age-elevation profiles, Thomson et al. (2010) and Christeleit et al. (2017) inferred a period of enhanced exhumation at 1 to 7 Ma and 5 to 10 Ma, respectively, for the Southern Andes. An age-elevation diagram including all available data does, however, not show any meaningful trend of measured ages with elevation for the entire study area (Appendix I, Supplementary Figure 1). Notably, Paleozoic and Mesozoic ages obtained at low

elevations do not permit the calculation of exhumation rates corrected for Pliocene-enhanced exhumation under a reasonable geothermal gradient, as proposed by Willet and Brandon (2013). Thus, our exhumation model does not include a Pliocene phase of enhanced exhumation. Consequently, exhumation rates calculated from ages older than 10 Ma may yield lower exhumation rates than comparable exhumation rates calculated with correction for local enhanced exhumation. As we assume uniform erosion rates since the closure of the AFT and the (U-Th)/He systems, calculated exhumation rates do not account for changes in exhumation related to changes in style of deformation, proposed for the Southern Andes (see previous section).

As demonstrated by Willet and Brandon (2013), the conversion of AFT and (U-Th)/He ages to exhumation rates is sensitive to the selected mean elevation and geothermal gradient. Sensitivity tests based on the selection of different geothermal gradients (Appendix I, Supplementary Figure 2) underscores a strong dependence of the output exhumation rate on the geothermal gradients. A spatial change of the geothermal gradient may, thus, have a strong influence on calculated exhumation rates. Sensitivity tests also show that all samples within the range of measured ages undergo the same change in exhumation rate with changing geothermal gradient (Appendix I, Supplementary Figure 2). Tests exploring the influence of errors in AFT and (U-Th)/He ages on the resulting exhumation rates show a linear correlation between increasing error and resulting changes in the exhumation rate (Appendix I, Supplementary Figures 3). An error of 10 % in the measured age roughly results in a 10 % variation of the calculated exhumation rate.

2.4 Results

2.4.1 Lineament characteristics

A total of 198 prominent lineaments, most of which trend WNW-ESE, N-S, and NE-SW and enclose rectangular to rhomb-shaped, upper-crustal domains, were identified between 40°S and 47°S (Figs. 2.3, 2.4). The N-S-trending lineaments, notably the two known master lineaments and their NE-SW trending connecting step-over lineaments of the LOFZ, collectively evident by major glacial valleys and

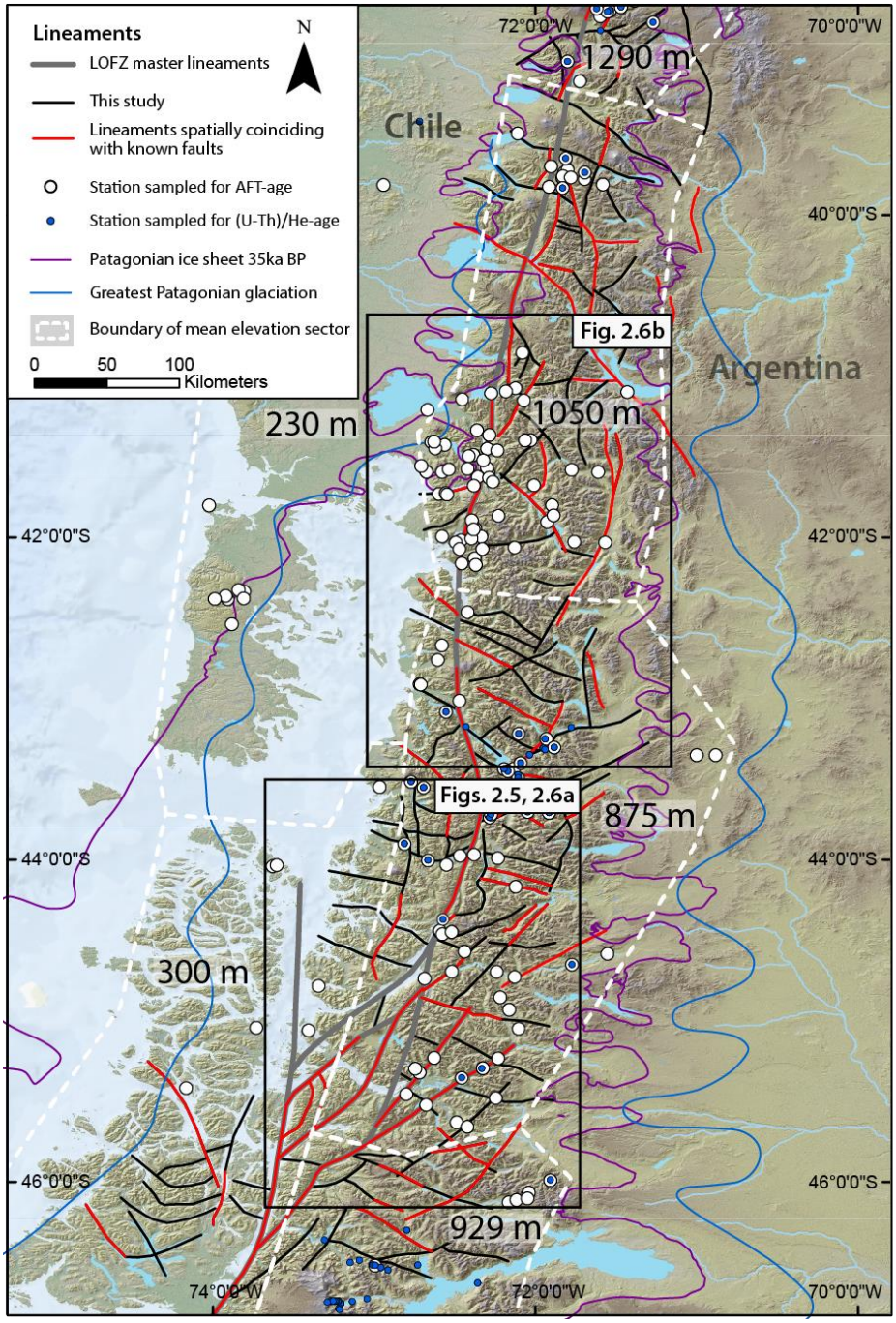

Figure 2.3: Map of the Southern Andean Volcanic Zone investigated showing lineaments identified in this study and stations of low-T thermochronology data compiled from Thomson et al. (2010), Geogieva et al. (2016) and Christeleit et al. (2017). Lineaments coinciding with mapped faults are compiled from Diraison et al. (1998); Sernageomin (2003); Lagabrielle et al. (2004); Orts et al. (2012) and Echaurren et al. (2016). Master lineaments of the LOFZ are from Thomson (2002). White dashed lines indicate sector boundaries used for mean elevation calculation. Respective mean elevation values are given for each sector. Greatest Patagonian glaciation and Patagonian ice sheet at 35 ka are from Hein et al. (2011) and Davies et al. (2020), respectively.

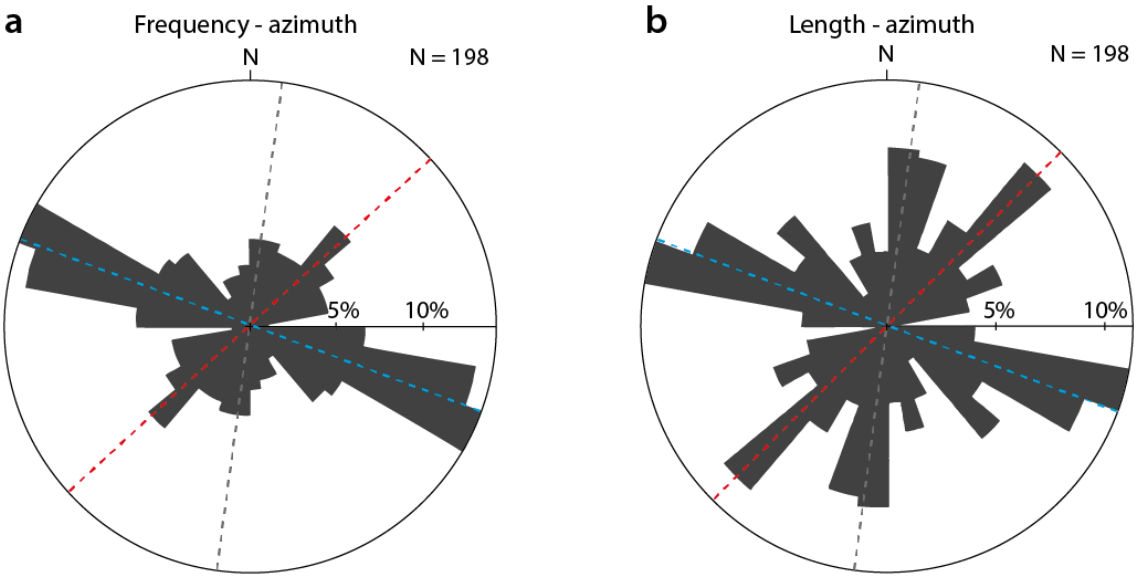

Figure 2.4: Rose diagrams displaying the azimuths of extracted lineaments in 10°-bins with respect to (a) the frequency of orientations and (b) the summed length of lineaments. Red, blue and grey dashed lines indicate NE-, NW- and NNE-trending clusters of lineament orientations.

fjords, are the longest and morphologically most prominent ones (Figs. 2.3, 2.5). Interestingly, all other lineaments terminate abruptly at the N-S-trending ones. WNW-ESE-trending lineaments are most abundant and transect the entire width of the orogen (Figs 2.3, 2.4).

In many places, WNW-ESE-trending lineaments are curved and truncated as well as displaced by N-S- and NE-SW-trending lineaments (Figs. 2.3, 2.5). These characteristics point to respectively distinct kinematics of upper-crustal deformation, even though some of the truncations may result from the difficulty in tracing lineaments. Truncated lineaments are particularly common in the southern part of the study area (Fig. 2.5). Strike-separations of displaced WNW-ESE-trending lineaments show both, right- and left-lateral apparent displacement components (Fig. 2.5), with sinistral displacements being less prominent than dextral ones.

2.4.2 Exhumation patterns

Compiled exhumation rates vary mostly between 0.1 and 2.0 mm/yr (Fig. 2.6). Even though the variation in these rates across the LOFZ are regarded as minor by

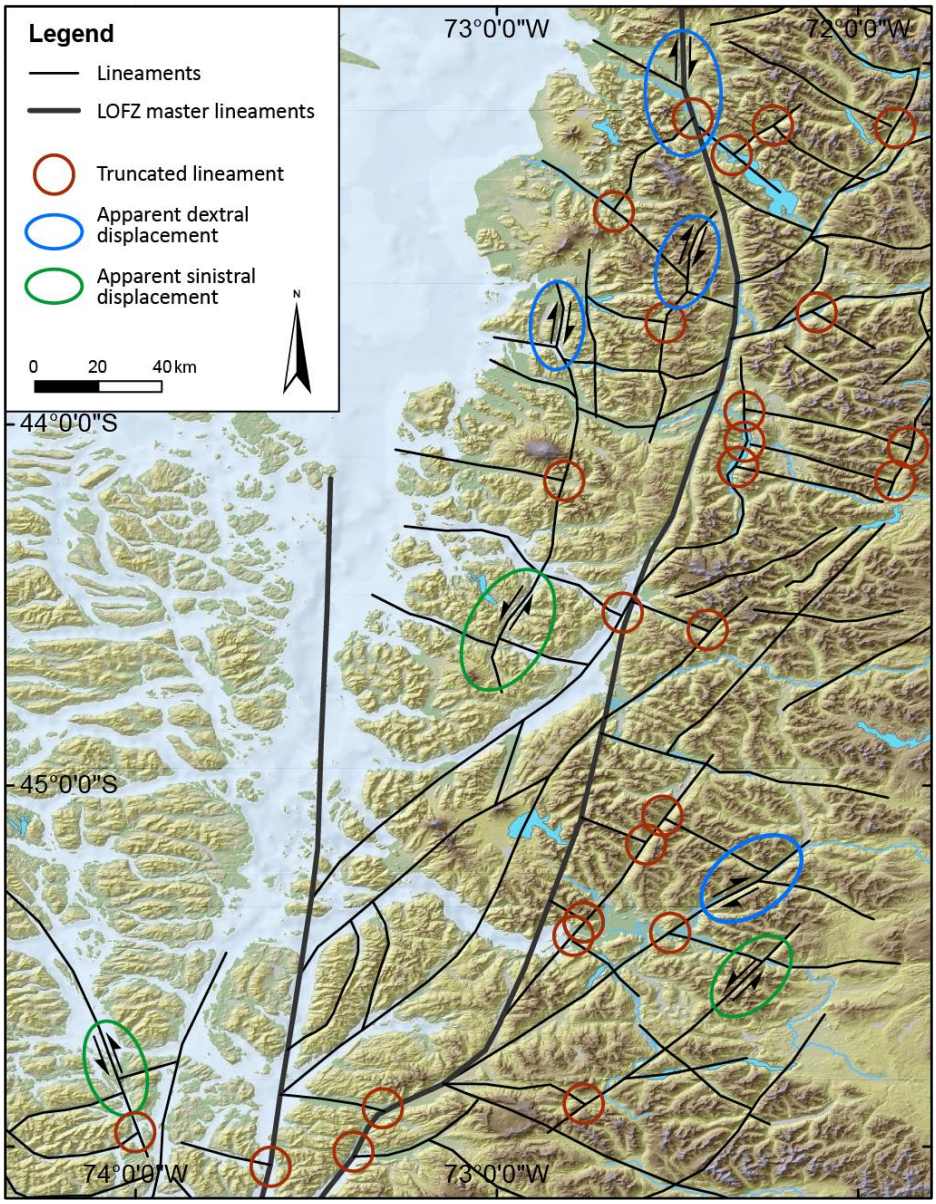

Figure 2.5: Lineaments, lineament abutments (red circles) and Horizontal slip components (half arrows) inferred from apparent displacements of lineaments, abutments of lineaments at mutual intersections (red circles) superimposed on topography from the southern portion of the Southern Andean Volcanic Zone. For location of area see Figure 2.3.

Thomson et al. (2010), their spatial distribution points to differential exhumation in the Southern Andes. Exhumation rates of up to 4.91 mm/yr are concentrated in the central portions of the orogen (Fig. 2.6). To the East and West, exhumation rates decrease to as low as 0.01 mm/yr. To explore to what extent exhumation is influenced by large-scale (crustal) deformation, the locations of lineament traces are indicated in two E-W and two N-S swath profiles (Fig. 2.7). The profiles show

that gradients in exhumation rates seem to spatially coincide with the location of mapped lineaments, whereby areas that are bordered by lineaments are characterized by uniform exhumation rates (Figs. 2.6, 2.7). Notably, gradients in exhumation are more pronounced at N-S-trending (orgen-parallel) lineaments than across WNW-ESE-trending lineaments.

2.5 Discussion

Due to the remoteness and inaccessibility of large parts of the Southern Andes, which render comprehensive, regional structural analyses most challenging (Cembrano et al., 1996, 2000, 2002; Lara et al., 2008), we attempt to constrain the mode of kinematic partitioning in this area through remotely-sensed lineaments and published exhumation rates. We will discuss the pattern of mapped lineaments, the kinematics of fault zones, portrayed by the lineaments, and the relationship between compiled exhumation rates and inferred faults. Based on this data and published fault-kinematic and paleomagnetic studies, we propose a viable alternative to the traditional hypothesis of kinematic partitioning for the Southern Andes.

2.5.1 Lineament pattern

A straightforward result of the lineament extraction from high-resolution DEMs is the fact that prominent lineaments are diverse in trend and distributed over the entire width of the Southern Andes (Fig. 2.3). Although the individual segments of the LOFZ are part of this lineament pattern, the LOFZ may not be as structurally important as conveyed in previous studies. Rather, the network of NE-SW- and WNW-ESE-trending lineaments is a ubiquitous structural characteristic of the Southern Andes (Figs. 2.3, 2.4). A fundamental issue regarding the interpretation of these lineaments in terms of deformation is the extent to which they correspond indeed to structural discontinuities, i.e. faults. We, therefore, compared the positions of extracted lineaments to known fault traces at the same locations (Fig. 2.3). Obviously, the master and associated step-over lineaments of the southern LOFZ have been recognized as faults for a long time (Hervé, 1976; Cembrano and Hervé, 1993; Cembrano et al., 2000, 2002). Similarly, most prominent WNW-ESE-

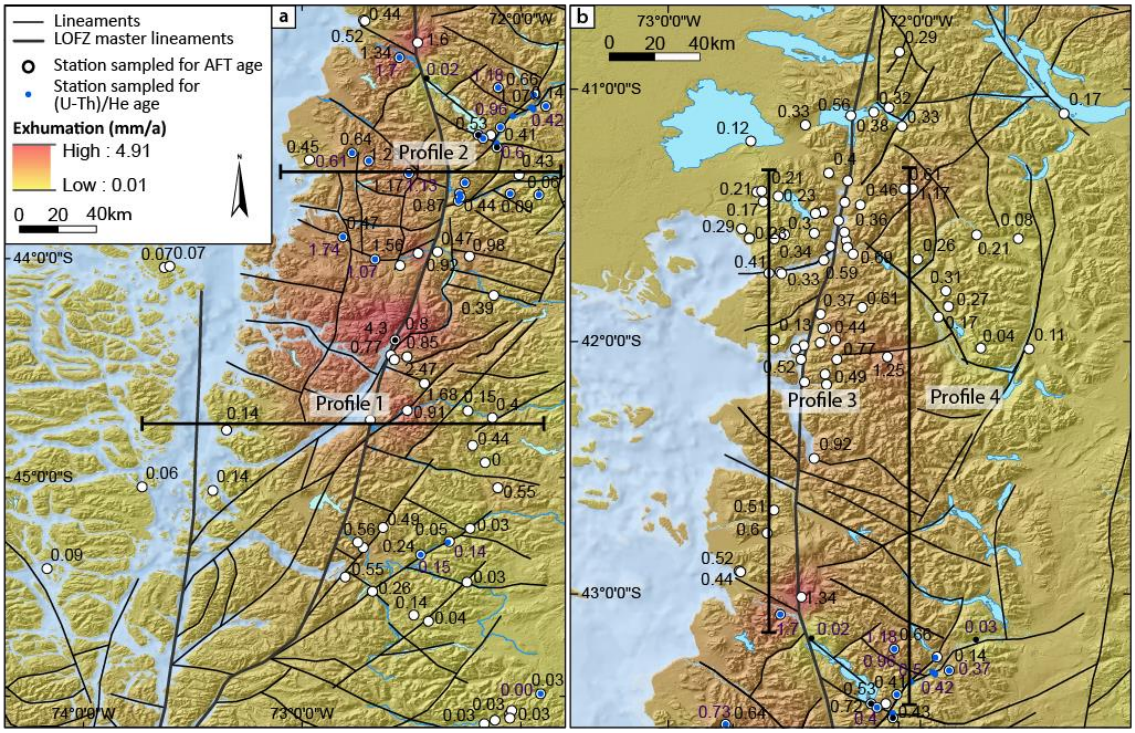

Figure 2.6: Interpolated exhumation rates superimposed on DEM from (a) the southern SVZ and (b) the central SVZ. Black lines indicate the locations of swath profiles in Figure 2.7.

trending lineaments, such as the Gastre and the Mocha Villarica Fault Zone (Fig. 2.1; Rapela and Pankhurst, 1992; Melnick and Echtler, 2006), known as Andean transverse faults (Pérez-Flores et al., 2016; Sielfeld et al., 2019b), have been diagnosed as pre-Andean structural discontinuities that were reactivated during Andean deformation (Yañez and Cembrano, 2004; Glodny et al., 2008; Melnick et al., 2009). More importantly, about half of the mapped lineaments do, in fact, correspond to faults (Fig. 2.3; Diraison et al., 1998; Sernageomin, 2003; Lagabrielle et al., 2004; Rosenau et al., 2006; Orts et al., 2012; Echaurren et al., 2016). As these lineaments share the same remote sensing characteristics as the rest of the lineaments, which lack direct fault evidence, we are confident that the latter do portray actual faults as well.

Based on the inversion of fault-slip data, Rosenau et al. (2006) proposed a kinematic hypothesis for the presence of margin-parallel dextral and WNW-ESE-striking sinistral faults for the northern portion of the SAVZ (see also Hernandez-Moreno et al., 2014). Numerical models corroborate this hypothesis and highlight the kinematic significance of WNW-ESE-striking structural discontinuities in this regard (Stanton-Yonge et al., 2016). Although less prominent in the northern SVZ,

NE-SW-trending lineaments, many of which are confirmed faults and connected to the LOFZ master faults, are present in the SVZ (Fig. 2.3). Their kinematic disposition with regard to the LOFZ master faults, reminiscent of synthetic Riedel shears, and shortening directions gleaned from fault-slip analysis (Potent and Reuther, 2001; Potent, 2003; Rosenau, 2004; Rosenau et al., 2006) point to significant dextral slip components on these faults. These faults and the pattern of mapped lineaments, adhering to faults, fit the kinematic partitioning hypothesis proposed by Rosenau et al. (2006). In summary, oblique plate convergence is not only taken up by dextral strike-slip on the LOFZ. Rather, upper-plate kinematic partitioning of deformation in the Southern Andes has affected the entire orogen and is, to a large extent, accomplished on WNW-striking structural discontinuities with sinistral slip components and NE-SW-striking discontinuities characterized by dextral slip components.

2.5.2 Lineament abutments

Displaced and truncated lineaments in the SVZ (Figs. 2.3, 2.5) offer important insight into the kinematics and the evolution of prominent structural discontinuities. Focussing specifically on lineament abutments between 42°S and 44°S, we note that E-W- to WNW-ESE-trending lineaments are systematically truncated or displaced by northerly and northeasterly trending ones (Fig. 2.3). Based on the inspection of strike separations of the displaced lineaments, the majority of the slip components on N-S- and NE-SW-trending lineaments amounts to dextral displacements, in agreement with fault-slip data and models of kinematic partitioning (Cembrano et al., 1996; Rosenau et al., 2006). Notably, in agreement with kinematic data, dextral displacement of major NW-trending lineaments across the main trace of the LOFZ is observed on multiple occasions (Figs. 2.3, 2.5). However, in some places apparent opposite horizontal slip components on the same lineament are recognized, corroborating observations by Cembrano et al. (2000) specifically for the LOFZ. Such cases occur notably where two or more sub-parallel lineaments are apparently displaced in opposite directions on N- and NE-trending lineaments. This lineament configuration can be explained by vertical displacement of oppositely dipping faults abutting on thrust- or reverse faults (Fig. 2.8) and indicates that the mapped lineaments are indeed the

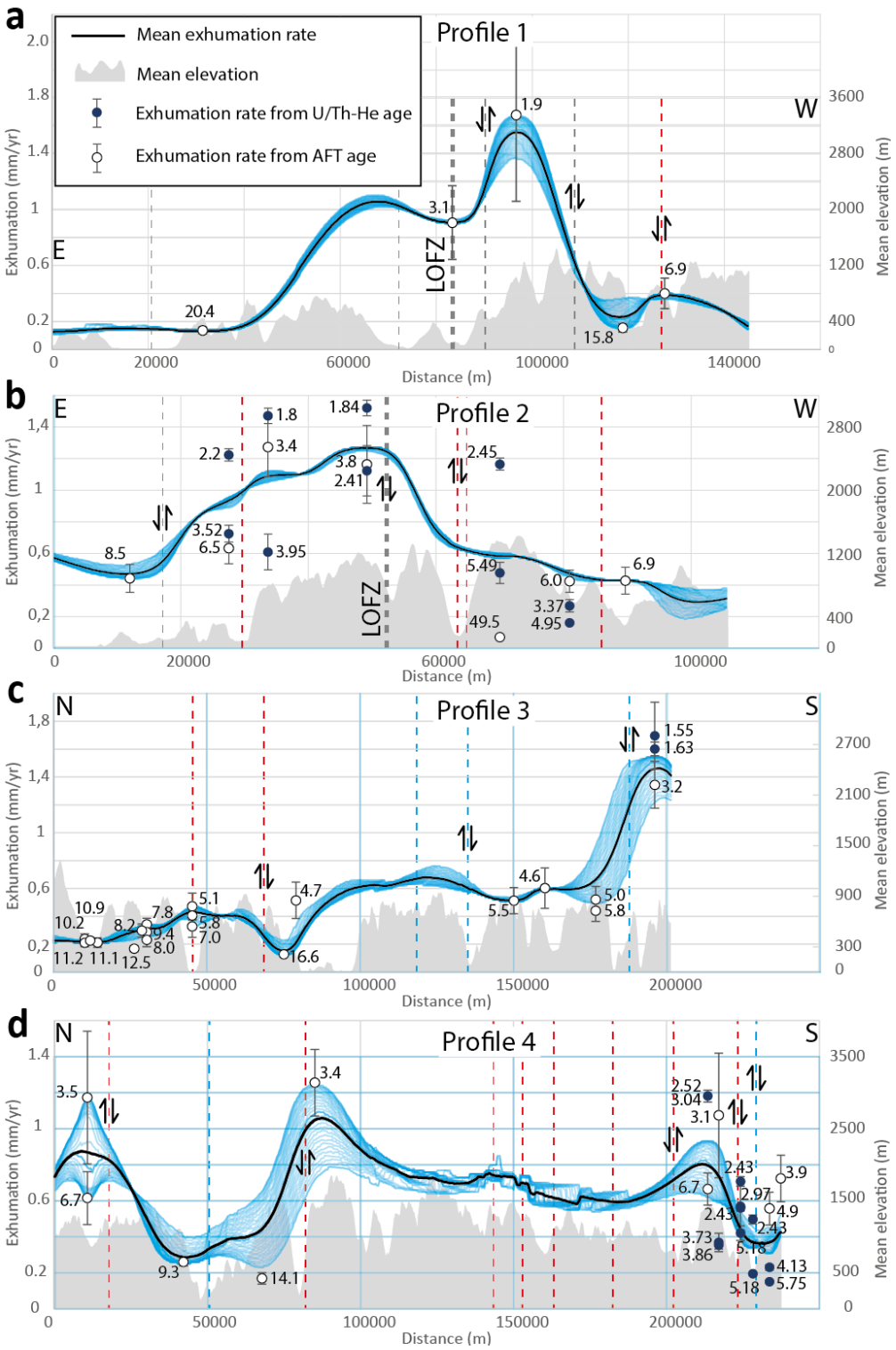

Figure 2.7: Swath profiles (width: 10 km) showing interpolated exhumation rates and mean elevation. (a) Profile 1, (b) Profile 2, (c) Profile 3, (d) Profile 4. For location of profiles see Figure 2.6. Numbers indicate the ages in Ma. Red, blue and grey dashed lines indicate NE-, NW- and N-S-trending lineaments, respectively.

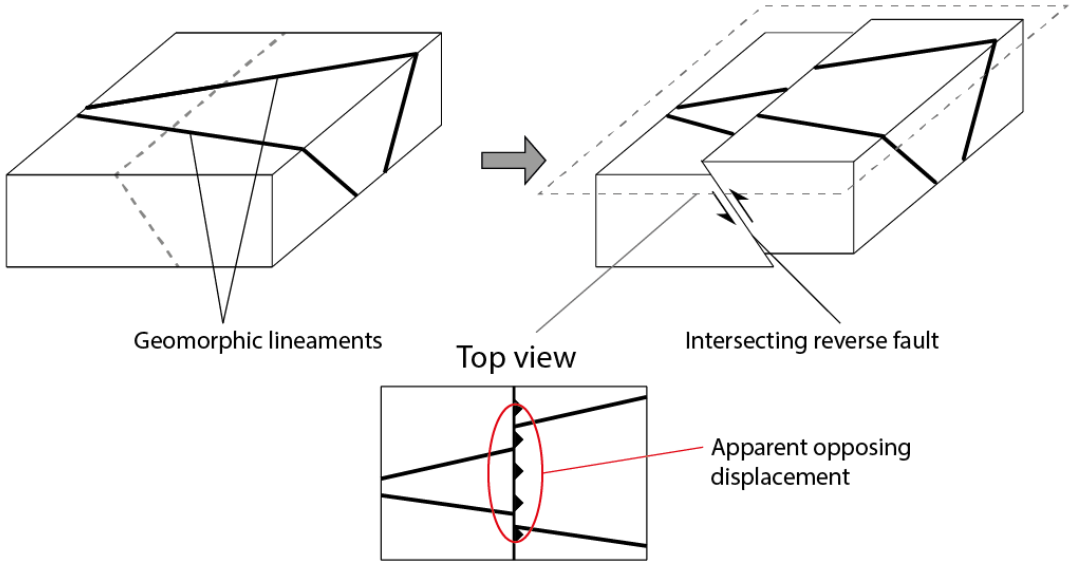

Figure 2.8: Schematic diagram illustrating sense of vertical slip components inferred from horizontal strike separations of (oppositely) dipping planar structures displaced on a reverse fault.

morphologic expressions of surface fault traces. Vertical displacements on faults associated with the LOFZ have been noted by Cembrano et al. (2002), Thomson (2002) and Lara et al. (2008). In fact, abutments of NW-trending lineaments in the southeast portion of the study area (Fig. 2.4) occur on NE-trending lineaments, which Thomson (2002) interpreted as reverse faults. Judging by the number of identified lineament abutments (Fig. 2.3, 2.5), vertical displacement on major NW- NE- and N-S-striking faults may have been underestimated previously in tectonic models of kinematic partitioning in the Southern Andes. Recognizing field studies such as the one by Cembrano et al. (2002), we conclude that the LOFZ is not characterized by dextral strike-slip only, and that any hypothesis on kinematic partitioning in the Southern Andes needs to honour significant vertical displacement components on margin-parallel structural discontinuities.

A second important aspect of documented lineament abutments concerns the evolution of the lineament (fault) sets. Based on our observations, WNW-ESE-striking lineaments are truncated by, and thus largely predate, N-trending lineaments, including step-over lineaments, of the LOFZ. This may indicate that orogen-scale, upper-crustal faulting in the Southern Andes has adhered to the classical model of brittle fault development in a fault zone, i.e., initial distributed faulting decreases progressively and culminates in the localisation of a single fault (Stanchits et al., 2011). By analogy, distributed faulting affecting the entire width of

the Andean orogen is followed by localization of deformation on a few master faults of the LOFZ in the orogen center. In fact, WNW-ESE- and NE-SW-striking faults were active in Neogene times (Rosenau et al., 2006; Lara et al., 2008) and, thus, started to be active before the LOFZ master faults at about 4 Ma (Cembrano et al., 2002) and many of the modern (Late Miocene to Recent) volcanic centers in the SVZ. We speculate that arc magmatism through thermal softening of crust may have rendered localization of deformation, i. e. the LOFZ, to the center of the SVZ (Fig. 2.1). Localization of deformation on the LOFZ may have been also prompted by a change in the tectonic style of deformation during the Neogene. Structural studies of the eastern sector of the Southern Andes indicate a Cretaceous and a Miocene phase of enhanced shortening, which lead to the formation of thrust and reverse faults in the retroarc (Orts et al., 2012, 2015; Echaurren et al., 2016). The observed present-day localization of deformation on the master faults of the LOFZ may well have been aided by a decrease in the shortening rate. Alternatively, enhanced glaciation during the Pliocene may have promoted an orogen-wide retreat of deformation to its' core which facilitates the LOFZ (Thomson et al., 2010). However, recent observations of intra-arc crustal seismicity in the Southern Andes demonstrate the activity of major margin-oblique faults aside from the main LOFZ indicating that distributed deformation to some degree has continued to this day (Sielfeld et al., 2019a).

2.5.3 Exhumation pattern

Interpolated rock exhumation rates highlight respective variations in the Southern Andes (Fig. 2.6). High exhumation rates of up to 4.91 mm/yr are evident in the central, topographically most elevated portions of the orogen. These rates are, on the one hand, attributed to denudation by enhanced glacial activity during the Pliocene and Pleistocene (Thomson et al., 2010; Christeleit et al., 2017). On the other hand, exhumation is maximal to the west of the highest elevations, likely due to orographic precipitation (Fig. 2.7a, b). Anomalously young AFT ages are reported from the vicinity of the LOFZ and were attributed to the influence of an enhanced upper-crustal heat flow caused by magmatism and associated advection of hot fluids along fracture zones (Thomson, 2002). Thus, high exhumation rates calculated from young AFT and (U-Th)/He ages close to the LOFZ and the present-day volcanic arc may have resulted from a higher geothermal gradient than used

for our calculation. As samples of various ages experience the same change in exhumation rate with changing geothermal gradient (Appendix I, Supplementary Figure 2), a change in the geothermal gradient results in an overall increase or decrease of all exhumation rates. Similarly, an enhanced erosion at 44° S due to enhanced precipitation, as proposed by Herman and Brandon (2015), would be expected to produce a widespread increase in recorded rock exhumation at the respective area. Consequently, considerable latitudinal and longitudinal variations in exhumation rates over few tens of kilometers (Fig. 2.7) may indicate that exhumation rates are overestimated, but processes such as local differential surface uplift and erosion also govern intra-arc variations in rock exhumation.

For example, the spatial correspondence of mapped lineaments with gradients in the interpolated surface of modelled exhumation rates indicates a considerable influence of large-scale (crustal) deformation on rock exhumation (Fig. 2.7). More specifically, differential rock uplift, i.e. vertical extrusion of rock, appears to be associated with reverse and thrust faults marked by the respective lineaments, notably N-S trending ones (Fig. 2.7a, b). Moreover, orogen-parallel exhumation curves display plateaus of high exhumation rates and narrow depressions of low exhumation rates, both bordered by lineaments (Fig. 2.7c, d). These observations agree with differential rock uplift of lineament-bound, upper-crustal domains. The pattern of compiled exhumation rates in combination with new lineament (fault) data provide evidence for widespread reverse faulting notably on N-S-striking faults, possibly enhanced through isostatic uplift due to glacial retreat in the Southern Andes. As the variations in exhumation rates across the Southern Andes are almost exclusively constrained by Miocene to Pliocene AFT and (U-Th)/He ages, reverse faulting occurred likely during the late Miocene and Pliocene. These observations agree with widespread Miocene reverse faulting along the LOFZ (Thomson, 2002; Cembrano et al., 2000, 2002) and the eastern slope of the Southern Andes (Diraison et al., 1998; Orts et al., 2015; Echaurren et al., 2016). Horizontal shortening as reported for the North Patagonian fold-and-thrust belt (Orts et al., 2012; Echaurren et al., 2016) may have affected the entire Southern Andes and, based on AFT and (U-Th)/He ages, may have continued into the Pliocene.

2.5.4 Revised mode of kinematic partitioning in the Southern Andes

Recent kinematic, geochronologic and paleomagnetic studies question the traditional concept of kinematic partitioning in the Southern Andes, in which the LOFZ is viewed as the dominant fault zone accomplishing horizontal shearing (Thomson 2002; Rosenau et al., 2006; Hernandez-Moreno et al., 2014; Georgieva et al., 2016). In accordance with previous structural studies (Diraison et al., 1998; Rosenau et al., 2006; Hernandez-Moreno et al., 2014), our structural evidence calls for Miocene distributed deformation on margin-parallel, NE-SW-striking and WNW-ESE-striking faults, which continued to be active to Pliocene times. Collectively, horizontal and vertical shear components on these faults affected the entire southern Andean orogen (Fig. 2.9). Rock uplift and differential vertical displacements on the LOFZ and other margin-parallel faults is maximal in the central portions of the orogen. The results indicate that the Southern Andes took up oblique plate convergence by horizontal shortening, crustal thickening and mostly dextral strike-slip, which fit the tectonic model of dextral transpression

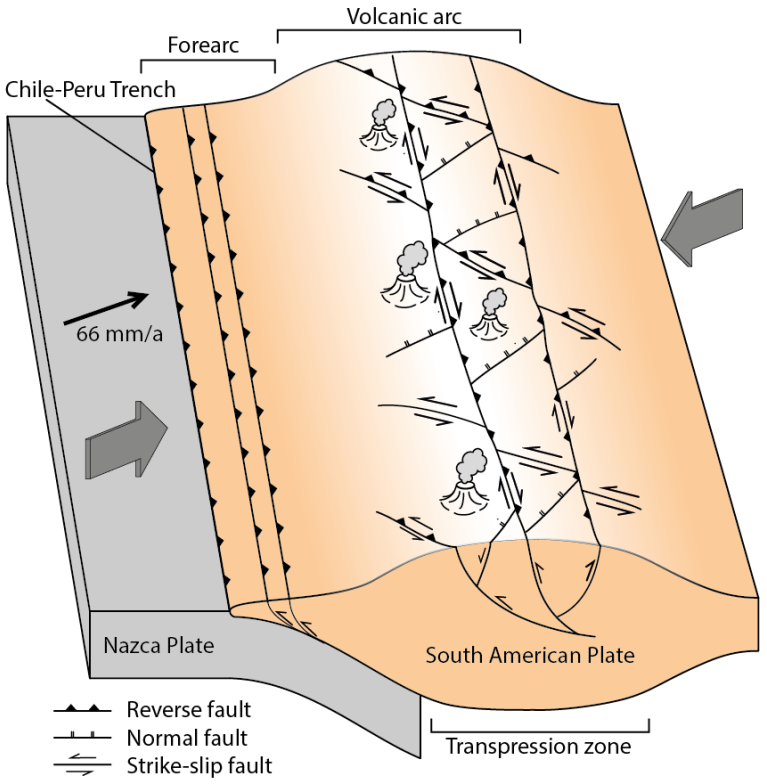

Figure 2.9: Schematic block diagram depicting kinematic partitioning amounting to dextral transpression in the Southern Andes.

(Harland, 1971; Sanderson and Marchini, 1984; Robin and Cruden, 1994; Dewey et al., 1998) on the orogen scale (Fig. 2.9). We regard the southern Andean orogen as a crustal-scale transpression zone with ill-defined zone boundaries. As stated above, the observed present-day concentration of slip on the LOFZ may have been the result of enhanced glacial erosion and decreased shortening since the Pliocene. In this context, transpression may well have been superseded by predominate dextral displacement on the LOFZ (Lange et al., 2008), oblique slip and reverse displacement however still occur today (Sielfeld et al., 2019a).

2.6 Conclusion

Identification of distinct lineament sets, portraying traces of upper-crustal faults or fault zones, and reassessment of low-T thermochronology data requires reconsideration of kinematic partitioning in the Southern Andes. We find that oblique plate convergence has been accommodated by (1) distributed deformation affecting the entire orogen, (2) three lineament (fault) sets accomplishing chiefly margin-parallel dextral displacement and horizontal shortening and (3) rock uplift that is maximal in the orogen center. These characteristics amount to dextral transpression on the orogen scale and indicate that previously the component of horizontal shortening was underestimated, whereas the kinematic role of the Liquiñe-Ofqui Fault Zone as the sole strike-slip fault was overestimated. AFT und (U-Th)/He ages indicate that the currently observe predominate strike-slip deformation within the Southern Andes may only may have begun during the late Pliocene.

3 Revisiting the sliver hypothesis of kinematic partitioning at the Southern Andean obliquely convergent plate margin

3.1 Abstract

Traditional models of kinematic partitioning at obliquely convergent plate boundaries entail margin-normal shortening, mostly in the fore-arc, and margin-parallel strike-slip in the orogen interiors. Due to the apparent detachment and horizontal displacement of elongate crustal blocks on strike-slip faults, this mode of kinematic partitioning became known as the sliver hypothesis, notably in the Southern Andes. Here, the Liquiñe-Ofqui fault zone (LOFZ) is regarded as a prime example of an intra-arc strike-slip fault zone, apparently displacing a fore-arc crustal sliver, known as the Chiloé Block. Based on novel lineament extraction and scaled analogue modelling, we question the sliver hypothesis for the Southern Andes. Analogue modelling experiments tailored to kinematic boundary conditions of the Southern Andes indicate the evolution of intra-arc deformation in two phases. Phase 1 is characterized by the formation of reverse faults oriented perpendicular to the plate convergence vector, followed by the formation of margin-parallel faults during phase 2. Model fault patterns portray compiled and remotely sensed first-order faults in the Southern Andes. Collectively, analogue modelling experiments and structural ground truth call into question the sliver hypothesis and point to distributed transpressive intra-arc deformation and clockwise rotation of crust accommodating oblique plate convergence in the Southern Andes.

3.2 Introduction

The concept of kinematic partitioning into margin-normal shortening and margin-parallel slip at obliquely convergent plate margins has been inferred mostly from earthquake focal mechanism and GPS velocity data (e. g. Fitch, 1972; Beck, 1991; McCaffrey, 1992; Nocquet et al., 2014). Margin-normal shortening is widely

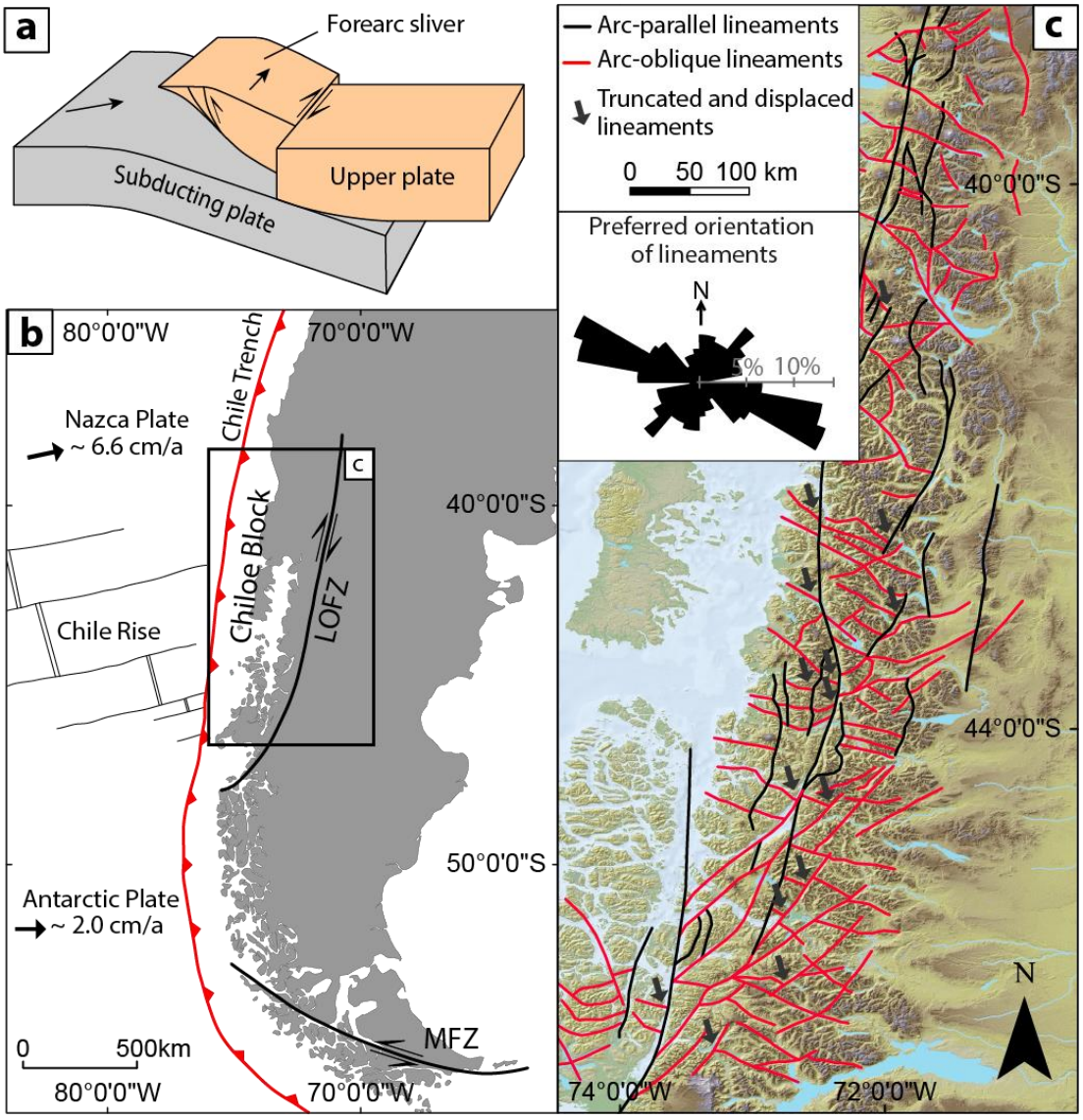

Figure 3.1: Plate tectonic setting and lineament data of the Southern Andes. (a) Schematic illustration showing the traditional view of kinematic partitioning at obliquely convergent plate boundaries (sliver hypothesis). (b) Tectonic setting of southern South America. LOFZ: Liquine-Ofqui fault zone, MFZ: Magallanes fault zone. (c) Morphotectonic lineaments of the study area.

believed to be resolved chiefly through thrusting in the fore-arc, whereas margin-parallel slip is accommodated on few major faults in the interior of orogens (Tikoff and Teyssier, 1994; Chemenda et al., 2000; McCaffrey et al., 2000). This interpretation of geophysical and structural data has led to the tectonic concept of fore-arc slivers displaced parallel to the plate margin (Fig. 3.1a; Wang et al., 2008). However, there is uncertainty about the dominance of margin-parallel faults in accomplishing margin-parallel translation of crust, which also pertains to the long-

standing controversy as to the presence of an impediment of translated crust at the leading sliver edges (Beck et al., 1993).

Similar to the morphologically most prominent Sumatran Fault System, Indonesia, the Liquiñe-Ofqui fault zone (LOFZ) in the Southern Andes (Fig. 3.1b), is regarded as a bonafide intra-arc fault zone accommodating large magnitudes of margin-parallel displacement of crust (Cembrano et al., 1996). As a consequence of oblique plate convergence, the forearc has been detached apparently from the LOFZ and displaced northward as a coherent crustal entity known as the Chiloe Block (Cembrano et al., 1996; Hoffmann-Rothe et al., 2006). However, the presence of prominent sets of first-order NE- to NNE- and WNW-striking faults, disposed at high angles to the LOFZ and transecting the entire Southern Andes in some areas (Cembrano et al., 2002; Rosenau et al., 2006) casts doubt on the sliver hypothesis in accommodating margin-parallel translation of crust. Here, we test this hypothesis of kinematic partitioning in the Southern Andes by comparing the pattern of first-order faults inferred from lineament extraction with model fault patterns of scaled analogue experiments tailored to kinematic boundary conditions of the southern Andean convergent plate margin.

3.3 Geological setting

Deformation in the Southern Andes has been largely controlled by oblique convergence of the Nazca and South American Plates since Eocene times (Somoza, 1998). As a consequence of this deformation, the LOFZ emerged between 38°S and 46°S at around 4 Ma (Cembrano et al., 2002) and displaced crust of the Chiloé Block toward the North (Fig. 3.1b; Forsythe and Nelson, 1985; Cembrano et al., 2000). Displacement of the Block in Recent times is consistent with GPS velocity (Moreno et al., 2011), earthquake focal mechanism (Lange et al., 2008) and fault-slip data (Cembrano et al., 2000; Rosenau et al., 2006). Structural filed studies from the Southern Andes (Fig. 3.1c) indicate the presence of prominent NNE-striking reverse and strike-slip faults, NE-striking normal faults and WNW-striking sinistral strike-slip faults, collectively amounting to dextral transpression (Rosenau et al., 2006; Lara et al., 2008; Stanton-Yonge et al., 2016; Sielfeld et al., 2019b).

3.4 Methods

3.4.1 Lineament extraction

Morphological lineaments of the Southern Andes between 40°S and 47°S were extracted from high-resolution ASTER GDEM 2 digital elevation models (DEMs) with 30 m horizontal resolution. Individual lineaments were identified from shaded relief models, aspect and drainage maps calculated from the original DEM using ArcGIS (Esri). As lineament extraction from such high-resolution datasets may easily result in oversampling of small-scale lineaments, which are difficult to interpret in terms of orogen-scale deformation, extraction focused on first-order morphological variations.

3.4.2 Analogue modelling

Transpression was simulated with a modelling apparatus consisting of a fixed half and a mobile half separated by a strike-slip velocity discontinuity (Fig. 3.2). Each half is equipped with a piston, which shortened the materials transverse to this discontinuity. In order to tailor the experiments to the kinematics of upper-crustal deformation in the Southern Andes at different convergence obliquities, which occurred during Tertiary times (Somoza, 1998), we used two distinct model setups, setup 1 and setup 2. Setup 1 modelled deformation caused by the present convergence obliquity of 70° between the Nazca and South American plates. Accordingly, the rates of strike-slip and shortening were scaled to the GPS velocities of the Southern Andes (Klotz et al., 2001; Moreno et al., 2011). Setup 2 simulated the Eocene to Oligocene convergence obliquity of 50° accomplished by respective adjustments of the strike-slip and shortening rates (Fig 3.2).

Both experimental setups utilized two model layers simulating brittle upper and viscous lower crust (Fig. 3.2). The lower crust is represented by a 2.1 cm thick layer of polydimethylsiloxane (PDMS)-corundum mixture (Zwaan et al., 2018), and the upper crust by a 0.7 cm thick layer of G23T quartz sand with a Mohr-Coulomb rheology (Schellart, 2000; Panien et al., 2006). A thin layer of nearly frictionless micro glass beads covered by plastic wrap lines the base of the box (Fig 3.2). This layer reduces friction between the base plate of the apparatus and the viscous layer and allows the viscous layer to deform freely. A plane inclined at 30° and mounted

to the piston of the moving apparatus half simulated the top surface of the subducting slab (Fig. 3.2).

The thickness of model layers was scaled to the likely depth of brittle-ductile coupling at 10 km between upper and lower crust, expressed as the mechanical strength ratio (R-value; Schueller and Davy, 2008). A representative R-value of 2.148 for the Southern Andes was calculated for this purpose (details on scaling and analogue materials are provided in Appendix II, Supplementary methods). Experiments were monitored with a stereo-camera system at an imaging rate of one minute and processed using the digital image correlation software DaVis 10.1 (LaVision), which allowed us to precisely analyse the evolution of surface deformation from 3D particle movement. To ensure reproducibility, experiments of each experimental setup were run four times (Appendix III, Figs. S1, S2, S3, S4).

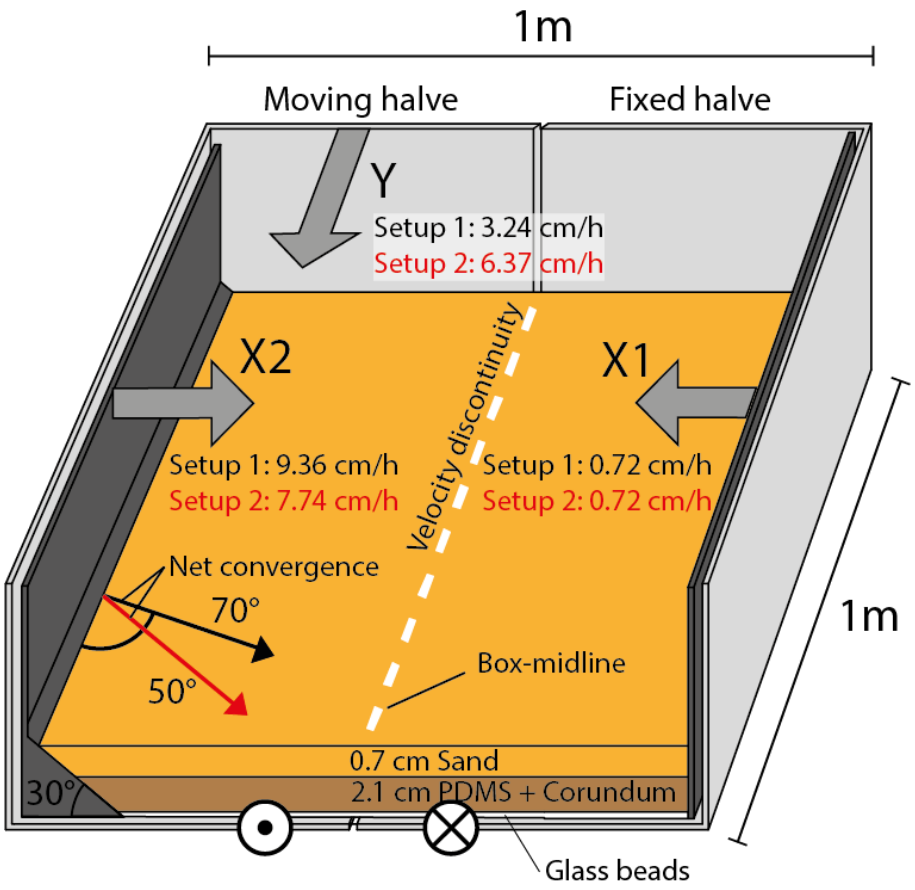

Figure 3.2: Schematic illustration of the experimental setup and applied boundary conditions. Grey arrows and labels indicate direction and applied velocities of the pistons X1 and X2 and the moving box halve Y.

As the modelling apparatus only permits to simulate sinistral shear, the recorded images and processed results are mirrored to match dextral transpression in the Southern Andes.

3.5 Results

3.5.1 Lineaments

Lineament extraction shows prominent sets of NNE-trending, i.e. continental margin-parallel, WNW- and NE-trending lineaments, with a directional preference of the WNW-trending set (Fig. 3.1c). Lineaments of this set are cut by, or truncate at, NNE- and NE-trending ones (Fig. 3.1c).

3.5.2 Analogue experiments

Faulting in granular material started 30 minutes after the onsets of experiments. Two faulting phases are apparent in both experimental setups. Phase 1, lasting ~70 minutes (~1.9 Ma in nature), is characterized by the formation of evenly spaced reverse faults striking oblique to the piston and crudely orthogonal to the convergence vector, (Fig. 3.3a, Appendix III, figures S1, S3). The faults form a central deformation zone.

Phase 2 in both setups is characterized by the formation of piston-parallel reverse faults close to the vertical piston (Fig. 3.3b, d). The location and number of these faults varies between both setups. In contrast to setup 2 experiments (Fig. 3.3d), a large number of piston-parallel reverse faults developed in setup 1 experiments, next to, and on either side of, the central deformation zone of piston-oblique faults (Fig. 3.3b). In both setups, the piston-oblique faults remained active during phase 2. Some piston-parallel reverse faults also formed in between piston-oblique faults (Fig 3.3b). The resulting rhomb-shaped pattern of piston-oblique and piston-parallel faults remained unchanged until the termination of the experiments at 90 minutes (2.8 Ma in nature). In both setups, the central deformation zone is characterized by net clockwise rotation of material, but piston-oblique faults are characterized by domains of counter-clockwise rotation, indicating sinistral reverse motion on the faults (Fig. 3.3c). Although piston-oblique faults remain active during

phase 2, a significant portion of shortening is accommodated on piston-parallel reverse faults forming pop-ups bound by oppositely dipping reverse faults (Fig. 3.4a).

3.6 Discussion

Lineament extraction in the Southern Andes shows that much of the orogen is transected by morphological lineaments (Fig 3.1c), many of which coincide with the traces of known first-order faults. Specifically, WNW-trending lineaments between 43°S and 39°S correspond to major sinistral and reverse faults, whereas dextral and reverse faults coincide with N-S- and NE-trending lineaments between 39°S and 46°S (Diraison et al., 1998; Cembrano et al., 2000; Thomson, 2002; Lagabrielle et al., 2004; Rosenau et al., 2006; Sielfeld et al., 2019b). Collectively, the spatial coincidence of morphological lineaments with major upper-crustal faults in the Southern Andes provides evidence that the extracted lineaments demarcate indeed the traces of major faults.

Piston-parallel reverse faults at the inclined piston correspond to thrust faults in the fore-arc (Fig. 3.3a). Moreover, an initially 5 cm to 10 cm wide gap in deformation between reverse faults at the inclined piston and faults of the central deformation zone (Fig. 3.3a) matches rather well with the 70 km – 140 km wide zone in nature that is largely devoid of faults. Hence, the central deformation zone spatially relates to the magmatic arc, the pattern of its first-order faults, visible as lineaments, coincides to a large extent with the respective model fault pattern (Figs. 3.1c, 3.3b, c). Moreover, the kinematics of faults in the central deformation zone, i.e., piston-oblique sinistral-reverse faults and piston-parallel thrusts (Fig. 3.3), agree remarkably well respectively with the kinematics of first-order WNW-striking and margin-parallel faults in the magmatic arc (Fig. 3.1c).

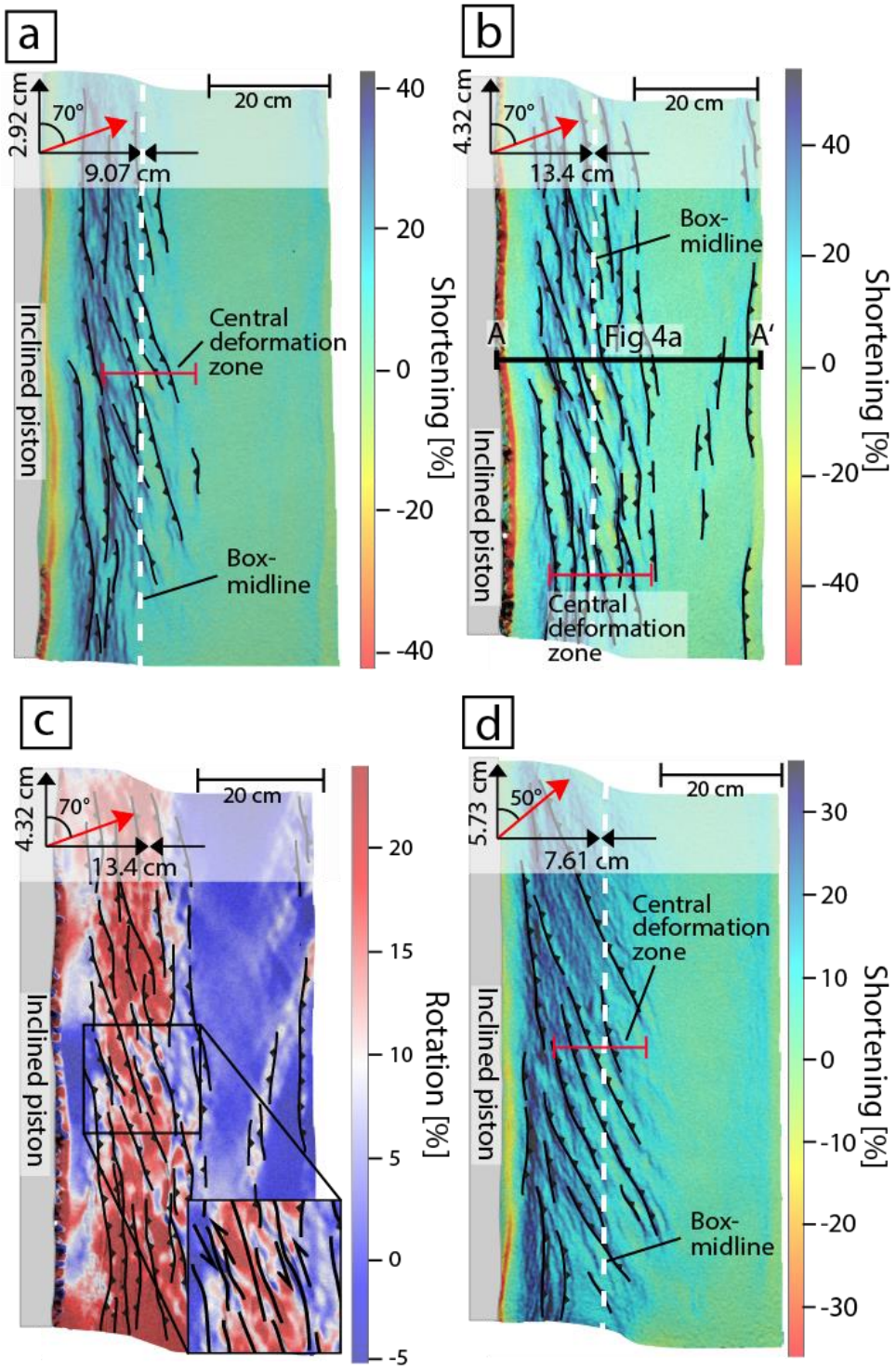

Figure 3.3: Images showing kinematic results of setup 1 and setup 2 experiments calculated from digital image correlation. (a) Cumulative shortening in setup 1 after 54 minutes. (b) Cumulative shortening in setup 1 after 80 minutes. (c) Cumulative vertical-axis rotation in setup 1 after 80 minutes. (d) Cumulative shortening in setup 2 after 54 minutes.

However, equivalent model faults to NE-striking faults do not seem to have developed in the experiments. This observation may indicate that the experiments were either terminated before such faults could have formed or that asymmetric fabric development imparted by dextral strike slip inhibited the formation of faults with this orientation. Similarly, N-striking faults, equivalents to the LOFZ, are far less developed in the experiments than margin-oblique faults and only formed in the central deformation zone in phase 2 of the experiments. Truncation of WNW-striking faults by N- and NE-striking faults (Fig. 3.1c) and geochronologic evidence for a Miocene to Pliocene, i.e., late-orogenic, formation of the LOFZ (Cembrano et al., 2000) are consistent with the experimental results and point to a two-phase structural evolution of the magmatic arc. Thus, overall shortening of the magmatic arc commenced at an early stage of the orogenic history and is evident by the pervasive presence of, and significant components of thrusting on, WNW-striking faults. As the orientation of the equivalent model faults depends chiefly on the convergence obliquity (compare Figs. 3.3a and 3.3d), the orientation of these faults points to their formation during a period of high convergence obliquity, and thus likely during Eocene-Oligocene times (Somoza, 1998).

An important outcome of the experiments is pervasive clockwise rotation of material in the central deformation zone, forming a wide, but well-defined, dextral transpressive shear belt (Fig. 3.3c). Clockwise rotation in this shear belt will affect any material surfaces striking parallel to the dominant set of piston-oblique thrust faults. Clockwise rotation of these faults in book-shelf manner accounts well for the sinistral displacement components on these faults (inset in Fig. 3.3c), which holds also for their WNW-striking equivalents in nature (Rosenau et al., 2006). Furthermore, predominant clockwise rotation of upper crust in the magmatic arc of the Southern Andes in Tertiary times is fairly well established by paleomagnetic studies (Cembrano et al., 1992; Beck et al., 2000; Hernandez-Moreno et al., 2014). Based on the structural and kinematic similarity of experiments and nature, we propose that the magmatic arc forms a distinct zone of dextral transpression, which commenced in Eocene-Oligocene times with the formation of en-echelon WNW-striking sinistral reverse faults. This scenario calls into question northward rigid-body translation of crust solely on the LOFZ and, thus, the sliver hypothesis

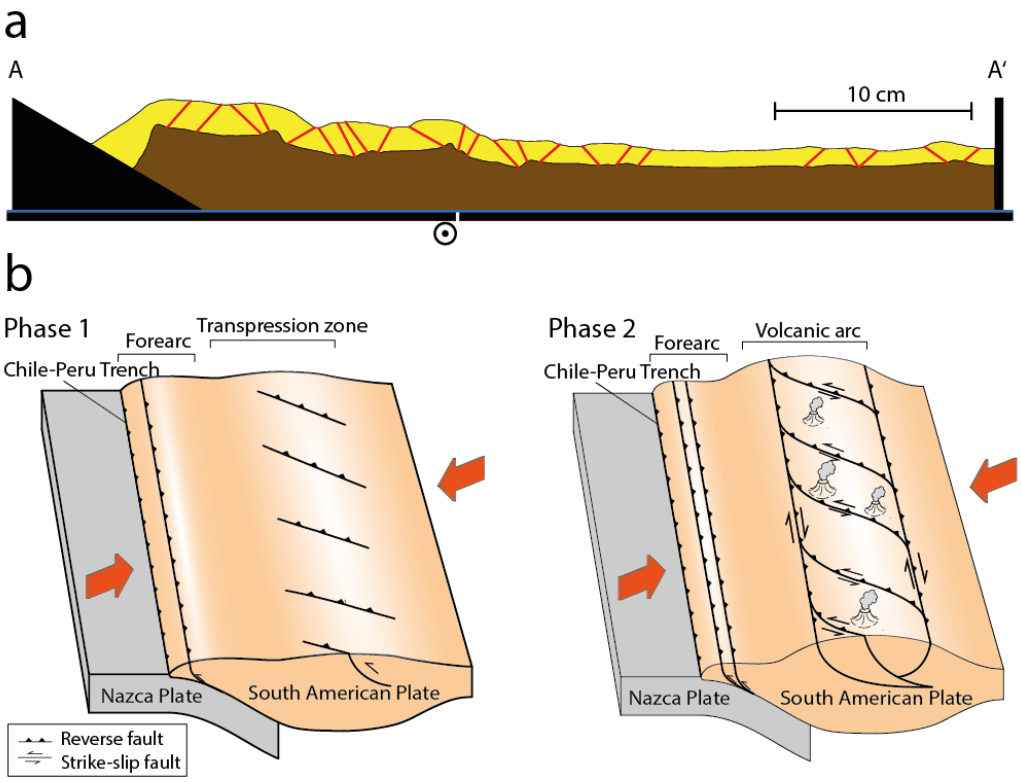

Figure 3.4: Early and final stages of fault development under oblique convergence. (a) Cross section A – A' (location in Fig. 3b) based on the final top surfaces of the sand and PDMS layers showing the final structural configuration of setup 1 experiments. Red lines denote reverse faults. (b) Schematic illustration highlighting the formation of faults in the Southern Andes based on experimental phases 1 and 2.

for the Southern Andes during most of the Tertiary. Northward displacement of crust by orogen-wide dextral transpression removes also a long-standing structural enigma associated with rigid-body translation, i.e., the apparent lack of an impediment at the northern margin of any displaced crustal block (Beck, 1993). Orogen-wide transpression resolves this issue through the pervasive presence of WNW-striking faults, serving as distributed buttressing zones in the Southern Andes.

3.7 Conclusion

Extracted first-order lineaments from, and scaled analogue experiments tailored to the kinematic boundary conditions of, the Southern Andes question the validity of the sliver-hypothesis for the Southern Andes during most of the Tertiary.

Experimental results show a two-stage structural evolution, notably of the magmatic arc, characterized by convergence-normal sinistral-reverse faults during phase 1 and piston-parallel thrusts with a dextral shear component during phase 2. The pattern, kinematics and overprinting relationships of extracted lineaments, corresponding to prominent fault zones, are consistent with the experimental results. In contrast to the rigid-body translation of crust along the LOFZ in the Southern Andes, which likely gained in importance only in the latest stages of the orogenic history, we propose that dextral transpression affected the magmatic arc and commenced in Eocene times. Kinematically, transpression was accommodated by overall clockwise rotation of crust, margin-parallel thrust faults and sinistral-reverse faults, which served as distributed buttressing zones.

4 Constraints on the Plio-Pleistocene stress field and regional volcanism from dikes surrounding the Copahue Caviahue volcanic complex, Andean Southern Volcanic Zone

4.1 Abstract

Previous studies of the Caviahue Copahue volcanic complex (CCVC), located in the Andean Southern Volcanic Zone, have recognized abundant associated dikes. Aside from their mere recognition, detailed studies of the dikes are however lacking. Here we present first comprehensive geochemical data and dike orientations which complement to our understanding of the Pliocene to recent regional stress field and the volcanic history of the CCVC. Major element concentrations show a basaltic to trachydacitic composition of dikes, akin to rocks of the CCVC. Coeval with proposed Miocene to Pliocene steepening of the subducting slab-dip, decreased Zr/Nb and Ba/Nb ratios of dikes and Copahue lavas compared to older products of the CCVC point to a decreasing degree of mantle melting resulting from reduced slab derived fluid flux. Orientations of dikes in the Caviahue depression indicate an emplacement as inclined sheets above a shallow crustal magma chamber which locally altered the regional stress field. Regional ENE- and ESE-trending maximum compressive stress axes (σ_{1H}), inferred from tightly clustering regional dike-trends are consistent with Pliocene-Pleistocene compression along the eastern slope of the Southern Andes. I accordance with published Miocene to Recent σ_{1H}-axes, regional dike trends indicate that proposed Miocene to Pliocene switch from upper-crustal shortening to extension occurred without changes in the orientation of σ_{1H}-axes and, thus, likely through a shift in the σ_3-axis-orientation from vertical to horizontal.

4.2 Introduction

Studying the spatial distribution and orientation of dikes has proven a useful tool to decipher the transport of magma in the context of the local and regional stress field (e. g. Delaney, 1986; Jolly and Sanderson, 1997; Gudmundsson, 2002; Galland

et al., 2007a, b; Tibaldi et al., 2010). Even under compression, where the axis of minimum compressive stress is expected to be vertical, dikes are emplaced parallel to the horizontal maximum compressive stress axes σ_{1H} (Tibaldi et al., 2010 and references therein). Thus, dike orientations serve as an excellent indicator for the orientation of principal stress axes under upper crustal compression and extension. Moreover, application of the Mohr circle to dike populations permits the calculation of relative magmatic driving pressures compared to regional upper-crustal stresses (Delaney, 1986; Jolly and Sanderson, 1997; Yamaji, 2016).

Extensive Neogene to Quaternary volcanism along the eastern Patagonian Andes provides ideal conditions for the investigation of volcanic activity in the foothills of a subduction orogen. In the Argentinian provinces of Neuquen and Mendoza, dikes and aligned volcanic vents associated with Tromen volcano (Galland et al., 2007a), the Payún Matrú volcanic field (Hernando et al., 2014), and the Malargüe fold-and-thrust belt (Barrinuevo et al., 2019) have provided insights in the influence of transpression on dike emplacement, and the associated stress field. Despite the large distance between individual volcanic centers, studies report a consistent bimodal orientation σ_{1H} axes trending ENE and ESE. Local strike-slip and reverse faulting is thereby observed in association with dike emplacement (Hernando et al., 2014; Barrinuevo et al., 2019). SW of Tromen and Payún Matrú, studies addressing the Pliocene to Pleistocene Copahue Caviahue vocanic complex (CCVC) recognized abundant associated dikes (Pesce, 1989; Linares et al., 1999; Melnick et al., 2006a). Despite their first recognition some 30 years ago, studies addressing the emplacement of the latter and their genetic relationship to the CCVC are however lacking.

The CCVC comprises the active Copahue stratovolcano and the Caviahue depression, also termed Caviahue caldera. Until today, the origin of the Caviahue depression remains controversial. Proposed scenarios for the formation of the depression include a pull apart basin in a strike-slip stepover (Folguera and Ramos, 2000) and a formation through collapse of an upper crustal magma chamber (Linares et al., 1999; Melnick et al., 2006a). Goal of this study is to investigate the emplacement of dikes associated with the CCVC in the context of the regional stress field and their genetic relationship to the volcanic complex on the basis of geochemical data and dike orientations.

4.3 Geological setting

The CCVC is located on the eastern slope of the northern Patagonian Andes within the Southern Volcanic Zone (SVZ; Fig. 4.1). To the West, the CCVC is bound by the southern Andean Main Cordillera, which is mainly composed of the Oligocene to Miocene sedimentary Cura Mallin formation (Radic et al., 2000, 2002) and Miocene volcanic rocks of the Trapa Trapa formation (Fig. 4.1b; Muñoz and Niemeyer, 1984; Melnick et al., 2006a). In the surrounding of the CCVC, these Oligocene to Miocene rocks are unconformably overlain by the Pliocene Cola de Zorro and Hualcupén formations (Vergara and Muñoz, 1983; Linares et al., 1999; Varekamp et al., 2006). Based on geological mapping, Melnick et al. (2006a) reported the Hualcupén formation as the local equivalent of the Cola de Zorro formation. Both units are therefore addressed as Cola de Zorro formation in this publication. The Cola de Zorro formation comprises basaltic to andesitic lava flows, debris flows and pyroclastic deposits (Mazzoni and Licitria, 2000; Melnick et al., 2006a, Varekamp et al., 2006). To the East, the CCVC is bound by the SSE-tending Loncopué trough, interpreted as a back-arc basin (Varekamp et al., 2010; Rojas Vera et al., 2014), and the Agrio fold and thrust belt composed of Mesozoic to Cenozoic sedimentary and volcanic rocks (Fig. 4.1b; Zamora Valcarce et al., 2010; Rojas Vera et al., 2015).

Pliocene to recent deformation in the northern Patagonian Andes is traditionally described as mostly transcurrent with the majority of intra-arc deformation concentrated on the N-S-trending Liquiñe-Ofqui fault zone (LOFZ; Cembrano et al., 1996, 2000; Rosenau et al., 2006). The LOFZ is interpreted to accommodate margin-parallel slip imparted through oblique subduction of the Nazca plate (Cembrano et al., 1996; Rosenau et al., 2006). Recent studies however provided evidence for transpressive deformation along the LOFZ and associated faults (Lavenu and Cembrano, 1999; Lara et al., 2008). The CCVC is located at the northern terminus of the LOFZ, which is characterized by NW- to NE-striking splay faults (Melnick et al., 2006b; Folguera et al., 2015). Among those, the NE-striking Lomin Fault terminates at the southeastern corner of the CCVC (Fig. 4.1b; Melnick et al., 2006b; Folguera et al., 2015).

4.3.1 Volcanic evolution of the CCVC

Volcanic activity of the CCVC began in the early Pliocene with the deposition of the Cola de Zorro formation, interpreted as the remnant of numerous polygenetic stratovolcanoes (Vergara and Muñoz, 1983; Varekamp et al., 2006). Large-scale Plinian eruptions allegedly formed this 400 m to 800 m thick volcanic succession. K-Ar ages for the Cola de Zorro formation range from 5.6 Ma to 4.0 Ma (Linares et al., 1999). The subsequent formation of the Caviahue depression during the Pliocene-Pleistocene marks the onset of deposition of the Copahue-Caviahue volcanic sequence (Fig. 4.2). The oldest reported volcanic rocks in the Caviahue

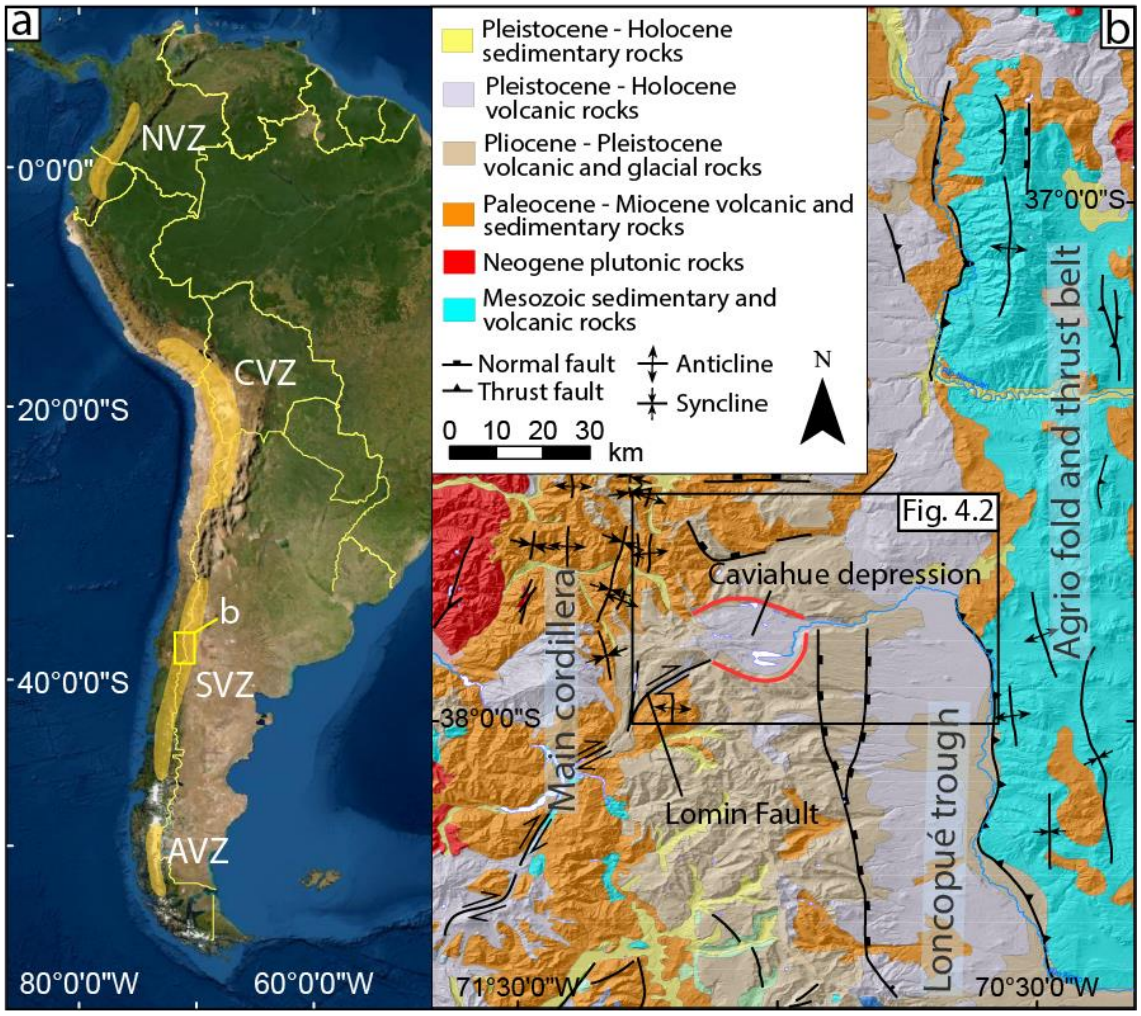

Figure 4.1: Volcanic Zones of the Andes and geology of the study area. (a) Volcanic zones of the Andes. NVZ: Northern Volcanic Zone, CVZ: Central Volcanic Zone, SVZ: Southern Volcanic Zone, AVZ: Austral Volcanic Zone. (b) Simplified geological map and main morphotectonic units of the Neuquén Andes. Red line marks the outline of the Caviahue depression.

depression belong to the Las Mellizas formation, which covers most of the depression (Fig. 2; Pesce, 1989; Linares et al., 1999; Melnick et al., 2006a). The Las Mellizas formation is composed of basaltic to andesitic lavas and ignimbrites (Melnick et al., 2006a). K-Ar and Ar-Ar ages for the Las Mellizas formation range from 2.68 Ma to 0.125 Ma (Linares et al., 1999; Sruoga and Consoli, 2011). Coeval with deposition of the Las Mellizas formation, a formation of the Caviahue depression as a collapse caldera was estimated at 2.68 Ma. Deltaic deposits underlying lavas of the Las Mellizas formation however indicate a formation of the latter unrelated to the formation of the depression and, thus, an older age of the depression (Hernando et al., 2020). The northeastern sector of the depression is covered by the andesitic Trolope lavas, which yield K-Ar ages of 1.63 to 1.09 Ma (Linares et al., 1999). The youngest rocks of the Copahue-Caviahue eruptive series belong to the active Copahue volcano, which displays an NE alignment of summit craters (Petrinovic et al., 2014a, b; Balbis et al., 2016; Baez et al., 2020). Copahue volcano is composed of basaltic to andesitic and subordinate dacitic lavas erupted in three stages (Melnick et al., 2006a; Baez et al., 2020). K-Ar ages point to an onset of volcano formation at around 1 Ma (Linares et al., 1999) while superposition of Copahue lavas over rocks of the Las Mellizas formation indicate an age of Copahue lavas younger than 0.125 Ma.

4.4 Methods

The orientation of dikes within the Caviahue depression and the trend of dikes in its' surrounding were acquired using a combination of field-based and remote sensing techniques. Orientations and across-strike thickness of dikes in the walls of the Caviahue depression were measured on 70 stations. Dike orientations obtained from digital outcrop models (DOMs) complimented field-based measurements. Representative samples of Dikes were taken for petrographic, major and trace element analysis.

4.4.1 Drone-assisted measurement of dike-orientations

3D DOMs were created using the photogrammetric "Structure from Motion-MultiView Stereo" (SfM-MVS) technique (Bilmes et al., 2019 and references

therein). Outcrop photos used for this purpose were acquired with a DJI Mavic 2 Pro drone equipped with a Hasselblad L1D-2c camera with 20-megapixel image resolution. Ground control points were measured with a pair of Emlid Reach Rs + RTK GNSS receivers. Processing of the DOMs was done using Pix4D mapper (Pix4D SA). Dike orientations and thicknesses were subsequently measured using the software Virtual Reality Geological Studio (VRGS).

4.4.2 Cluster analysis and stress inversion

Cluster analysis of dike orientations obtained in the Caviahue depression was performed by fitting a mixed Bingham distribution to the dataset using the software GArcmB (Yamaji and Sato, 2011; Yamaji, 2016; Umino et al., 2019). The software partitions orientation data into K pre-defined clusters where each cluster is represented by a Bingham component. Each Bingham component is defined by the concentration parameters κ1, κ2, and the relative mixing coefficient ϖ. Fitting of the mixed Bingham distribution is achieved through maximizing the respective log-likelihood function (Yamaji, 2016)

$$L(X) = \sum_{n=1}^{N} log_e P_{mB}(v_n|X),$$

where $P_{mB}(v_n|X)$ represents the probability density function of the mixed Bingham distribution (Yamaji and Sato, 2011). Optimal partitioning is determined by calculating Bayesian Information criterion

$$BIC = -2\mathrm{L}(X^{opt} + (6K - 1)\log_e N,$$

where L is the logarithmic likelihood function (Bishop, 2006), X^{opt} represent the optimal mixed Bingham distribution, and K is the number of Clusters. The optimal number of clusters is characterized by a minimal BIC. In order to determine the optimal partitioning for the set of measured dike orientations, GArcmB was run five times for 1 to 5 pre-defined clusters (K) repsectivey.

As dike intrusions occur when the magma pressure P_m exceeds the normal stress σ_n to the dike plane, fractures oriented perpendicular to the minimum stress axis open favourably at low P_m (Jolly and Sanderson, 1997). The distribution of dike pole-orientations therefore forms a cluster centered on the σ_3-axis. With decreasing

stress ratio $\phi = (\sigma_2 - \sigma_3)/(\sigma_1 - \sigma_3)$ or increasing magma pressure, P_m, the cluster of dike pole orientations, represented by the respective Bingham distribution varies from circular to elliptical to gridle-like (Jolly and Sanderson, 1997).

4.4.3 Remote sensing

Dikes in the surrounding of the Caviahue depression were identified from Satellite images using the World Imagery dataset provided by Esri. The trend of dikes was traced and converted to a polyline shapefile using ArcGIS (Esri). The azimuth between start- and endpoint and the length of each dike-trace were calculated from the dataset.

4.4.4 Major and trace elements

Major and trace element concentrations were measured on seven dike-samples which were selected to represent the entire macroscopic spectrum of compositions and textures. Additionally, four samples of lavas constituting Copahue volcano were measured (see table 4.1 for sample coordinates). Samples were prepared by crushing in an agate shatterbox. Aliquots were subsequently analysed by fused lithium tetraborate beads using standard XRF techniques at the Mineralogical-Petrographical Institute at the Universität Hamburg. Accuracy was controlled by measuring international standards.

4.5 Results

A total of 70 dikes were identified cutting the Cola de Zorro formation in the walls of the Caviahue depression (Fig. 4.2). Dike thicknesses range from approximately 0.5 m to 15 m. Cross-cutting of individual Dikes was observed in one location within the eastern wall of the depression (Fig. 4.3a). Dikes show a textural variation from porphyritic to aphyric with a black to dark grey aphanitic groundmass. Porphyritic dikes contain abundant plagioclase phenocrysts ranging from 0.1 cm to 1 cm in size and, with a lower abundance, clinopyroxene phenocrysts ranging from 0.1 cm to

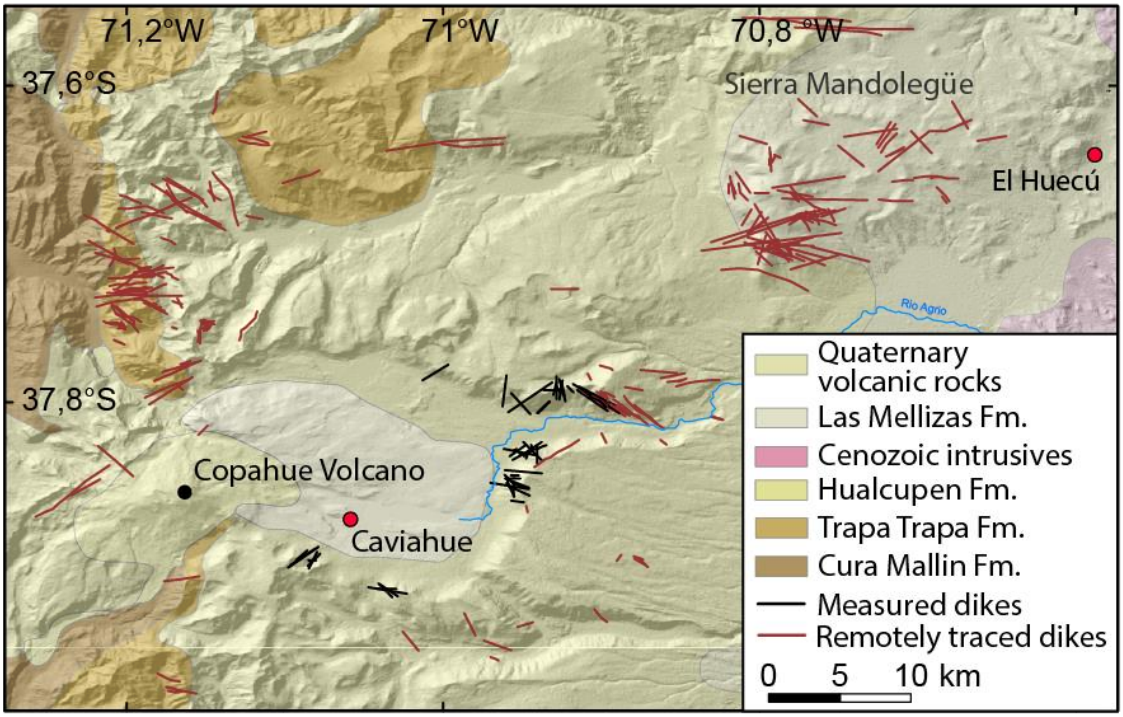

Figure 4.2: Dikes associated with the CCVC. (a) Measured and remotely traced dikes superimposed on generalized geological map after Sernageomin (2002) and Rojas Vera et al. (2014).

0.5 cm in size. The most primitive dike (sample 1033) only contains clinopyroxene phenocrysts. The groundmass of aphyric and porphyritic dikes is composed of plagioclase and subordinate clinopyroxene microcrystals and glass.

4.5.1 Dikes in the walls of the Caviahue depression

A lower hemisphere equal area projection of poles to measured dike surfaces shows distributed orientations of dike orientations with minor clusters of dikes trending in NE-SW, and NW-SE respectively (Fig. 4.3b). Cluster analysis with GArcmB indicates an optimal partitioning of the dike population into two clusters (Fig. 4.3c). The Bingham distribution comprising cluster 1 has a maximum concentration axis at (048/08), a gridled distribution with $\kappa 1 = -3.99$ and $\kappa 2 = -1.012$. Cluster 2 is defined by a maximum concentration axis at (137/00) and a circular distribution with $\kappa 1 = -41.197$ and $\kappa 2 = -25.044$. The mixing coefficient for both

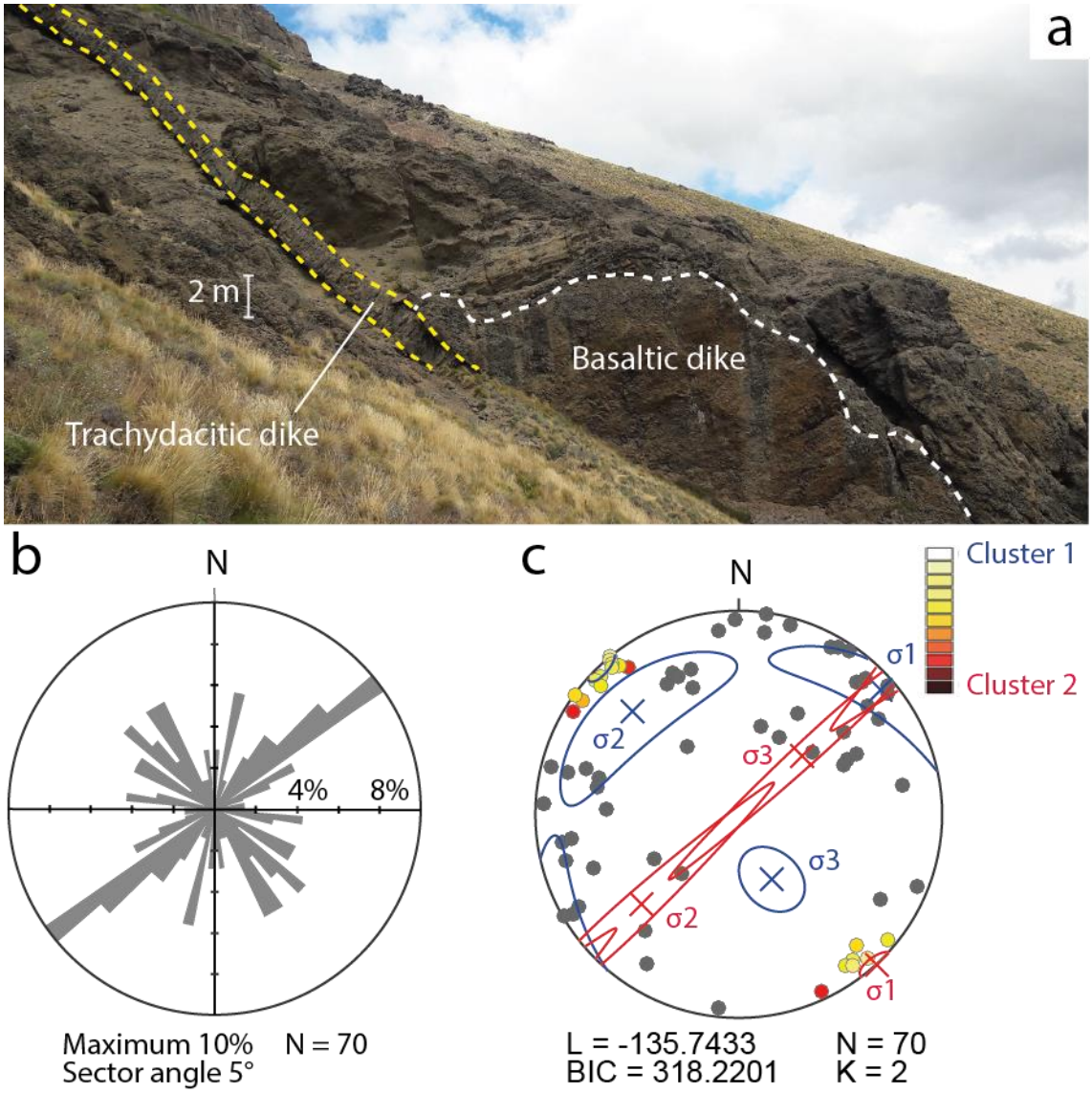

Figure 4.3: Dikes in the walls of the Caviahue depression. (a) Vertical basaltic dike (white dashed line) cut by moderately dipping trachydacitic dike (yellow dashed line). (b) Rose diagram showing strike orientations of measured dikes in the walls of the depression. (c) Poles to measured dikes displayed in a lower hemisphere equal area projection. Color-coded data points indicate the membership to cluster 1 and 2 determined with GArcmB. Maximum (σ_1), intermediate (σ_2) and minimal (σ_3) principal stress axes for both clusters are shown in blue for cluster 1 and red for cluster 2.

Bingham distributions is $\varpi 1 = 0.8215$ and $\varpi 2 = 0.1785$ for cluster 1 and cluster 2, respectively. The calculated stress ration ϕ for Cluster 1 yields 0.2529 and 0.608 for cluster 2.

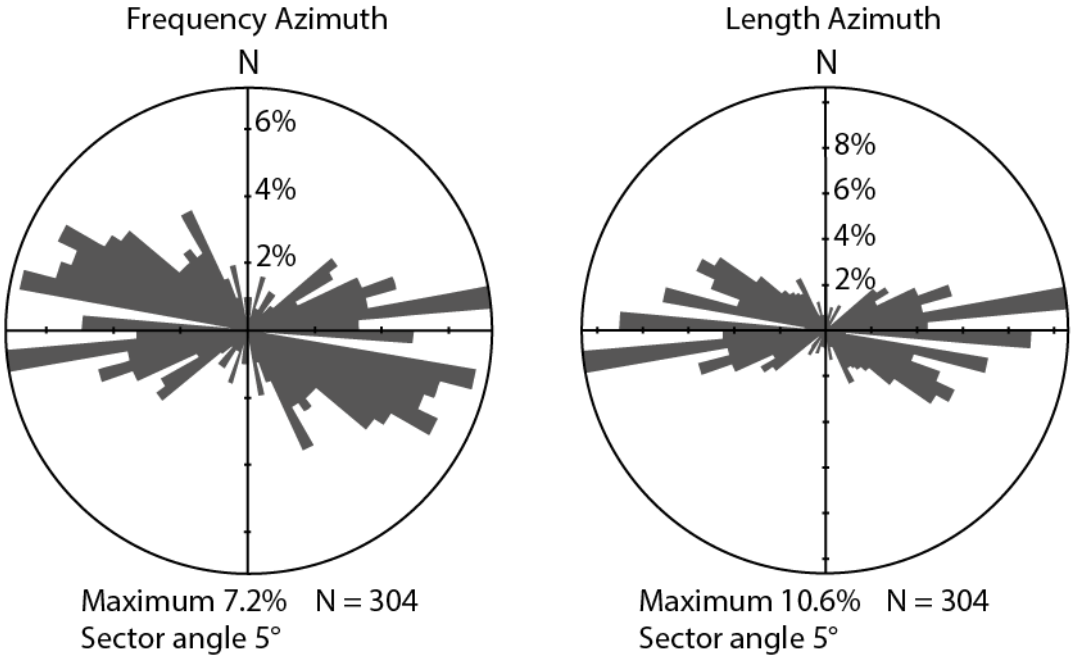

Figure 4.4: Frequency- and length-weighted rose diagrams showing the strike orientation of remotely traced dikes in the surrounding of the Caviahue depression.

4.5.2 Dikes surrounding the Caviahue depression

Dikes identified on satellite images in the surrounding of the Caviahue depression are concentrated in three distinct areas (Fig. 4.3): NW of the depression, dikes are identified cutting Miocene sedimentary and volcanic rocks of the Cura Mallin and Trapa Trapa formations (Fig. 4.2). In the North-East, dikes were identified in Pleistocene to Quaternary volcanic rocks. East of the depression, dikes cut the Pliocene Cola de Zorro Formation (Fig. 4.2). A frequency azimuth rose diagram of the surface traces of identified dikes shows predominate WNW and WSW strike orientations for dikes surrounding the Caviahue depression (Fig 4.4a). A length weighted rose diagram shows a stronger pronounced ENE-trend compared to the frequency azimuth diagram (Fig.4. 4b).

4.5.3 Major elements

Results of XRF-analysis of representative dike samples and Copahue lavas are presented in Table 4.1. According to the TAS classification of Le Bas et al. (1986) sampled dikes are basalts, basaltic andesites, basaltic trachyandesites,

Table 4.1: Major element composition of dikes in the walls of the Caviahue depression and Copahue lavas

Sample	Latitude	Longitude	LOI (%)	Sum (%)	SiO_2	Al_2O_3	Fe_2O_3	MgO	MnO	CaO	Na_2O	K_2O	TiO_2	P_2O_5	SO_3
Dikes															
792-7	-37,809937	-70,827542	0,21	99,48	58,85	17,86	6,71	2,64	0,14	5,73	4,42	1,71	0,79	0,25	0
802	-37,830698	-70,953082	3,63	99,439	56,99	15,51	8,05	1,44	0,17	4,54	4,09	2,93	1,4	0,48	0,02
895	-37,805188	-70,944712	3,31	99,082	54,2	16,75	8,41	2,17	0,14	7,07	3,21	2,16	1,14	0,32	0,02
907	-37,791678	-70,929281	2,35	99,147	57,66	16,08	7,42	1,47	0,14	4,81	4,72	2,35	1,42	0,57	0
933	-37,851656	-70,957918	1,88	99,199	63,54	16	4,23	1,13	0,1	2,8	4,72	3,72	0,73	0,18	0
934	-37,851766	-70,958244	1,26	99,053	56,04	16,76	8,5	2,5	0,17	6,07	4,24	1,77	1,24	0,36	0
1023	-37,917876	-71,035588	1,5	99,191	50,47	17,04	9,34	6,78	0,14	8,2	3,34	0,83	1,09	0,25	0,02
Copahue Lavas															
568	-37,88333	-71,096464	0,21	99,238	54,76	17,18	8,57	4,5	0,13	7,21	3,49	1,62	1,12	0,26	0,01
924	-37,857724	-71,115726	-0,02	99,256	56,99	17,06	7,69	3,66	0,12	6,29	3,76	2,14	1,09	0,29	0
979	-37,845211	-71,12666	-0,09	99,666	61,91	15,43	6,96	1,68	0,12	4,05	4,41	3,24	1,31	0,42	0,02
1021	-37,851023	-71,114047	0,02	99,423	55,7	17,1	8,48	3,79	0,13	6,55	3,81	2,05	1,21	0,34	0,06

Table 4.2: Trace element compositions of dikes in the walls of the Caviahue depression and Copahue lavas in ppm.

Sample	As	Ba	Ce	Co	Cr	Cu	Ga	La	Nb	Nd	Ni	Pb	Rb	Sc	Sr	Th	U	V	Y	Zn	Zr	Bi
Dikes																						
792-7	37	397	40	22	1	33	12	35	10	23	2	11	34	15	607	8	7	111	19	57	161	-1
802	11	502	66	22	-7	82	25	40	14	56	0	25	78	23	338	8	-2	138	44	88	328	-1
895	-3	347	38	28	35	77	21	16	11	46	19	13	80	20	460	7	2	164	32	80	208	6
907	11	481	43	13	-8	30	25	25	14	32	-1	14	39	19	431	3	1	83	44	100	243	-1
933	2	664	65	11	-1	20	24	25	16	40	0	21	92	11	249	11	4	53	38	55	355	-4
934	2	431	31	21	-7	47	21	27	9	3	5	10	40	29	406	7	4	156	34	82	180	-2
1023	-3	232	28	40	338	88	11	18	5	15	135	5	15	19	550	-3	-2	175	20	73	110	9
Copahue Lavas																						
568	-5	376	58	32	78	67	18	20	9	19	44	16	45	17	503	6	5	199	26	76	177	5
924	6	453	58	26	35	53	17	11	11	48	33	15	60	21	510	8	4	155	27	71	225	4
979	24	622	83	17	-8	26	23	52	15	37	3	22	94	15	337	9	2	117	39	84	330	5
1021	7	466	53	25	43	42	18	28	11	22	23	10	57	26	498	11	4	170	28	81	238	-3

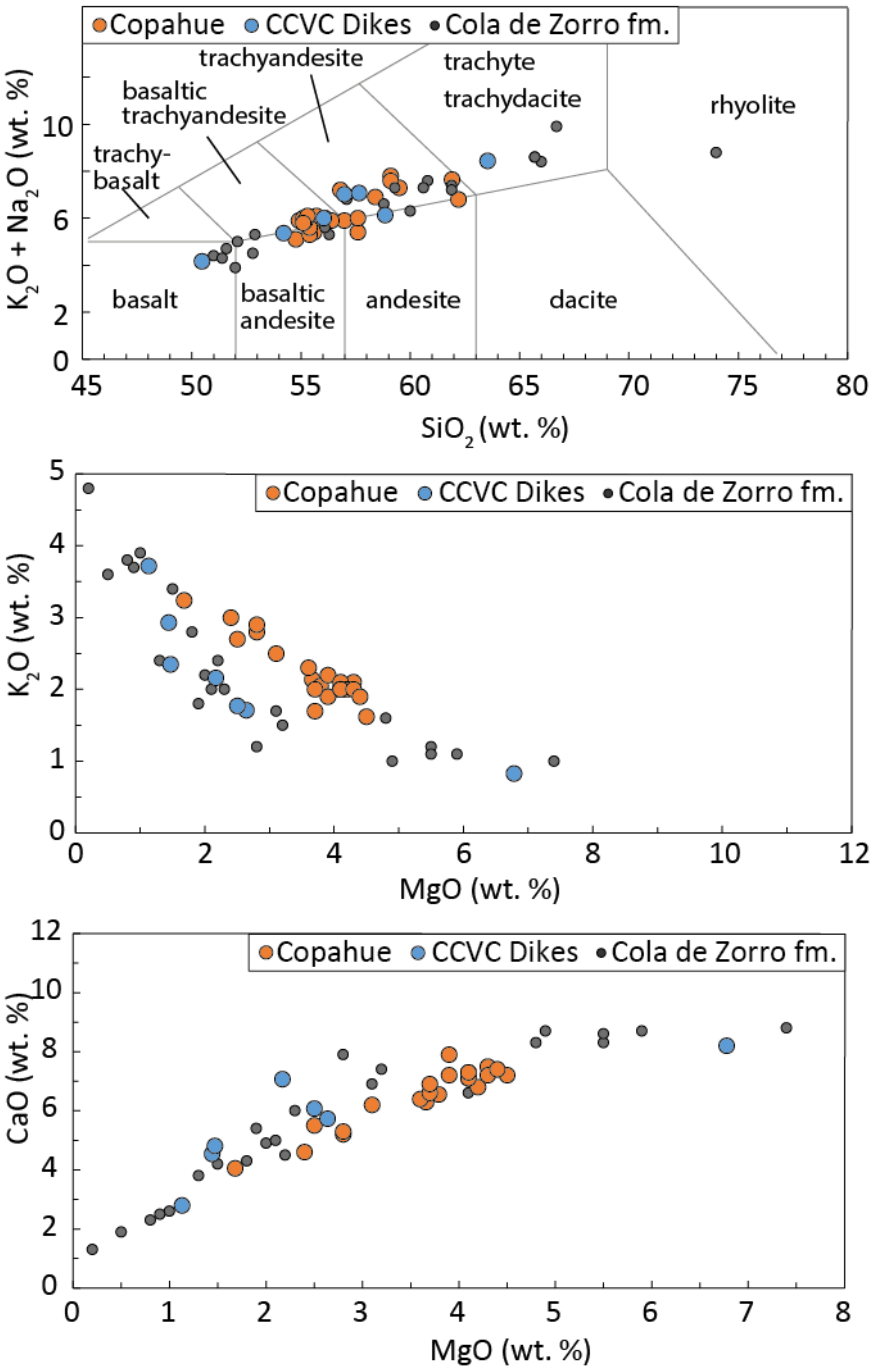

Figure 4.5: Major element concentrations and rock classification after le Bas et al. (1986) of dikes in the walls of the Caviahue depression (blue dots), Copahue volcano (orange dots; Varekamp et al., 2006 and this study) and the Cola de Zorro formation (grey dots; Varekamp et al., 2006) with respect to SiO_2 and MgO.

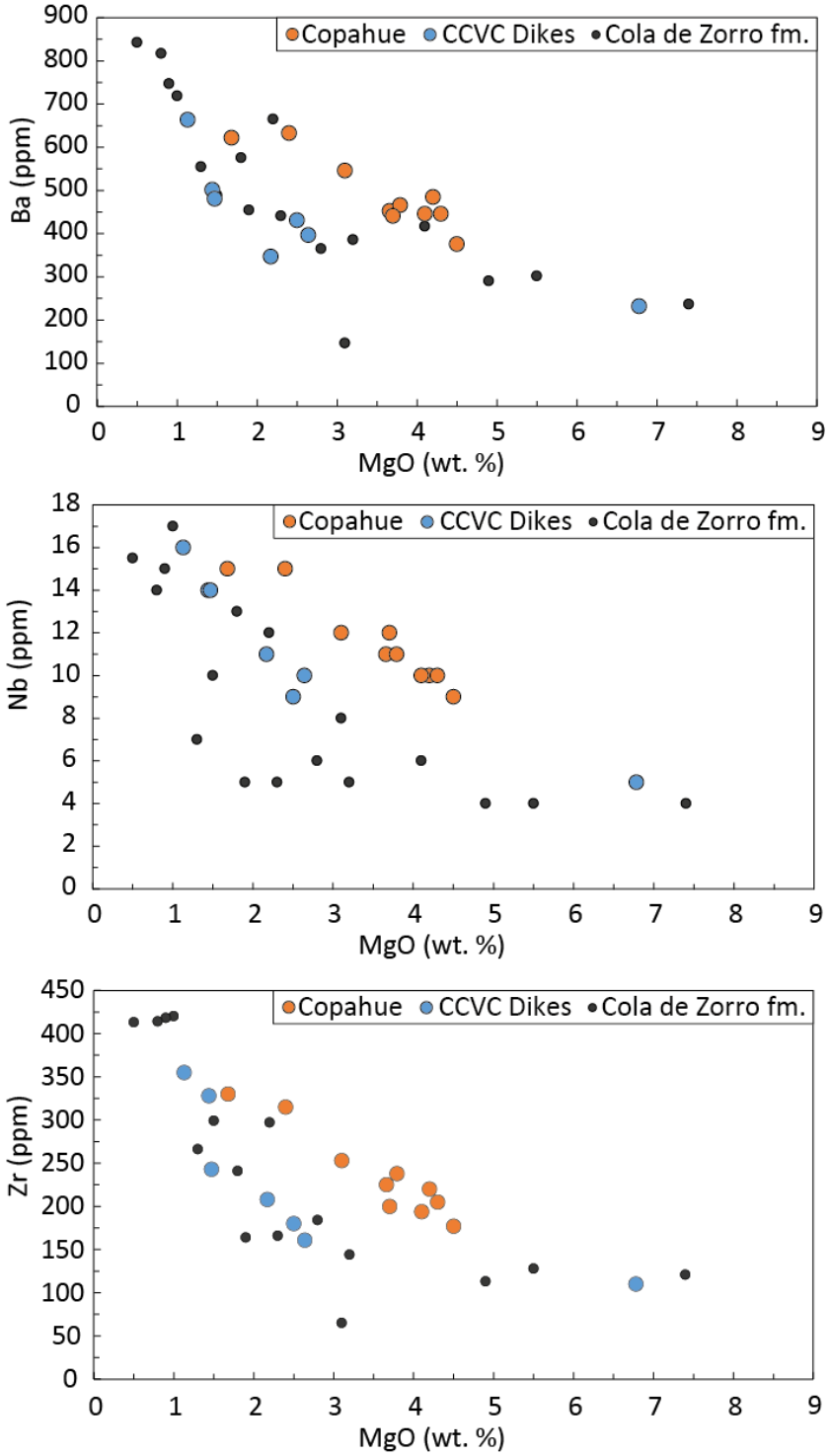

Figure 4.6: Trace element abundances of dikes in the walls of the Caviahue depression (blue dots), Copahue volcano (orange dots; Varekamp et al. 2006 and this study), and the Cola de Zorro formation (grey dots; Varekamp et al. 2006) plotted against MgO content.

trachyandesites and trachydacites (Fig. 4.5). Major element compositions of samples dikes show similar characteristics as lavas of the nearby Copahue volcano (Fig. 4.5). K_2O and Na_2O increase while CaO and Al_2O_3 decrease with decreasing MgO content (Fig. 4.5; Table 4.1). Dikes thereby show lower K_2O- and slightly increased CaO-values at low MgO contents compared to Copahue lavas (Fig. 4.5, Table 4.1).

4.5.4 Trace elements

Trace element concentrations for basaltic to andesitic dikes in the walls of the Caviahue depression are shown in Table 4.2. Sampled dikes show a positive correlation between incompatible trace elements with decreasing MgO content (Fig. 4.6). LILE- and HFSE-concentrations of dikes are similar to lava flows and volcaniclastic deposits of the Cola de Zorro formation and slightly depleted compared to Copahue lavas (Fig. 4.6, Table 4.2). Dikes share the same Zr/Nb and Ba/Nb ratios as lavas of Copahue volcano (Fig. 4.7). Conversely, Zr/Nb and Ba/Nb ratios of the Cola de Zorro formation sampled by Varekamp et al. (2006) show a moderately decreasing trend with increasing Nb-content and generally enhanced ratios compared to measured dikes and Copahue lavas (Fig. 4.7).

4.6 Discussion

Results of this study provide first comprehensive data on dikes associated with the CCVC. Due to a lack radiometric ages, the emplacement age of the dikes can only be determined from field relations. As dikes within the walls of the Caviahue depression are observed to cut 5.6 ± 0.1 Ma to 4 ± 0.1 Ma volcano-sedimentary sequences of the Cola de Zorro formation (Muñoz and Stern, 1988; Linares et al., 1999), a maximum age of 4 Ma may be inferred. A confinement of dike outcrops to the wall rocks of the Caviahue depression (Fig 4.2) indicates an emplacement prior to formation of the depression. As estimated ages for the formation of the Caviahue depression range from 2 Ma to 0.1 Ma (Linares et al., 1999; Hernando et al., 2020), emplacement of dikes in the walls of the Caviahue depression likely occurred between 4 Ma and 0.1 Ma. Dikes identified on satellite images in the Sierra Mandolegüe are however confined by Pleistocene to Holocene volcanic rocks (Fig.

4.2). As Holocene volcanic activity to the east of the CCVC, including the Sierra Mandolegüe, is however restricted to cinder cones and local lava flows (Varekamp et al., 2010; Rojas Vera et al., 2010, 2014), dike outcrops surrounding the CCVC have likely not been covered by Holocene volcanic activity and may thus also be of Pliocene to Pleistocene age.

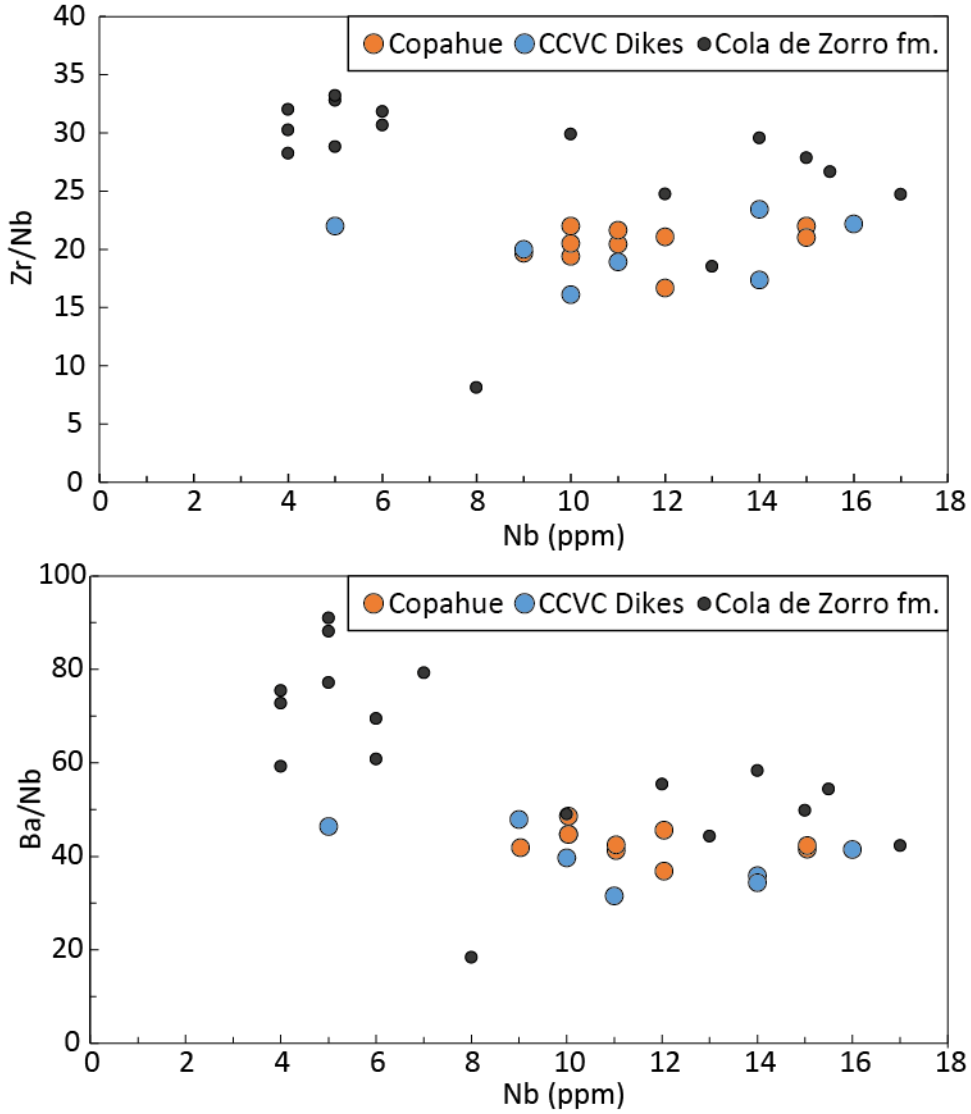

Figure 4.7: Zr/Nb and Ba/Nb ratios of dikes in the walls of the Caviahue depression (blue dots), Copahue volcano (orange dots; Varekamp et al., 2006 and this study) and the Cola de Zorro formation (grey dots; Varekamp et al., 2006).

4.6.1 Geochemical characteristics

With basaltic to trachydacitic compositions, Copahue lavas and dikes in the walls of the Caviahue depression represent the entire spectrum of volcanic rocks characterizing the Southern Volcanic Zone (Stern, 2004; Jacques et al., 2013). Similar major element concentrations of sampled dikes with respect to MgO as Lavas of Copahue volcano and the Cola de Zorro formation (Fig. 4.5; Varekamp et al., 2006), demonstrate their affiliation to the Copahue Caviahue eruptive system.

Contrary to similarities in major element concentrations, decreased LILE and HFSE concentrations of the Cola de Zorro formation and sampled dikes compared to Copahue lavas, along with low Zr/Nb- and Ba/Nb-ratios of dikes and Copahue lavas document a change in the sources contributing to the melt reservoir coeval with the onset of the Copahue eruptive series. Within the SVZ, decreasing Zr/Nb and Ba/Nb ratios are well documented with increasing distance from the Chile trench (Jacques et al., 2013; Rojas Vera et al., 2014). Volcanoes of the arc front hereby show Zr/Nb and Ba/Nb values of around 30 and 50 to 150 respectively which decrease to Zr/Nb ratios of around 10 and Ba/Nb ratios of less than 40 in the back-arc (Jacques et al., 2013; Rojas Vera et al., 2014). This trend of decreasing Zr/Nb and Ba/Nb is generally attributed to a decreasing influence of slab-derived fluid flux with increasing distance from the trench, resulting in lower degrees of mantle melting. Following this interpretation, low Zr/Nb and Ba/Nb ratios of Plio-Pleistocene dikes in the walls of the Caviahue depression and Pleistocene-Holocene Copahue lavas compared to the early Pliocene Cola de Zorro formation (Fig. 4.7) indicate a decrease in slab-derived fluid flux during the late Pliocene to Pleistocene. Similarly, Varekamp et al. (2006) interpreted differences in trace element and isotopic signatures of rocks of the Cola de Zorro formation and Copahue volcano as a decreasing influence of fluid flux from the subducted plate and an increasing contribution of partially melted subducted sediments to the melt reservoir over time. Changes in the trace element concentrations of the CCVC may thus record proposed Miocene to Pliocene steepening of the subducted slab coeval with a change from late Miocene flat-slab subduction to the current plate configuration (Kay et al., 2006; Folguera et al., 2010).

4.6.2 Dike emplacement

Optimal partitioning of dikes in the walls of the Caviahue depression into two clusters (Fig. 4.3c) implies an emplacement in two distinct events. The gridled shape of Cluster 1 hereby demonstrates an emplacement of included dikes under high magma pressure compared to regional stresses, or under a low stress ratio (Fig. 4.3c; Jolly and Sanderson, 1997; Yamaji and Sato, 2011; Yamaji, 2016). Conversely, the narrow, circular shape of cluster 2 indicates an emplacement under low magma pressure or high stress ratio (Fig. 4.3c). However, a definition of the latter by merely 17 dikes with a moderate membership to the cluster (colour coded poles in Fig. 4.3c), compared to 53 dikes defining cluster 1, demonstrates weak partitioning of the dataset. Additional data may thus be necessary to confirm the presence of two distinct dike clusters. As dikes demarcating cluster 2 share a membership to cluster 1, we favour emplacement of dikes in the Walls of the Caviahue depression in one event characterized by increased magma pressure or a low stress ratio ϕ.

Tightly clustering dike trends in the surrounding of the Caviahue depression compared to distributed orientations of dikes inside the depression (Fig 4.3b; Fig. 4.4) indicate an emplacement of dikes in the walls of the Caviahue depression under enhanced magma pressure as indicated by the gridled distribution of cluster 1. In this regard, field observations and numerical models demonstrate that increased magma pressure of a shallow crustal magma chamber may alter the regional stress trajectories which commonly results in diverse trends of dikes with moderate inclination above the magma chamber, termed inclined sheets (e. g. Gudmundsson, 2002; Gudmundsson et al., 2014). Thus, diversely oriented dikes, emplaced in the wall rocks of the Caviahue depression, likely represent inclined sheets emplaced above an upper crustal magma chamber at the location of the Caviahue depression (Fig. 4.8). The presence of a high pressure, shallow crustal magma chamber coeval with dike-emplacement, which marks the last volcanic activity prior to formation of the Caviahue depression, may provide indirect evidence for an origin of the depression as a collapse caldera. Dikes in the surrounding of the depression remained largely unaffected by the local alteration of the stress field resulting in less to non-deviating dike trends.

4.6.3 Regional stress field

Contrary to the NE- and SE-trending σ_{1H}-axes inferred from dikes exposed the depression walls (Fig. 4.3c), trends of dikes surrounding the Caviahue depression indicate σ_{1H}-axes trending ENE and ESE (Fig. 4.4). While the local stress field at the Caviahue depression was likely altered during dike emplacement, dikes surrounding the depression may accurately portray the regional stress field. ENE- and ESE-trending σ_{1H}-axes are both consistent with roughly arc-orthogonal compressions of the upper crust and agree well with roughly E-W-trending Miocene to recent σ_{1H}-axes inferred from dikes in the Malargüe fold-and-thrust belt north of our study area (Barrionuevo et al., 2019). Similar present day σ_{1H}-axes obtained from borehole breakouts in the Neuquén basin (Guzmán et al., 2007) and Quaternary vent alignments of the Payún Matrú Volcanic Field (Hernando et al., 2014) indicate that the stress field characterized by roughly E-W-oriented σ_{1H}-axes has prevailed from the Miocene to present. Coeval with Pliocene slab-steepening, Folguera et al. (2010) and Rojas Vera et al. (2010, 2014), however, propose a transition from Miocene shortening to Pliocene to present upper-crustal extension,

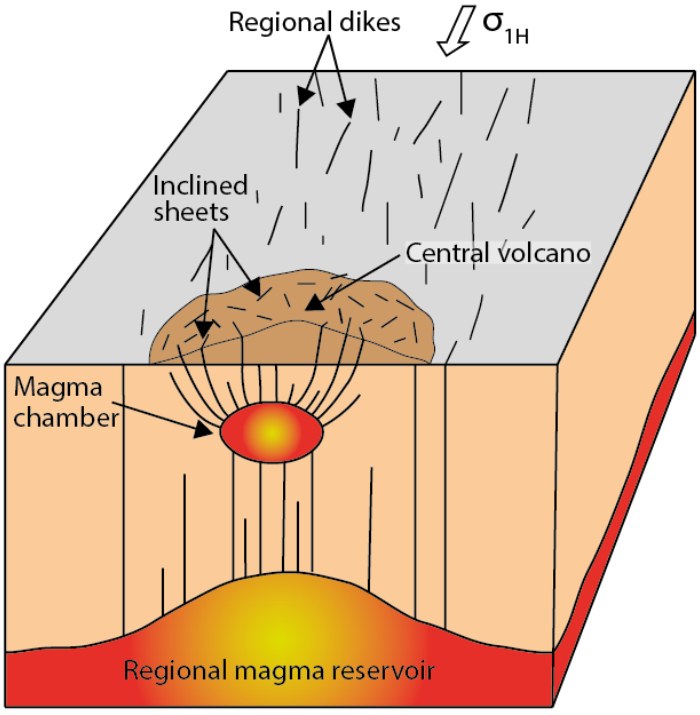

Figure 4.8: Schematic illustration of inclined sheets above a shallow crustal magma chamber modified after Gudmundsson et al. (2014).

which resulted in the opening of the Loncopué Trough, located just east of the CCVC. Considering that Pliocene to Pleistocene dikes surrounding the CCVC did not emplace during an intermittent period of shortening, roughly E-W-trending σ_{1H}-axes demonstrate that proposed Pliocene changes in the subduction geometry likely occurred without market changes to the orientation of σ_{1H}-axes. Consequently, Miocene to Pliocene change from upper-crustal shortening to extension in the Southern Andes may thus have been achieved through a mere switch from a vertically oriented σ_3-axis to a horizontal orientation.

4.7 Conclusion

First comprehensive data from basaltic to trachyandesitic dikes in the vicinity of the Copahue Caviahue volcanic complex compliment the volcanic history of this complex and provide constrains for the upper crustal stress field along the western slope of the Southern Andes. Despite a lack of radiometric ages, field relations indicate a Pliocene to Pleistocene age of dikes in the walls of the Caviahue depression. Decreased Zr/Nb and Ba/Nb ratios of Copahue lavas and dikes document a diminishing fluid flux from the subducted slab resulting in lower degrees of mantle melting. Distributed orientations of dikes in the walls of the Caviahue depression are consisted with an emplacement as inclined sheets above a shallow crustal magma chamber. Corroborated by previous studies, surface trends of dikes surrounding the depression indicate a Miocene to present regional stress field characterized by ENE- and ESE-trending σ_{1H}-axes. Miocene to Pliocene change from upper-crustal shortening to extension in the Southern Andes has thus liekly been achieved through a mere switch from a vertically oriented σ_3-axis to a horizontal orientation without a markedly changing the orientation of σ_{1H}-axes.

5 Conclusion

This thesis addresses kinematic partitioning of deformation in the Southern Andes and the apparent northward translation of crust along the Liquiñe-Ofqui fault zone by means of remote sensing, reassessment of exhumation rates, scaled analogue modelling, and a field-based study of regional dikes. Lineaments extracted from digital elevation models of the Southern Andes are used to constrain the upper-crustal fault-pattern. Extracted lineaments, the majority of which coinciding with mapped faults, show the Southern Andes dissected by an interconnected network of arc-parallel and arc-oblique faults. Here, offset of arc-oblique lineaments on the LOFZ is consistent with proposed predominate right-lateral displacement on the LOFZ. Overall, the observed lineament pattern, corroborated by published fault-slip data, provides evidence for distributed deformation in the Southern Andes resolved on numerous arc-parallel and arc-oblique first-order faults aside from the LOFZ, which collectively encompass the entire southern Andean cordillera.

Exhumation rates calculated from published apatite fission track and (U-Th)/He ages show Miocene to Pliocene enhanced exhumation in the central portion of the Southern Andes which diminishes to the East and West. Here, changes between domains characterized by enhanced and reduced exhumation coincide with extracted NW-, NE-, and N-S-trending lineaments. These changes in exhumation rate are interpreted to result from vertical offset along reverse faults, confirming local observations of transpressive deformation on margin-parallel and margin-oblique faults. In summary, these observations indicate distributed transpressive deformation affecting the entire Southern Andes with the maximal vertical extrusion of rocks occurring along the volcanic arc.

Analogue models tailored to the kinematic boundary conditions of the Southern Andes serve to investigate the progression of southern Andean deformation. Model results show the evolution of a central deformation zone in an early phase defined by reverse faults oriented perpendicular to the convergence vector and a late phase characterized by reverse displacement on faults parallel to an inclined piston, simulating the plate interface. Similarities in the orientation and kinematics of model faults with major faults in the Southern Andes suggest an

analogous two-stage evolution of southern Andean faults. Here, displacement of WNW-striking faults by N-S-striking ones supports an early formation margin-oblique faults similar to model piston-oblique faults. Based on the orientation of the former with respect to the plate margin an onset of deformation under increased convergence-obliquity, likely during the Eocene to Oligocene is proposed.

Aside from slip on major upper-crustal faults, model results, corroborated by paleomagnetic data from the Southern Andes show a significant portion of deformation accommodated through pervasive clockwise rotation of crust which may account for sinistral displacement on WNW-striking faults. Collectively, structural and kinematic similarities between analogue models and the Southern Andes support the observation of distributed transpressive deformation in the Southern Andes.

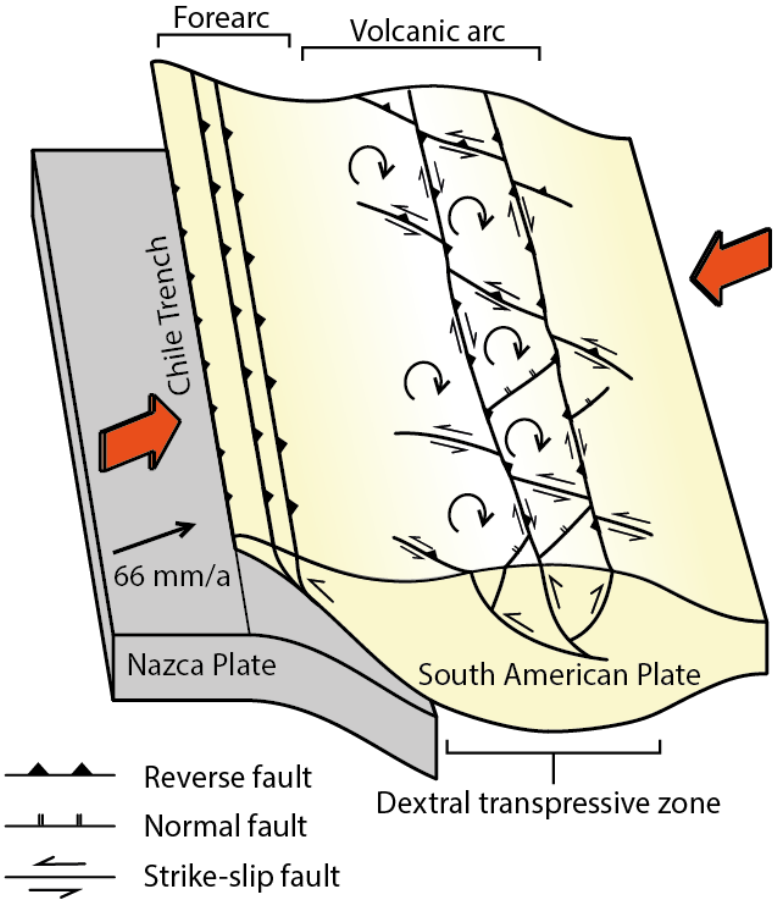

Figure 5.1: Schematic illustration highlighting the northward displacement of crust through clockwise rotation, margin-oblique sinistral reverse faults, and margin-parallel reverse faults, collectively forming an intra-arc dextral transpressive zone.

In contrast to the previously proposed rigid-body translation of a forearc-sliver solely on the Liquiñe-Ofqui fault zone, combined results of analogue modelling and remote sensing indicate northward displacement of crust accommodated on an orogen-wide dextral transpressive zone. This scenario removes the long-standing controversy of a lacking impediment or buttress in the Southern Andes, hampering northward translation of crust. Within the proposed orogen-wide dextral transpressive zone, WNW-striking sinistral reverse faults are capable of accommodating margin-parallel shortening within the overriding plate (Fig. 5.1).

Dikes associated with the Copahue Caviahue volcanic complex, located at the norther terminus of the Liquiñe-Ofqui fault zone, are used to constrain the Neogene upper-crustal stress field in the northern portion of the Southern Andes. Despite a lack of radiometric ages, field relations of dikes in the walls of the Caviahue depression indicate a Pliocene to Pleistocene age. Trace element ratios of dikes document a decreasing degree of mantle melting resulting from a diminishing fluid flux from the subducted slab, coeval with a proposed Miocene to Pliocene slab-steepening. Corroborated by previous studies, trends of regional dikes surrounding the Copahue Caviahue volcanic complex indicate a regional stress field characterized by ENE- and ESE-trending maximum compressive stress-axes (σ_{1H}). Deviating orientations of dikes in the walls of the Caviahue depression are interpreted to have resulted from a local alteration of the regional stress field due to the presence of a shallow crustal magma chamber. In contrast to previous studies which provided evidence for late Miocene to present extension in the Southern Andes, roughly E-W-trending σ_{1H}-axes inferred from regional dikes are consistent with arc-orthogonal compression indicating that proposed Miocene to Pliocene changes in the subduction geometry did not result in a reorientation of σ_{1H}-axes. Trends of dikes surrounding the CCVC thus demonstrate that a shift from Miocene shortening to proposed Pliocene to present extension was likely achieved through a switch of the σ_3-axis-orientation from vertical to horizontal.

6 Acknowledgements

Writing this thesis would not have been possible without the much-appreciated help from numerous people. First, I would like to thank my supervisor Prof. Dr. Ulrich Riller who guided me through the last three years. Ulrich not only gave me the opportunity to write this thesis but also taught me everything I know about scientific work with great patience and commitment. Conduction of analogue experiments would not have been possible without the support of Oliver Eisermann who provided greatly to the development and preparation of experimental setups. In addition, I thank Oliver for his help with the evaluation of experimental result and for our countless discussions about modelling southern Andean deformation. I thank Prof. Dr. Stefan Jung and Dr. Ivan Petrinovic for their help with the interpretation of geochemical data. Catalina Balbis, Irene Hernando, and Joachin Bucher are thanked for a wonderful field season in Caviahue and for sharing their knowledge on the Copahue Caviahue volcanic complex with me. Endless discussions with my fellow Felix Schulte provided inspiration and motivation to continue working during every episode of the last three years. Thank you, Felix for patiently listening to all my ideas without complaining even once. Jan Majewski is thanked for his help with the modification of Matlab code. Thalita Knauer assisted the extraction of dike traces from satellite images. This Project was funded by the German Science Foundation (DFG). I thank Japan's Ministry of Economy, Trade, and Industry (METI) and NASA for the provision of digital elevation models.

7 References

Adriasola AC, Thomson SN, Brix MR, Hervé F, Stöckhert B (2005) Postmagmatic cooling and late Cenozoic denondation of the North Patagonian Batholith in the Los Lagos region of Chile, 41°-42°15'S. International Journal of Earth Sciences 95:504-528

Aguirre L, Hervé F, Godoy E (1972) Distribution of metamorphic facies in Chile: - an outline. Krystalinikum 9:7-19

Angermann D, Klotz J, Reigber C (1999) Space-geodetic estimation of the Nazca-South America Euler vector. Earth and Planetary Science Letters 171:329-334

Assumpção M, Feng M, Tassara A, Julià J (2013) Model crustal thickness for South America from seismic refraction, receiver and surface wave tomography. Tectonophysics 609:82-96

Báez AD, Báez W, Caselli AT, Martini MA, Sommer CA (2020) The glaciovolcanic evolution of the Copahue volcano, Andean Southern Volcanic Zone, Argentina-Chile. J. Volcanol. Geoth. Res. 396:106866

Balbis C, Petrinovic IA, Guzmán S (2016) A contribution to the hazards assessment at Copahue volcano (Argentina-Chile) by facies analysis of a recent pyroclastic density current deposit. J. Volcanol. Geoth. Res. 327:288–298

Barrientos SE, Ward SN (1990) The 1960Chile earthquake—inversion for slip distribution from surface deformation. Geophysical Journal International 103:589–598

Barrionuevo M, Giambiagi L, Mescua JF, Suriano J, de la Cal H, Soto JL, Lossada AC (2019) Miocene deformation in the orogenic front of the Malargüe fold-and-thrust belt (35°30'-36°S: Controls on the migration of magmatic and hydrocarbon fluids. Tectonophysics 766:480-499

Bechis F, Encinas A, Concheyro A, Litvak AV, Aguirre-Urreta B, Ramos VA (2014) New age constraints for the Cenozoic marine transgression of northwestern Patagonia, Argentina (41°-43°S): Paleogeographic and tectonic implications. Journal of South American Earth Sciences 52:72-93

Beck ME (1983) On the mechanism of tectonic transport in zones of oblique subduction. Tectonophysics 93:1–11

Beck ME (1991) Coastwise transport reconsidered: Lateral displacements in oblique subduction zones, and tectonic consequences. Physics of the Earth and Planetary Interiors 68:1–8

Beck ME, Rojas C, Cembrano J (1993) On the nature of buttressing in margin-parallel strike-slip fault systems. Geology 21:755-758

Beck ME, Burmester RF, Steele BC (1998) Paleomagnetism of probably remagnetized late Mesozoic volcanic rocks near Lago Verde, Aisén, Southern Chile. Andean Geology 25:153–163

Beck ME, Burmester R, Cembrano J, Drake R, Garcia A, Hervé F, Munizaga F (2000) Paleomagnetism of the North Patagonian batholith, southern Chile. An exercise in shape analysis. Tectonophysics 326:185-202

Bilek SL (2010) Invited review paper: Seismicity along the South American subduction zone: Review of large earthquakes, tsunamis, and subduction zone complexity. Tectonophysics 495:2-14

Bilmes A, D'Elia L, Lopez L, Richiano S, Varela A, Alvarez MP, Bucher J, Eymard I, Muravchik M, Franzese J, Ariztegui D (2019) Digital outcrop modelling using "structure-frommotion" photogrammetry: acquisition strategies, validation and interpretations to different sedimentary environments. Journal of South American Earth Sciences 96:102325

Bird P (2003) An updated digital model of plate boundaries. Geochemistry Geophysics Geosystems 4:1027

Bohm M, Lüth S, Echtler H, Asch G, Bataille K, Bruhn C, Rietbrock A, Wigger P (2002) The Southern Andes between 36° and 40°S latitude: seismicity and average seismic velocities. Tectonophysics 356:275-289

Breitesprecher K, Thorkelson DJ (2009) Neogene kinematic history of Nazca-Antarctic-Phoenix slab windows beneath Patagonia and the Antarctic Peninsula. Tectonophysics 464:10-20

Brooks B, Bevis M, Smalley R, Kendrick E, Manceda R, Lauría E, Maturana R, Araujo M (2003) Crustal motion in the Southern Andes (26°-36°S): Do the Andes behave like a microplate? Geochemistry Geophysics Geosystem 4:1085

Burns MW, Jordan T, Copeland P, Kelley SA (2006) The case for extensional tectonics in the Oligocene-Miocene Southern Andes as recorded in the Cura Mallin basin (36°-38°S). In: Kay SM, Ramos VA (eds.) Evolution of an Andean margin: A tectonic and magmatic view from the Andes to the Neuquén Basin (35°-39°S lat). Geological Society of America, pp 163-184

Cande SC, Leslie RB (1986) Late Cenozoic tectonics of the southern Chile Trench, Journal of Geophysical Research 91:471–496

Catalán N, Bataille K, Araya R (2017) Depth-dependent geometry of the Liquiñe-Ofqui fault zone and its relation to paths of slab-derived fluids. Geophysical Research Letters 44:916-920

Cembrano J, Hervé F (1993) The Liquiñe Ofqui Fault Zone: A major Cenozoic strike slip duplex in the southern Andes. In: Abstracts – International Symposium on Andean Geodynamics II, Off. de la Rech. Sci. et Tech. d'Outre-mer (ORSTOM), Paris, pp 175 –178

Cembrano J, Beck ME, Burmester RF, Rojas C, Garcia A, Herve F (1992) Paleomagnetism of lower Cretaceous rocks from east of the Liquiñe-Ofqui fault zone, southern Chile: Evidence of small in-situ clockwise rotations. Earth and Planetary Science Letters 113:539–551

Cembrano J, Hervé F, Lavenu A (1996) The Liquiñe-Ofqui fault zone: A long lived intraarc fault system in southern Chile. Tectonophysics 259:55–66

Cembrano J, Schermer E, Lavenu A, Sanhueza A (2000) Contrasting nature of deformation along an intra-arc shear zone, Liquiñe-Ofqui fault zone, southern Chilean Andes. Tectonophysics 319:129–149

Cembrano J, Lavenu A, Reynolds P, Arancibia G, López G, Sanhueza A (2002) Late Cenozoic transpressional ductile deformation north of the Nazca – South America – Antarctica triple junction. Tectonophysics 354:289–314

Cembrano J, González G, Arancibia G, Ahumada I, Olivares V, Herrera V (2005) Fault zone development and strain partitioning in an extensional strike-slip duplex: a case study from the Mesozoic Atacama fault system, Northern Chile. Tectonophysics 400:105–125

Chemenda A, Lallemand S, Bokun A (2000) Strain partitioning and interplate friction in oblique subduction zones: Constraints provided by experimental modeling. Journal of Geophysical Research 105:5567–5581

Chen W-Y, Wu J, Suppe J (2019) Southwards propagation of Nazca subduction along the Andes. Nature 565:441447

Christeleit EC, Brandon MT, Shuster D (2017) Miocene development of alpine glacial relief in the Patagonian Andes, as revealed by low-temperature thermochronometry. Earth and Planetary Science Letters 460:152-163

Cross TA, Pilger RH (1982) Controls of subduction geometry, location of magmatic arcs, and tectonics of arc and back-arc regions. Geological Society of America Bulletin, Vol. 93:545–562

Davies BJ, Darvill CM, Lovell H et al. (2020) The evolution of the Patagonian Ice Sheet from 35 ka to the present day (PATICE). Earth Science Reviews 204:103152

Delaney PT, Pollard DD, Ziony JI, McKee EH (1986) Field Relations between Dikes and Joints: Emplacement Processes and Paleostress Analysis. Journal of Geophysical Research 91:4920-4938

DeMets C, Gordon RG, Argus DF, Stein S (1994) Effect of recent revisions to the geomagnetic reversal time scale on estimates of current plate motions, Geophysical Research Letters 21:2191–2194

DeMets C, Gorden RG, Argus DF (2010) Geologically current plate motions. Geophysical Journal International 181:1-80

Dewey JF, Lamb SH (1992) Active tectonics of the Andes. Tectonophysics, Vol. 205:79-95

Dietz RS (1961) Continent and ocean basin evolution by spreading of the seafloor. Nature 190:854-857

Dewey JF, Holdsworth RE, Strachan RA (1998) Transpression and transtension zones. Geological Society, London, Special Publications 135:1-14

Diraison M, Cobbold PR, Rossello EA, Amos AJ (1998) Neogene dextral transpression due to oblique convergence across the Andes of northwestern Patagonia, Argentina. Journal of South American Earth Sciences 11:519-532

Diraison M, Cobbold PR, Gapais D, Rosello EA, Le Corre C (2000) Cenozoic crustal thickening, wrenching and rifting in the foothills of the southernmost Andes. Tectonophysics 216:91-119

Doglioni C, Carminati E, Cuffaro M, Scrocca D (2007) Subduction kinematics and dynamic constraints. Earth-Science Reviews 83:125–175

Echaurren A, Folguera A, Gianni G, Orts D, Tassara A, Encinas A, Giménez M, Valencia V (2016) Tectonic evolution of the North Patagonian Andes (41°-44° S) through recognition of syntectonic strata. Tectonophysics 677-678:99-114

Encinas A, Sagripanti L, Rodríguez MP, Orts D, Anavalón A, Giroux P, Otero J, Echaurren A, Zambrano P, Valencia V (2020) Tectonosedimentary evolution of the Coastal Cordillera and Central Depression of south-Central Chile (36°30'-42°S). Earth-Science Reviews 213:103465

Fick SE, Hijmans RJ (2017) WorldClim 2: new 1-km spatial resolution climate surfaces for global land areas. International Journal of Climatology 37:4302-4315

Fitch TJ (1972) Plate convergence, transcurrent faults, and internal deformation adjacent to southeast Asia and the western Pacific. Journal of Geophysical Research 77:4432–4460

Folguera A, Ramos VA (2000) Control estructural del volcán Copahue (38°S-71°W): implicancias tectónicaspara el arco volcánico cuaternario (36–39°S). Revista de la Asociación Geológica Argentina 55:229–244

Folguera A, Rojas Vera E, Bottesi G, Zamora Valcarce G, Ramos VA (2010) The Loncopué Trough: a Cenozoic basin produced by extension in the southern Central Andes. J. Geodyn. 49:287–295

Folguera A, Rojas Vera E, Vélez L, Tobal J, Orts D, Agusto M, Caselli A, Ramos VA (2015) A Review of the Geology, Structural Controls; and Tectonic Setting of Copahue Volcano, Southern Volcanic Zone, Andes, Argentina in Tassi F, et al. (eds.) Copahue Volcano, Active Volcanoes of the World, Springer, Berlin Heidelberg, pp 3-22

Folguera A, Naipauer M, Sagripanti L, Ghiglione MC, Orts DL, Giambiagi L (2016a) An Introduction to the Southern Andes (33-50°S): Book Structure. In: Folguera A, Naipauer M, Sagripanti L, Ghiglione MC, Orts DL, Giambiagi L (eds.) Growth of the Southern Andes, Springer Earth System Sciences, Heidelberg, pp 1-7

Forsyth D, Uyeda S (1975) On the Relative Importance of the Driving Forces of Plate Motion. Geophysical Journal International 43:163-200

Forsythe R, Nelson E (1985) Geological manifestations of ridge collision: Evidence from the Golfo de Penas-Taitao Basin, southern Chile. Tectonics 4:477-495

Galland O, Cobbold PR, de Bremond d'Ars J, Hallot E (2007a) Rise and emplacement of magma during horizontal shortening of the brittle crust: Insights from emperimental modelling. J. Geophys. Res. 112

Galland O, Hallot E Cobbold PR, Ruffet G, de Bremond d'Ars J (2007b) Volcanism in a compressional Andean setting: A structural and geochronological study of Tromen volcano (Neuquén province, Argentina). Tectonics 26

Galland O, Holohan E, de Vries, BW, Burchardt S (2015) Laboratory modelling of volcano plumbing systems: a review. In: Breitkreuz C, Rocchi S (eds.) Physical Geology of Shallow Magmatic Systems, Dykes, Sills and Laccoliths, Heidelberg, Springer, pp 147-214

Gansser A (1973) Facts and theories on the Andes. J. Geol. Soc. London 129:93–131

Garcia A, Beck ME, Burmester R, Munizaga F, Herve F (2011) Pelomagnetic reconnaissance of the region de los Lagos, southern Chile, and its tectonic implications. Revista geológica Chile 15:13–30

Georgieva V, Melnick D, Schildgen TF, Ehlers TA, Lagabrielle Y, Enkelmann E, Strecker MR (2016) Tectonic control on rock uplift, exhumation, and topography above an oceanic ridge collision: Southern Patagonien Andes (47°S), Chile. Tectonics 35:1317-1341

Giacosa RE, Heredia C (2004) Structure of the North Patagonian thick-skinned fold-and-thrust belt, southern central Andes, Argentina (41°-42°S). Journal of South American Earth Sciences 18:61-72

Glodny J, Echtler H, Collao S, Ardiles M, Burón P, Figueroa O (2008) Differential Late Paleozoic active margin evolution in South-Central Chile (37°S–40°S) – the Lanalhue Fault Zone. Journal of South American Earth Sciences 26:397-411

Gripp AE, Gordon RG (1990) Current plate velocities relative to the hotspots incorporating the NUVEL-1 global plate motion model. Geophysical Research Letters 17:1109–1112

Gudmundsson A (2002) Emplacement and arrest of sheets and dykes in central volcanoes. Journal of Volcanology and Geothermal Research 116:279-298

Gudmundsson A, Lecoeur N, Mohajeri N, Thordarson T (2014) Dike emplacement at Bardarbunga, Iceland, induces unusual stress changes, caldera deformation, and earthquakes. Bull. Volcanol. 76:869

Gutscher MA (2002) Andean subduction styles and their effect on thermal structure and interpolate coupling. Journal of South American Earth Sciences 15:3-10

Gutscher MA, Malavieille J, Lallemand S, Collot JY (1999) Tectonic segmentation of the North Andean Margin: Impact of the Carnegie Ridge collision. Earth and Planetary Science Letters 168:255-270

Guzmán C, Cristallini E, Bottesi G (2007) Contemporary stress orientations in the Andean retroarc between 34 S and 39 S from borehole breakout analysis. Tectonics 26:TC3016

Harland WB (1971) Tectonic transpression in Caledonian Spitzbergen. Geological Magazine 108:27–42

Hayes GP, Wald DJ, Johnson RL (2012) Slab 1.0: A three-dimensional model of global subduction zone geometries. Journal of Geophysical Research 117:B1

Heaton TH, Hartzell (1987) Earthquake Hazards of the Cascadia Subduction Zone. Science 236:162-168

Heit B, Yuan X, Bianchi M, Sodoudi F, Kind R (2008) Crustal thickness estimation beneath the southern central Andes at 30°S and 36°S from S wave receiver function analysis. Geophysical Journal International 174:249-254

Hein AS, Dunai TJ, Hulton NRJ, Xu S (2011) Exposure dating outwash gravels to determine the age of the greatest Patagonian glaciations. Geology 39:103-106

Herman F, Brandon M (2015) Mid-latitude glacial erosion hotspot related to equatorial shifts in southern Westerlies. Geology 43:987-990

Hernandez-Moreno C, Speranza F, Di Ciara A (2014) Understanding kinematics of intra-arc transcurrent deformation: Paleomagnetic evidence from the Liquiñe-Ofqui fault zone (Chile, 38-41°S). Tectonics 33:1964-1988

Hernando IR, Franzese JR, Llambías EJ, Petrinovic IA (2014) Vent distribution in the Quaternary Payún Matrú Volcanic Field, westernArgentina: Its relation to tectonics and crustal structures. Tectonophysics 622:122-134

Hernando I, Bucher J, del Papa CE, Eisermann JO, Göllner PL, Guzmán SR, Balbis C, Petrinovic IA (2020) Unraveling the timing of the Caviahue depression, Andean Southern Volcanic Zone: insights from the sedimentary infill. International Journal of Earth Sciences

Hervé M (1976) Estudio geológico de la falla Liquiñe-Reloncaví en la área de Liquiñe: Antecedentes de un movimiento transcurrente (Provincia de Vadivia). Actas Congreso Geológico Chileno 1:39–56

Hervé F, Pankhurst RJ, Drake R, Beck ME, Mpodozis C (1993) Granite generation and rapid unroofing related to strike-slip faulting, Aysén, Chile. Earth and Planetary Science Letters 120:375–386

Hervé F, Pankhurst RJ, Fanning CM, Calderón M, Yaxley GM (2007) The South Patagonian batholith: 150 my of granite magmatism on a plate margin. Lithos 97:373-394

Hess HH (1962) History of Ocean Basins. In: Engle AEJ, James HL, Leonard BL (eds.) Petrologic Studies: A Volume in Honor of A. F. Buddington, Geological Society of America, New York, pp 599–620

Heuret A, Lallemand S (2005) Plate motions, slab dynamics and back-arc deformation. Physics Earth Planetary International 149:31–51

Hoffmann-Rothe A, Kukowski N, Dresen N, Echtler G, Oncken O, Klotz J, Scheuber E, Kellner A (2006) Oblique convergence along the Chilean margin: Partitioning, margin-parallel faulting and force interaction at the plate interface. In: Oncken O (ed) The Andes: Active Subduction Orogeny, Springer, Berlin, Heidelberg, pp 125–146

Horton B (2018) Tectonic Regimes of the Central and Southern Andes: Responses to Variations in Plate Coupling During Subduction. Tectonics 37:402-429

Jacques G, Hoernle K, Gill J, Hauff F, Wehrmann H, Garbe-Schönberg D, van den Bogaard P, Bindeman I, Lara LE, (2013) Across-arc geochemical variations in the Southern Volcanic Zone, Chile (34.5–38.0°S): constraints on mantle wedge and slab input compositions. Geochim. Cosmochim. Acta 123:218–243

Jarrard RD (1986) Relations among subduction parameters. Reviews of Geophysics 24:217–284

Jolly RJH, Sanderson DJ (1997) A Mohr circle construction for the opening of a pre-existing fractures. Journal of Structural Geology 19:887–892

Jordan TE, Burns WM, Veiga R, Pángaro F, Copeland P, Kelley S, Mpodozis C (2001) Extension and basin formation in the southern Andes caused by increased convergence rate: A mid-Cenozoic trigger for the Andes. Tectonics 20:308-324

Kay SM, Burns M, Copeland P (2006) Upper Cretaceous to Holocene Magmatism over the Neuquén basin: evidence for transient shallowing of the subduction zone under the Neuquén Andes (36◦S to 38◦S latitude). In: Kay SM, Ramos VA (eds.) Evolution of an Andean Margin: A Tectonic and Magmatic View from the Andes to the Neuquén Basin (35–39◦S), Geological Society of America Special Paper 407, pp 19–60

Kimura G (1986) Oblique subduction and collision: Forearc tectonics of the Kuril arc. Geology 14:404-407

Klotz J, Khazaradze G, Angermann D, Reigber C, Perdomo R, Cifuentes O (2001) Earthquake cycle dominates contemporary crustal deformation in Central and Southern Andes. Earth Planetary Science Letters 193:437-446

Lagabrielle Y, Suarez M, Rossello EA, Herail G, Martinod J, Regnier M, de la Cruz R (2004) Neogene to Quaternary tectonic evolution of the Patagonian Andes at the latitude of the Chile Triple Junction. Tectonophysics 385:211-241

Lallemand S, Heuret A, Boutelier D (2005) On the relationships between slab dip, back-arc stress, upper plate absolute motion, and crustal nature in subduction zones. Geochemistry, Geophysics, Geosystems 6:10.1029

Lange D, Cembrano J, Rietbrock A, Haberland C, Dahm T, Bataille K (2008) First seismic record for intra-arc strike-slip tectonics along the Liquiñe-Ofqui fault zone at the obliquely convergent plate margin of the southern Andes. Tectonophysics 455:14-24

Lara LE, Cembrano J, Lavenu A (2008) Quaternary vertical displacement along the Liquiñe-Ofqui fault zone: Differential uplift and coeval volcanism in the Southern Andes? International Geology Review 50:975-993

Lavenu A, Cembrano J (1999) Compressional- and transpressional-stress pattern for Pliocene and Quaternary brittle deformation in fore arc and intra-arc zones (Andes of central and southern Chile). Journal of Structural Geology 21:1669–1691

Linares E, Ostera HA, Mas LC (1999) Cronología potasio-argón del Complejo Efusivo Copahue-Caviahue, provincia del Neuquén. Revista de la Asociación Geológica Argentina 54:240–247

Martin MW, Kato TT, Rodriguez C, Godoy E, Duhart P, McDonough M (1999) Evolution of the late Paleozoic accretionary complex and overlying forearc-

magmatic arc, south central chile (38°-41°S): Constraints for the tectonic setting along the southwestern margin of Gondwana. Tectonics 18:582- 605

Mazzoni M, Licitra DT (2000) Significado estratigráfico y volcanológico de depósitos de flujos piroclásticos neógenos con composición intermedia en la zona del lago Caviahue, provincial del Neuquén. Revista de la asociación Geológica Argentina 55:188–200

McCaffrey R (1992) Oblique plate convergence, slip vectors, and forearc deformation. Journal of Geophysical Research 97:8905–8915

McCaffrey R, Zwick P, Bock Y, Prawirodirdjo L, Genrich J, Puntodewo SSO, Subarya C (2000) Strain partitioning during oblique plate convergence in northern Sumatra: Geodetic and seismologic constraints and numerical modelling. Journal of Geophysical Research 105:363–376

Melnick D, Echtler HP (2006) Morphotectonic and geologic digital map compilations of the south-central Andes (36°–42°S). In: Oncken O (ed) The Andes: Active Subduction Orogeny, Springer, Berlin, Heidelberg, pp 125–146

Melnick D, Folguera A, Ramos VA (2006b) Structural control on arc volcanism: the Caviahue-Copahue complex, Central to Patagonian Andes transition. J. S. Am. Earth Sci. 22:66–88

Melnick D, Rosenau M, Folguera A, Echtler H (2006c) Neogene tectonic evolution of the Neuquén Andes western flank (37–39S). In: Kay SM, Ramos VA (eds.) Evolution of an Andean margin: A tectonic and magmatic view from the Andes to the Neuquén Basin (35–39S lat), Geological Society of America Special Paper 407, pp 73–95

Melnick D, Bookhagen B, Strecker MR, Echtler HP (2009) Segmentation of megathrust rupture zones from fore-arc deformation patterns over hundreds to millions of years, Arauco peninsula, Chile. Journal of Geophysical Research 114:B01407

Moreno M, Melnick D, Rosenau M, Bolte J, Klotz J, Echtler H, Baez J, Bataille K, Chen J, Bevis M, Hase H, Oncken O (2011) Heterogeneous plate locking in the South–Central Chile subduction zone: Building up the next great earthquake. Earth and Planetary Science Letters 305:413-424

Muñoz J, Niemeyer H (1984) Petrología de la Formación Trapa-Trapa y consideraciones acerca del volcanismo Mioceno entre los 36 y 39° Lat. S (Cordillera Principal). Revista Geológica de Chile 23:53-67

Muñoz Bravo J, Stern CR (1988) The Quaternary volcanic belt of the southern continental margin of South America: Transverse structural and petrochemical

variations across the segment between 38°S and 39°S. J. S. Am. Earth Sci. 1:147–161

Nocquet JM, Villegas-Lanza JC, Chlieh M, Mothes PA, Rolandone F, Jarrin P, Cisneros D, Alvarado A, Audin L, Bondoux F, Martin X, Font Y, Régnier M, Vallée M, Tran T, Beauval C, Maguiña Mendoza JM, Martinez W, Tavera H, Yepes H (2014) Motion of continental slivers and creeping subduction in the northern Andes. Nature Geoscience 7:287-291

Oncken O, Hindle D, Kley J, Elger K, Victor P, Schemmann K (2006) Deformation of the Central Andean upper plate system – facts, fiction, and constraints for plateau models. In: The Andes-Active Subduction Orogeny, Oncken O, Chong G, Franz G, Giese P, Götze H-J, Ramos VA, Strecker MR, Wigger P (eds.) Frontiers in Earth Sciences Series 1, Springer, Berlin, pp 3–27

Orts D, Folguera A, Encinas A, Ramos M, Tobal J, Ramos VA (2012) Tectonic development of the North Patagonian Andes and their related Miocene foreland basin (41°30'-43°S). Tectonics 31:TC3012

Orts DL, Folguera A, Giménez M, Ruiz F, Rojas Vera EA, Lince Klinger F (2015) Cenozoic building and deformational processes in the North Patagonian Andes. Journal of Geodynamics 86:26-41

Panien M, Schreurs G, Pfiffner A (2006) Mechanical behaviour of granular materials used in analogue modelling: insights from grain characterisation, ring-shear tests and analogue experiments. Journal of Structural Geology 28:1710-1724

Pankhurst R, Hervé F, Rojas L, Cembrano J (1992) Magmatism and tectonics in continental Chiloé, Chile (42° and 42°30´S). Tectonophysics 205:283-294

Pankhurst RJ, Weaver SD, Hervé F, Larrondo P (1999) Mesozoic-Cenozoic evolution of the North Patagonian Batholith in Aysén, southern Chile. J. Geol. Soc. London 156:673-694

Pardo-Casas F, Molnar P (1987) Relative motion of the Nazca (Farallon) and South American plates since Late Cretaceous times. Tectonics 6:233-248

Pérez-Flores P, Cembrano J, Sánchez-Alfaro P, Veloso E, Arancibia G, Roquer T (2016) Tectonics, magmatism and paleo-fluid distribution in a strike-slip setting: Insights from the northern termination of the Liquiñe–Ofqui fault System, Chile. Tectonophysics 680:192-210

Pesce A (1989) Evolución volcano-tectónica del complejo efusivo Copahue-Caviahue y su modelo geotérmico preliminar. Revista de la Asociación Geológica Argentina 44:307–327

Petrinovic IA, D'Elia L, Páez G, Balbis C, Guzmán S, Villarosa G, Carniel R (2014a) Depósito de corriente piroclástica reciente (1963–1964 AD? - 1976 AD?) del

volcán Copahue (I): evidencias geológicas de campo y edad radiocarbónica. Revista de la Asociación Geológica Argentina 71:139–142

Petrinovic IA, Villarosa G, D'Elia L, Guzmán S, Páez GN, Outes V, Manzoni C, Delménico A, Balbis C, Carniel R, Hernando IR (2014b) La erupción del 22 de diciembre de 2012 del volcán Copahue, Neuquén, Argentina: Caracterización del ciclo eruptive y sus productos. Revista de la Asociación Geológica Argentina 71:161–173

Piquer J, Yáñez G, Rivera O, Cooke DR (2019) Long-lived crustal damage zones associated with fault intersections in the high Andes of Central Chile. Andean Geology 46:223-239

Plafker G, Savage JC (1970) Mechanism of the Chilean Earthquake of May 21 and 22, 1960. Geological Society of America Bulletin 81:1-30

Potent S (2003) Kinematik und Dynamik neogener Deformationsprozesse des südzentralchilenischen Subduktionssystems, nördlichste Patagonische Anden (37°-40°S). Dissertation, Universität Hamburg

Potent S, Reuther C-D (2001) Neogene Deformationsprozesse im aktiven magmatischen Bogen Südzentralchiles zwischen 37°S und 39°S. Mitteilungen des Geologisch-Paläontologischen Institutes 85:1-22

Radic JP, Carpinelli A, Zurita E (2000) Cuenca Terciaria Cura-Mallín, informe geológico. Informe inédito SIPETROL S.A., Santiago, Chile

Radic JP, Rojas L, Carpinelli A, Zurita E (2002) Evolución tectónica de la Cuenca de Cura-Mallín, región cordillerana chileno Argentina (36300 S– 39000 S). Proceedings of the 15th Congreso Geológico Argentino, El Calafate 3:233–237

Ramos VA (1999) Plate tectonic setting of the Andean Cordillera. Episodes 22:183–190

Ramos VA (2009) Anatomy and global context of the Andes: Main geologic features and the Andean orogenic cycle. In: Kay SM, Ramos VA, Dickinson WR (eds.) Backbone of the Americas: Shallow Subduction, Plateau Uplift, and Ridge and Terrane Collision, Geological Society of America Memoir 204, pp 31-65

Ramos VA (2010) The tectonic regime along the Andes: Present-day and Mesozoic regimes. Geological Journal 45:2-25

Ramos VA, Folguera A (2009) Andean flat-slab subduction through time. In: Murphy JB, Keppie JD, Hynes AJ (eds) Ancient Orogens and Modern Analogues. Geological Society, London, Special Publications 327:31–54

Rapela CW, Pankhurst RJ (1992) The granites of northern Patagonia and the Gastre Fault System in relation to the break-up of Gondwana. Geological Society Special Publication 68:209-220

Reutter KJ, Scheuber E, Chong G (1996) The Precordilleran fault system of Chuquicamata, Northern Chile: evidence for reversals along arc-parallel strike-slip faults. Tectonophysics 259:213–228

Richardson RM (1992) Ridge forces, absolute plate motions, and the intraplate stress field. Journal of Geophysical Research 97:11739-11748

Riller U, Oncken O (2003) Growth of the central Andean Plateau by tectonic segmentation is controlled by the gradient in crustal shortening. Journal of Geology 111:367-384

Ritter MC, Leever K, Rosenau M, Oncken O (2016) Scaling the sandbox-Mechanical (dis) similarities of granular materials and brittle rock. Journal of Geophysical Research 121:6863-6879

Robin P-YF, Cruden AR (1994) Strain and vorticity patterns in ideally ductile transpression zones. Journal of Structural Geology 16:447–466

Rojas C, Beck ME, Burmester R (1994) Paleomagnetism of the mid-Tertiary Ayacara Formation, southern Chile: Counterclockwise rotation in a dextral shear zone. Journal of South American Earth Sciences 7:45–56

Rojas Vera EA, Folguera A, Valcarce GZ, Giménez M, Ruiz F, Martínez P, Bottesi G, Ramos VA (2010) Neogene to Quaternary extensional reactivation of a fold and thrust belt: the Agrio belt in the Southern Central Andes and its relation to the Loncopué trough (38°–39°S). Tectonophysics 492:279–294

Rojas Vera EA, Sellés D, Folguera A, Gímenez M, Ruíz F, Orts D, Zamora Valcarce G, Martínez P, Bechis F, Ramos VA (2014) The origin of the Loncopué Trough in the retroarc of the Southern Central Andes from field, geophysical and geochemical data. Tectonophysics 637:1-19

Rojas Vera EA, Mescua J, Folguera A, Becker TP, Sagripanti L, Fennell L, Orts D, Ramos VA (2015) Evolution of the Chos Malal and Agrio fold and thrust belts, Andes of Neuquén: Insights from structural analysis and apatite fission track dating. Journal of South American Earth Sciences 64:418-433

Rojas Vera EA, Orts DL, Folguera A, Zamora Valcarce G, Fennell L, Bottesi G, Chiachiarelli F, Ramos VA (2016) The transitional zone between the southern central and northern Patagonian Andes (36–39°S). In: Folguera A, Naipauer M, Sagripanti L, Ghiglione MC, Orts DL, Giambiagi L (eds.) Growth of the Southern Andes, Springer Earth System Sciences, Heidelberg, pp 99-114

Rosenau M (2004) Tectonics of the southern Andean intra-arc zone (38°–42°S). Dissertation, Freie Universität Berlin

Rosenau M, Melnick D, Echtler H (2006) Kinematic constraints on intra-arc shear and strain partitioning in the southern Andes between 38°S and 42°S latitude. Tectonics 25:TC4013

Sanderson DJ, Marchini WRD (1984) Transpression. Journal of Structural Geology 6:449–458

Santimano T, Rosenau M, Oncken O (2015) Intrinsic versus extrinsic variability of analogue sand-box experiments – Insights from statistical analysis of repeated accretionary sand wedge experiments. Journal of Structural Geology 75:80-100

Schellart W (2000) Shear test results for cohesion and friction coefficients for different granular materials: scaling implications for their usage in analogue modelling. Tectonophysics 324:1-16

Scheuber E, González G (1999) Tectonics of the Jurassic-early Cretaceous magmatic arc of the north Chilean Coastal Cordillera (22°– 26°S): a story of coupling and decoupling in the subduction zone. Tectonics 18:895–910

Schreurs G, et al. (2006) Analogue benchmarks of shortening and extension experiments. In: Buiter SJH, Schreuers G (eds.) Analogue and Numerical Modelling of Crustal-Scale Processes, Geological Society, London, Special Publication 253, pp 1-27

Schueller S, Davy P (2008) Gravity influenced brittle-ductile deformation and growth faulting in the lithosphere during collision. Results from laboratory experiments. Journal of Geophysical Research 113:B12404

Sernageomin (2003) Mapa Geológico de Chile: Versión digital, N°4, CD-ROM versión 1.0. Servicio Nacional de Geología y Minería. Publicación Geológica Digital, Santiago de Chile, Chile

Sielfeld G, Lange D, Cembrano J (2019a) Intra-arc crustal seismicity: seismotectonic implications or the Southern Andes Volcanic Zone, Chile. Tectonics 38:552-578

Sielfeld G, Ruz J, Brogi A, Cembrano J, Stanton-Yonge A, Pérez-Flores P, Iturrieta P (2019b) Oblique-slip tectonics in an active volcanic chain: A case study from the Southern Andes. Tectonophysics 770:228221

Sobolev SV, Babeyko AY (2005) What drives orogeny in the Andes? Geology, Vol. 33:617–620

Somoza R (1998) Updated Nazca (Farallon)–South America relative motions during the last 40 My: Implications for mountain building in the central Andean region. Journal of South American Earth Sciences 11:211–215

Somoza R, Ghidella ME (2012) Late Cretaceous to recent plate motions in western South America revisited. Earth and Planetary Science Letters 332:152-163

Sruoga P, Consoli VC (2011) Nueva edad Ar/Ar para la Formación Las Mellizas. Implicancias en la evolución del complejo Caviahue-Copahue (37° 51'S, 71° 09'O), Provincia de Neuquén. In: Proceedings XVIII Congreso Geológico Argentino, Neuquén, Argentina 10a, pp 512–513

Stanchits S, Mayr S, Shapiro S, Dresen G (2011) Fracturing of porous rock induced by fluid injection. Tectonophysics 503:129–145

Stanton-Yonge A, Griffith WA, Cembrano J, St. Julien R, Iturrieta P (2016) Tectonic role of margin-parallel and margin-transverse faults during oblique subduction in the Southern Volcanic Zone of the Andes: Insights from Boundary Element Modelling. Tectonics 35:1990-2013

Stern RJ (2002) Subduction zones. Reviews of Geology 40:1-38

Stern CR (2004) Active Andean volcanism: its geologic and tectonic setting. Revista Geológica de Chile 31:161-206

Stern CR, Muñoz J, Troncoso R, Duhart P, Crignola P, Farmer GL (2000) Tectonic setting of the mid-Tertiary coastal magmatic belt in South Central Chile: An extensional event related to late Oligocene changes in plate convergence rate and subduction geometry. Actas - Congr. Geol. Chil. IX 2:693-696

Tassara A, Yáñez G (2003) Relación entre el espesor elástico de la litósfera y la segmentación tectónica del margen andino (15–47°S). Rev. Geol. de Chile 30:159–186

Tassara A, Götze HJ, Schmidt S, Hackney R (2006) Three-dimensional density model of the Nazca plate and the Andean continental margin. Journal of Geophysical Research 111:B09404

Thomson SN (2002) Late Cenozoic geomorphic and tectonic evolution of the Patagonian Andes between latitudes 42 and 46 S: An appraisal based on fission-track results from the transpressional intra-arc Liquiñe-Ofqui fault zone. Geological Society of America Bulletin 114:1159–1173

Tibaldi A, Pasquarè F, Tormey D (2010) Volcanism in Reverse and Strike-Slip Fault Settings. In: Cloctingh S, Negendank J (eds.) Frontiers in Integrated Solid Earth Sciences, International Year of Planet Earth, Springer Heidelberg, Berlin, pp 315-348

Tikoff B, Teyssier C (1994) Strain modeling of displacement field partitioning in transpressional orogens. Journal of Structural Geology 16:1575–1588

Tomlinson AJ, Blanco N (1997) Structural evolution and displacement history of the West Fault system, Precordillera, Chile: part I, synmineral history. In: VIII Congresso Geológico Chileno, ACTAS Vol III – Nuevos Antecedentes de la Geología del Distrio de Chuquicamata, Periodo 1994–1995, Sesión 1: Geología Regional, Universidad Catolica del Norte, pp 1873–1877

Umino S, Kusano Y, Yamaji A, Fudai T, Tamura A, Arai S (2020) The conversion tectonics from spreading to subduction: Paleostress analysis of dike swarms during the subduction initiation in the Oman Ophiolite. Geological Society of America Bulletin 132:1333-1343

Varekamp JC, deMoor JM, Merrill MD, Colvin AS, Goss AR, Vroon PZ, Hilton DR (2006) Geochemistry and isotopic characteristics of the Caviahue-Copahue volcanic complex, Province of Neuquén, Argentina. Geol. Soc. Am. 407:317

Varekamp JC, Hesse A, Madeville CW (2010) Back-arc basalts from the Loncopue graben (Province of Neuquen, Argentina). Journal of Volcanology and Geothermal Research 197:313-328

Vergara M, Muñoz J (1982) La Formación Cola de Zorro en la alta cordillera Andina Chilena (36°-39°lat. S), sus características petrográficas y petrológicas. Revista Geológica de Chile 17:31-46

Vine FJ, Matthews DH (1963) Magnetic Anomalies over Oceanic Ridges. Nature 199:947-949

Wang K (1996) Simplified analysis of horizontal stresses in a buttressed forearc sliver at an oblique subduction zone. Geophysical Research Letters 23:2021-2024

Wang K, Hu Y, Bevis M, Kendrick E, Smalley R, Barriaga Vargas R, Lauría E (2008) Crustal motion in the zone of the 1960 Chile earthquake: Detangling earthquake-cycle deformation and forearc-sliver translation. Geochemistry Geophysics Geosystems 8:Q10010

Wang K, Hu Y, He J (2012) Deformation cycles of subduction earthquakes in a viscoelastic Earth. Nature 484:327-332

Watson DF, Philip GM (1985) A Refinement of Inverse Distance Weighted Interpolation. Geoprocessing 2:315-327

Wegener A (1912) Die Entstehung der Kontinente. Geologische Rundschau 3:276-292

Willet SD, Brandon MT (2013) Some analytical methods for converting thermochronometric age to erosion rate. Geochemistry Geophysics Geosystems 14:209-222

Willner AP, Hervé F, Thomson SN, Massone HJ (2003) Juxtaposition of different HP/LT metamorphic units during subduction erosion in a Mesozoic accretionary belt (Diege de Almagro Island/Southern Chile; 51°30'). Terra Nostra 2:86-87

Willner AP, Hervé F, Massone HJ (2000) Mineral chemistry and pressuretemperature evolution of two contrasting highpressure-low-temperature belts in the Chonos Archipelago, Southern Chile. J. Petrol. 41:309-330

Willner AP, Glodny J, Gerya TV, Godoy E, Massone HJ (2004) A counterclockwise PTt path of high-pressure/low-temperature rocks from the Coastal cordillera accretionary complex of south-central Chile: constraints for the earliest stage of subduction mass flow. Lithos 75:283-310

Yamaji A (2016) Genetic algorithm for fitting a mixed Bingham distribution to 3D orientations: a tool for the statistical and paleostress analyses of fracture orientations. The Island Arc 25:72–83

Yamaji A, Sato K (2011) Clustering of fracture orientations using a mixed Bingham distribution and its application to paleostress analysis from dike or vein orientations. Journal of Structural Geology 33:1148– 1157

Yañez G, Cembrano J (2004) Role of viscous plate coupling in the late Tertiary Andean tectonics. Journal of Geophysical Research 109:B02407

Zamora Valcarce G, Zapata T, del Pino D, Ansa A (2010) Structural evolution and magmatic characteristics of the Agrio fold-and-thrust belt. Geological Society of America Special Paper 407:125-145

Zwaan F, Schreurs G, Adam J (2018) Effects of sedimentation on rift segment evolution and rift interaction in orthogonal and oblique extensional settings: Insights from analogue models analysed with 4D X-ray computed tomography and digital volume correlation techniques. Global and Planetary Change 171:110-133

Appendix I: Supplementary figures to chapter 2

Supplementary Figure 1: Age-elevation (m a.s.l. indicates meters above sea level) relationship of compiled (a) AFT and (b) (U-Th)/He ages with respective error bars.

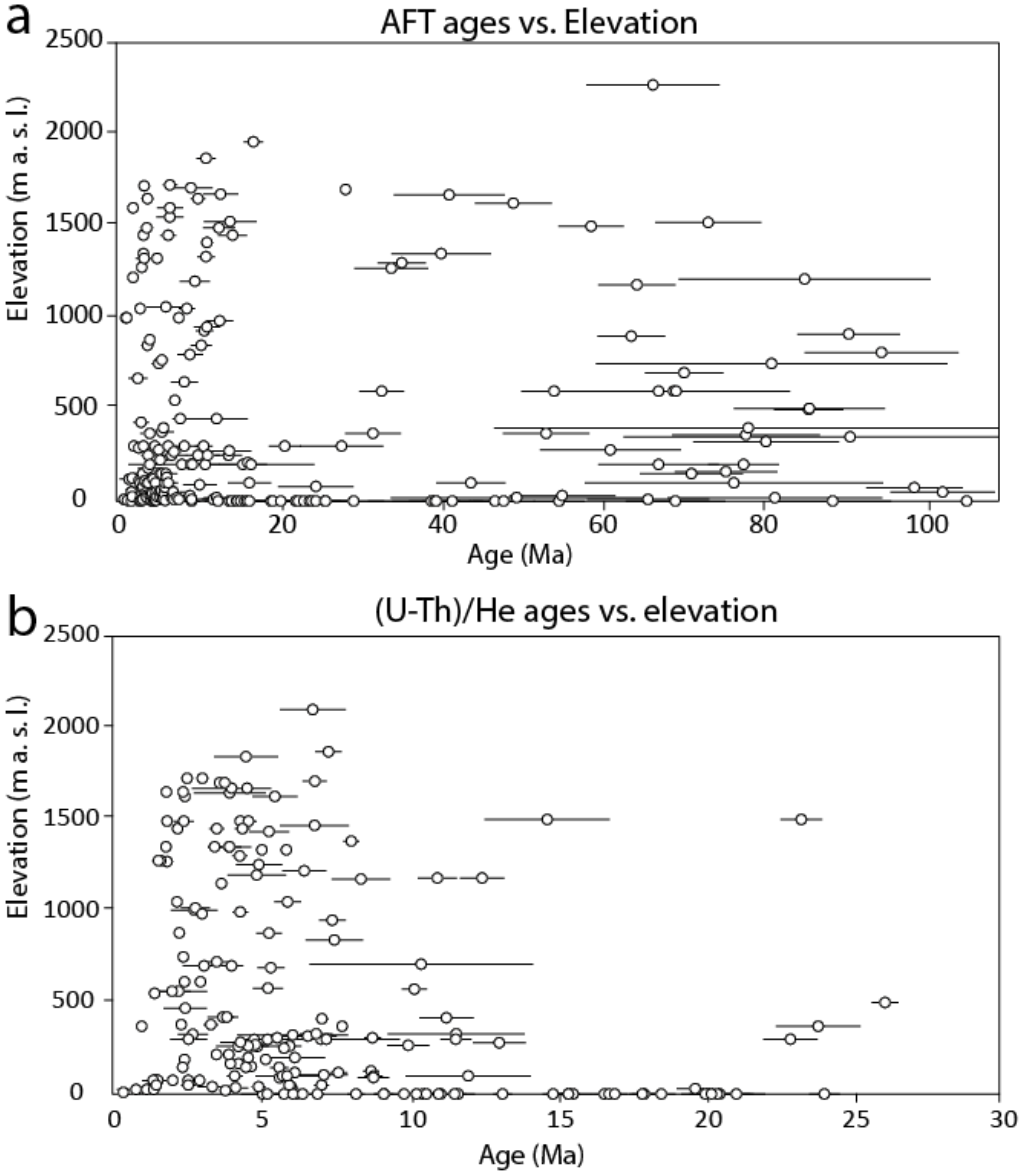

Supplementary Figure 2: Diagrams illustrating the sensitivity of exhumation rates to changes in the geothermal gradient for (a) AFT data and (b) (U-Th)/He data. Data points show deviation in exhumation rate calculated with different geothermal gradients relative to exhumation rates calculated with a gradient of 34°C/km. Data are calculated with selected age-elevation pairs representing the entire spectrum of compiled data presented in this study.

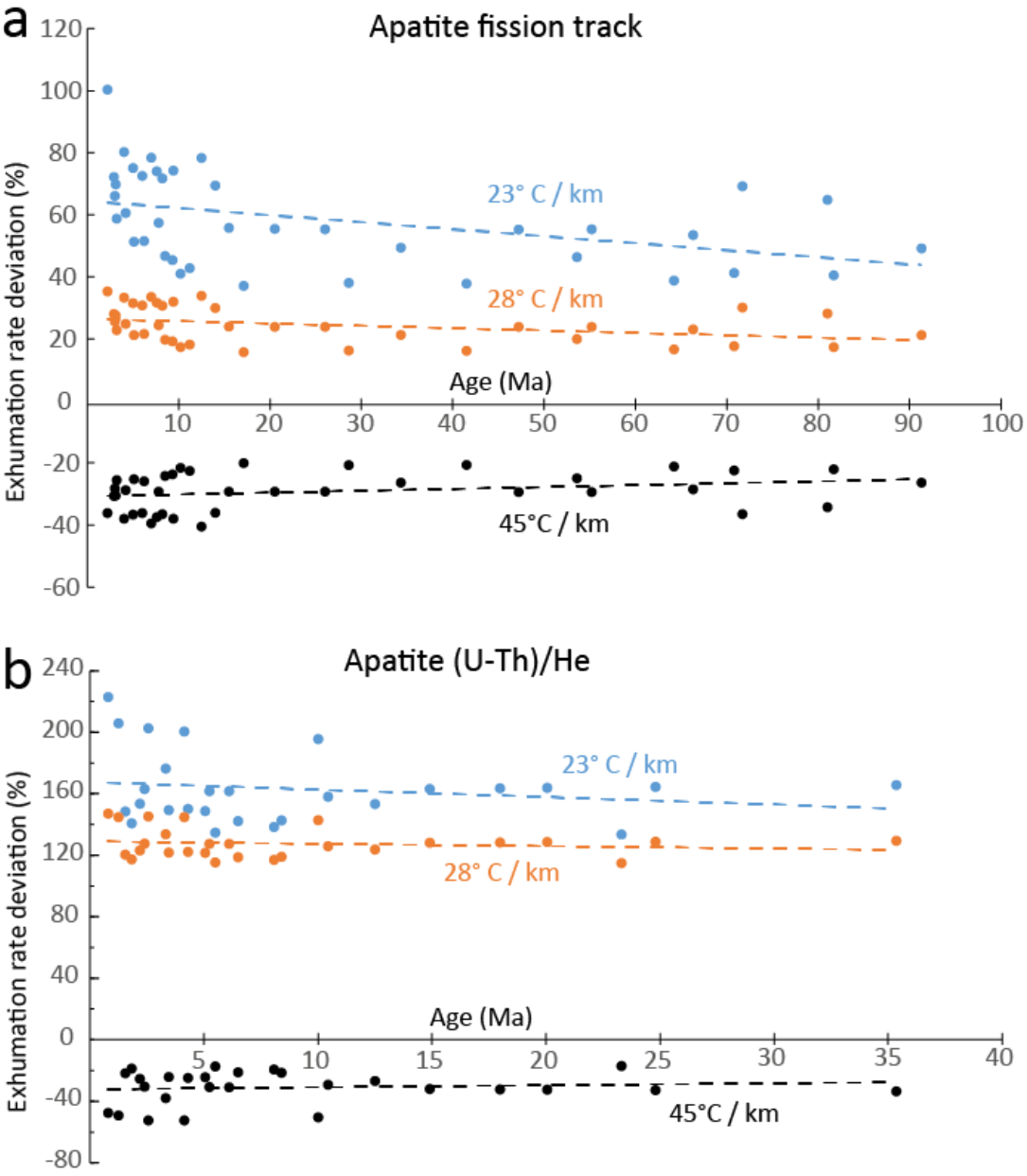

Supplementary Figure 3: Diagrams illustrating the sensitivity of calculated exhumation rates to error of input ages for (a) AFT data and (b) (U-Th)/He data. Similar to Supplementary Figure 2, calculations are based on selected age-elevation pairs representing the entire spectrum of compiled data presented in this study.

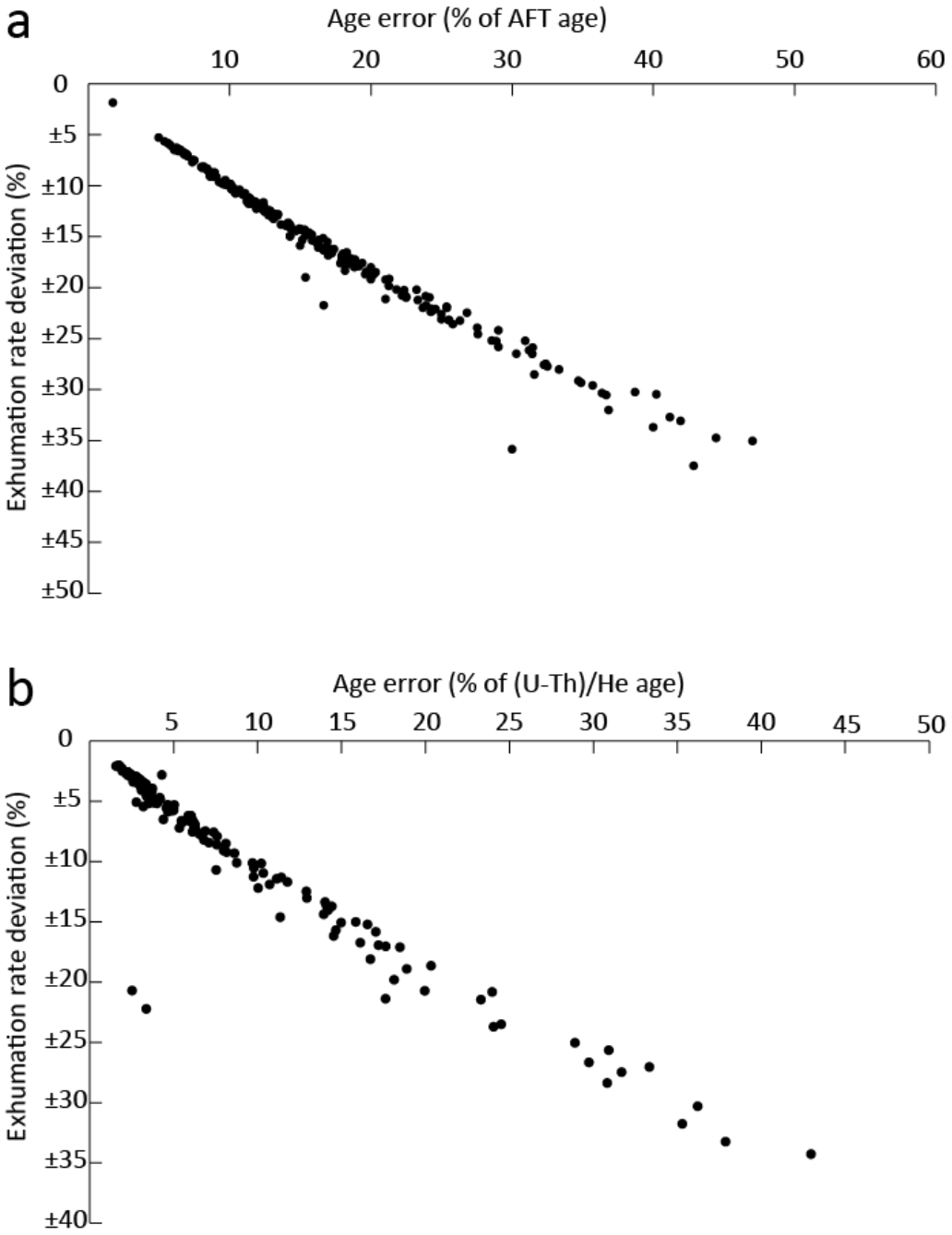

Appendix II: Supplementary methods to chapter 3

Scaling

In order to quantify modeled deformation processes and to ensure that physical laws governing deformation in our models apply to nature, accurate scaling is achieved through identification of the main dimensionless governing parameter for our experimental setup and comparing this parameter with nature (Galland et al. 2015). As the brittle-ductile coupling, expressed as the strength ratio between brittle and ductile material (R) has been shown to greatly influence the outcome of deformation experiments (Schuller and Davy, 2008 and references therein), we consider this ratio as the main dimensionless governing parameter for our experimental setup. Scaling was therefore achieved through similarity of the calculated experimental brittle-ductile strength ratio and the natural equivalent calculated for the Southern Andes. The strength ratio R is defined as the differential stress ratio between a brittle and a ductile layer:

$$\frac{\text{Brittel strength}}{\text{Ductile strength}} = \frac{\int_{\text{brit}}(\sigma_1 - \sigma_3)\,\text{dz}}{\int_{\text{duc}}(\sigma_1 - \sigma_3)\,\text{dz}} = \text{R}$$

The dimensionless differential stress for the brittle layer is expressed as:

$$\int_{\text{brit}}(\sigma_1 - \sigma_3)\,\text{dz} = \int_{\text{brit}} \sin\phi * \rho * g * l_{\text{brit}}\,\text{dz} = \frac{\sin\phi}{2} * \rho * g * l_{\text{brit}}^2$$

Where Φ represents the friction angle, ρ the density and l_{brit} the thickness of the brittle layer. The dimensionless differential stress for the ductile crust is expressed as:

$$\int_{\text{duc}}(\sigma_1 - \sigma_3)\,\text{dz} = \int_{\text{duc}} \eta * \frac{U}{L}\,\text{dz} = \eta * \frac{U}{L} * l_{\text{duc}}\,.$$

Where η represents the viscosity, U the rate of shortening, L the length of the compressing piston, and (l_{duc}) the thickness of the ductile layer. The R-ratio can therefore be expressed as:

$$\frac{\frac{\sin\phi}{2} * \rho * g * l_{brit}^2}{\eta * \frac{U}{L} * l_{duc}} = R$$

Cohesion, density, friction angle, and gravity are constant. The R-ration in our experiments is therefore mainly controlled by varying the thickness of the brittle and ductile layers and the velocity of the compressing pistons. Using a friction angle (Φ) of 30°, a density (ρ) of 2.5 g/cm^3, a thickness (l_{brit}) of 10 km for the upper brittle crust, and a viscosity (η) of 1500 Pa*s, a shortening rate (U) of 30 mm/a, a width (L) of 2000 km, and a thickness (l_{brit}) of 60 km for the lower crust, we calculated a representative R-value of 2.148 for the Southern Andean Volcanic Zone. The thickness of model layers and the piston-velocities were subsequently set to fulfil $R_n = R_m \approx 2.148$. In order to model continental-scale deformation, a thickness (l_m) of 0.7 cm was chosen for the model brittle crust which, for an average thickness (l_n) of 10 km for brittle crust in nature sets the length scale ratio to:

$$l' = \frac{l_m}{l_n} = \frac{0.007}{10000}[\mathrm{m}] = 7\mathrm{x}10^{-7}$$

14.28 km in nature therefore correspond to 1 cm in our model.

In order to maintain $R_n = R_m$, layers were shortened at a constant total shortening rate of U_m = 3.5 cm/h ($U_m = 9.72\mathrm{x}10^{-6}$ m/s). The individual velocities of the pistons (X1 and X2), and the moving box halve (Y) were thereby set to represent the upper crustal deformation field, inferred from GPS velocities (Klotz et al., 2001, Moreno et al., 2011). We consider the crustal deformation inferred from GPS velocities as the best approximation of interseismic upper crustal deformation applied through a locked plate interface available for the Southern Andes. As GPS vectors in the forearc region are oriented parallel to the overall convergence vector between the Nazca and South American plates, we employed a similar convergence vector to our model. The model convergence angle is thereby defined as:

with the convergence velocity given as the vector product of velocities $U_{x2} = X_2$ and $U_y = Y$:

$$\left|\overrightarrow{U_c}\right| = \left|\sqrt{U_{X_2}^2 + U_Y^2}\right|.$$

All scaling parameters of our model setup and their natural equivalent used to calculate the R-value for the Southern Andes are summarized in supplementary table 1.

Analogue materials

Fire-dried, moderately sorted G23T quartz sand with a grain size of 0.6-2.5 mm, a cohesion of ~ 20 Pa and a friction angle of 28.45° (Ritter et al., 2016; Santimano et al., 2015) was used as model upper crust. Despite its slightly coarser grain size, friction and cohesion of G23T quartz sand are similar to commonly used sand in analogue modelling (Ritter et al., 2016, Schreuers et al., 2006). With a densitiy of sand ρ_m = 1562 kg/m^3 and upper crust in nature ρ_n = 2500 kg/ m^3 the density scale ratio amounts to:

$$\rho'_B = \frac{\rho_{\mathrm{B}\,m}}{\rho_{\mathrm{B}\,n}} = \frac{1562}{2500}\left[\frac{\mathrm{kg}}{\mathrm{m}^3}\right] = 0.6248\,.$$

In order to prevent bouyant effects between model upper and lower crust, a mixture of 0.965 kg polydimethylsiloxane (PDMS) type KORASILON Öl G 30 M and 1 kg fine-grained corundum sand was used to model the lower crust. A density of ρ_m = 1600 kg/m^3 and an average density of the lower crust ρ_n = 2800 kg/m^3 set the density scale ratio at:

$$\rho'_{\mathrm{D}} = \frac{\rho_{\mathrm{D}\,m}}{\rho_{\mathrm{D}\,n}} = \frac{1600}{2800}\left[\frac{\mathrm{kg}}{\mathrm{m}^3}\right] = 0.5714\,.$$

With a stress exponent of the PDMS/corundum mixture of n = 1.05, the mixture is a Newtonian fluid with an effective viscosity of η = 1.5x10^5 Pa*s. Considering a viscosity η = 1x10^{22} Pa*s for the lower crust of the southern Andes (Moreno et al., 2001; Wang et al., 2007), the viscosity scale ratio is:

$$\eta' = \frac{\eta_m}{\eta_n} = \frac{1.5\mathrm{x}10^5}{1\mathrm{x}10^{22}}\,[\mathrm{Pa} * \mathrm{s}] = 1.5\mathrm{x}10^{-17}\,.$$

Micro glass beads served as low friction material decoupling the model lower crust from the box-bottom. Covered by a layer of plastic wrap, they remain at the bottom during the experiments. The spherical glass beads have a low friction and cohesion,

are well sorted and range in size from 0.4 mm to 0.8 mm and have a density of ρ_m = 1500 kg/m^3.

Supplementary table 1: Scaling parameters for our model and the Southern Andes with respective scaling factor.

Parameter	Nature	Model	Scaling factor
ϕ	30,00	30,00	1
$\boldsymbol{\rho}$ brittle crust	2500,00	1560,00	0,6240
$\boldsymbol{\rho}$ ductile crust	2800,00	1600,00	0,5714
g [m/s^2]	9,81	9,81	1
d brittle crust [m]	10000,00	0,007	7,00E-07
η [Pa*s]	1,00E+22	1,50E+05	1,50E-17
U [m/s]	9,5129E-10	2,7778E-05	2,92E+04
l [m]	2000000,00	1,00	5,00E-07
d ductile crust [m]	60000,00	0,021	3,50E-07
R	2,148	2,143	0,9977

Appendix III: Supplementary figures to chapter 3

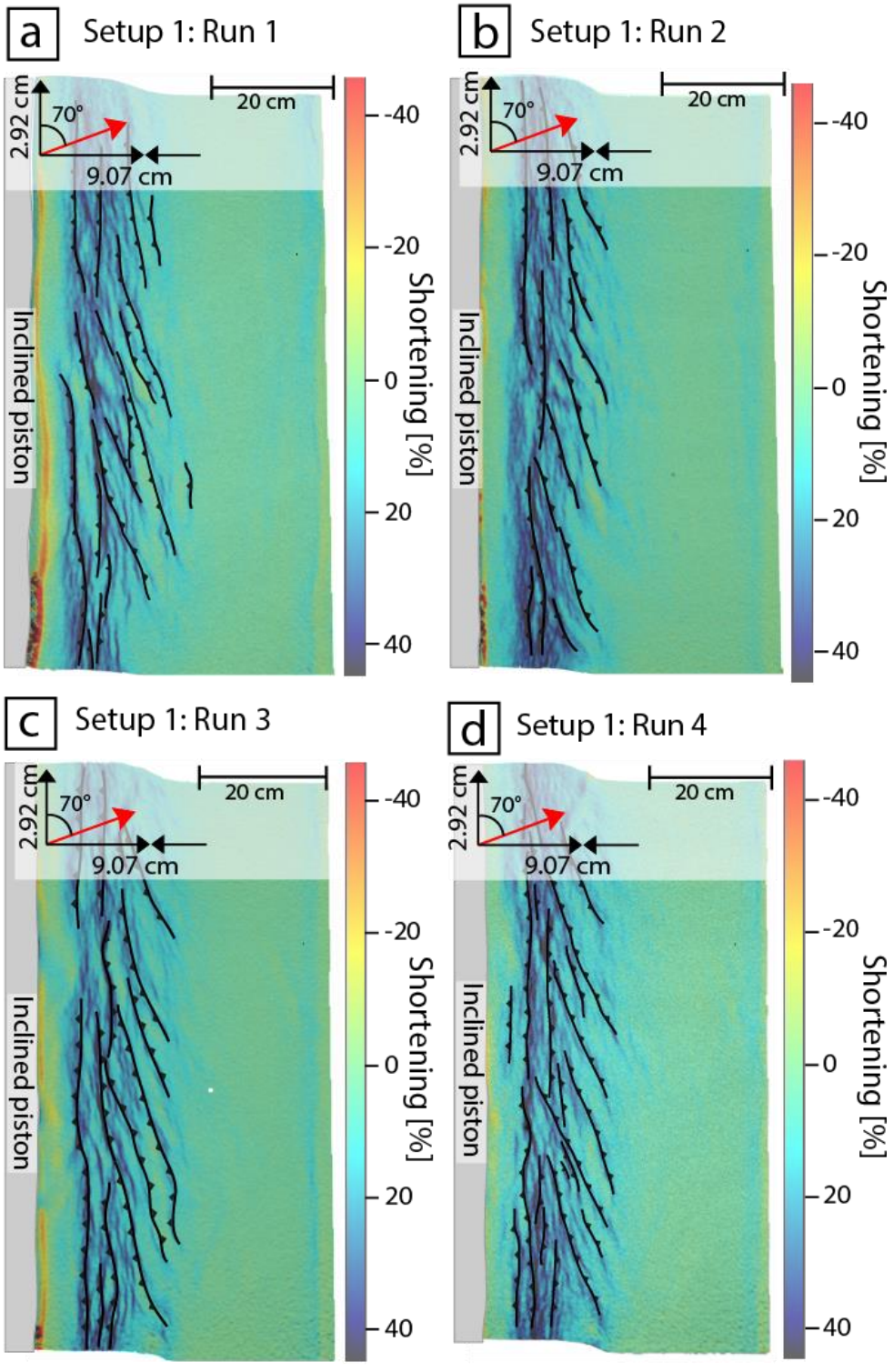

Supplementary figure S1: Cumulative shortening of all four setup 1 experimental runs after 54 minutes.

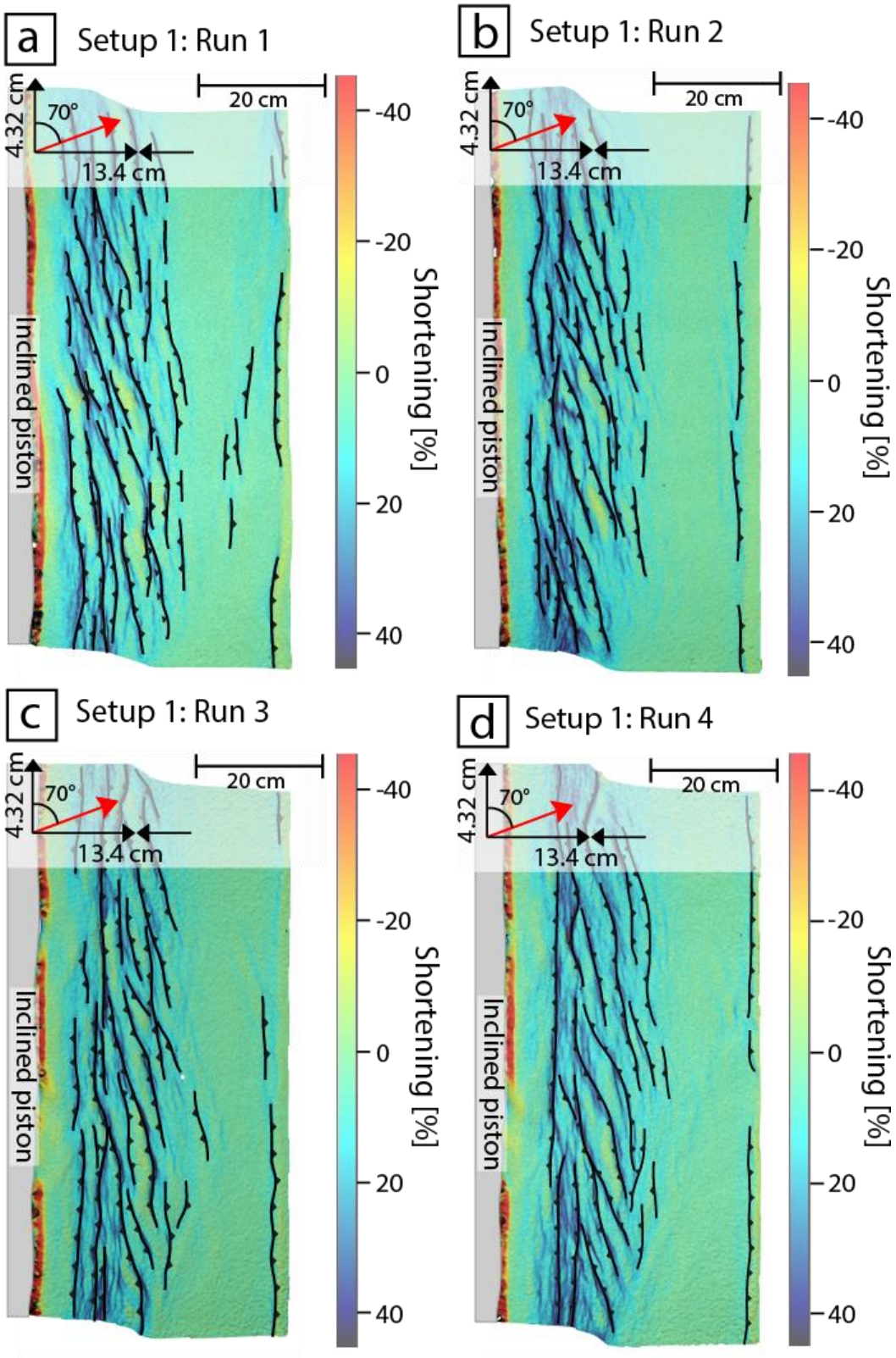

Supplementary figure S2: Cumulative divergence of all four setup 1 experimental runs after 80 minutes.

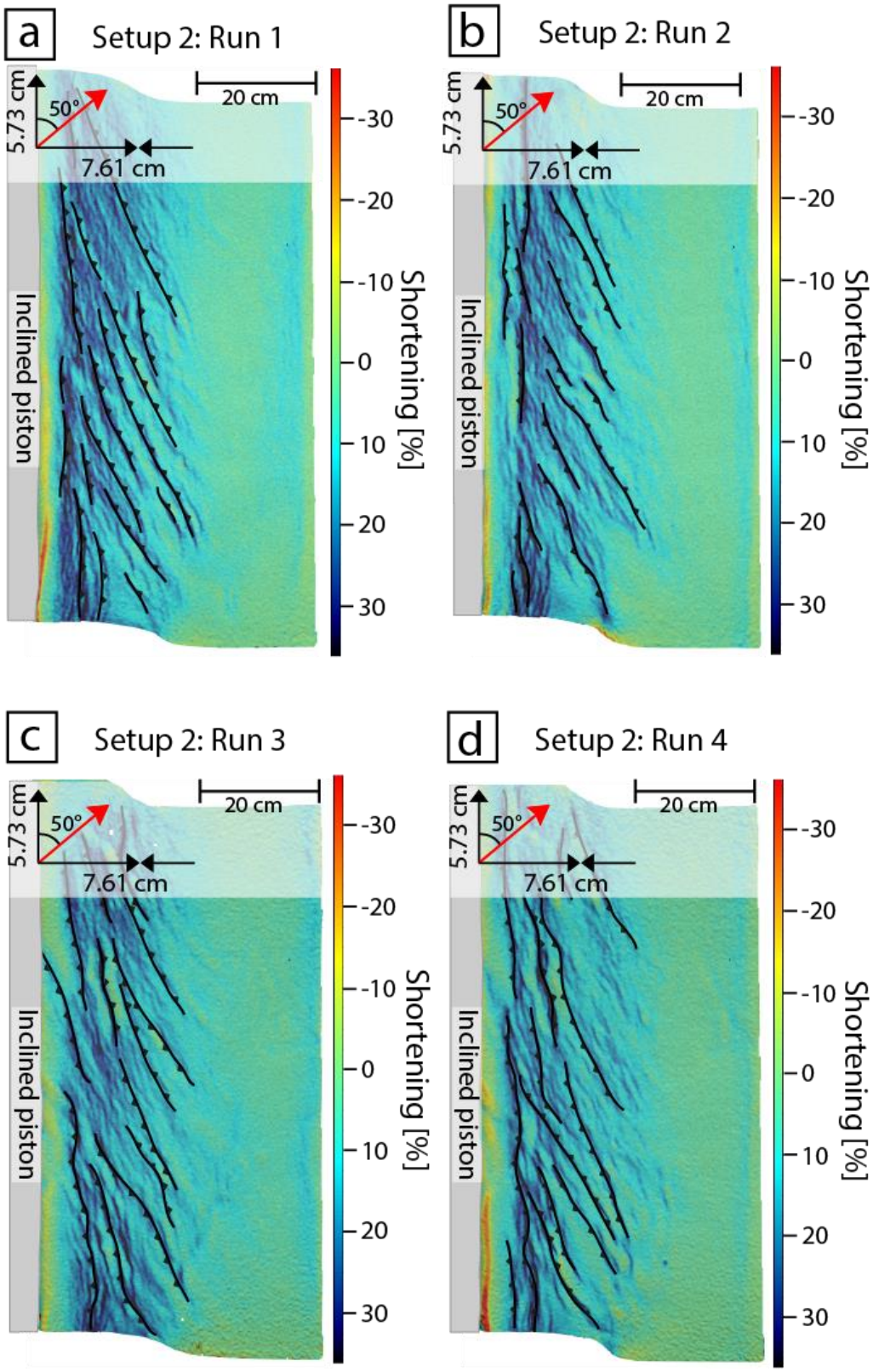

Supplementary figure S3: Cumulative shortening of all four setup 2 experimental runs after 54 minutes.

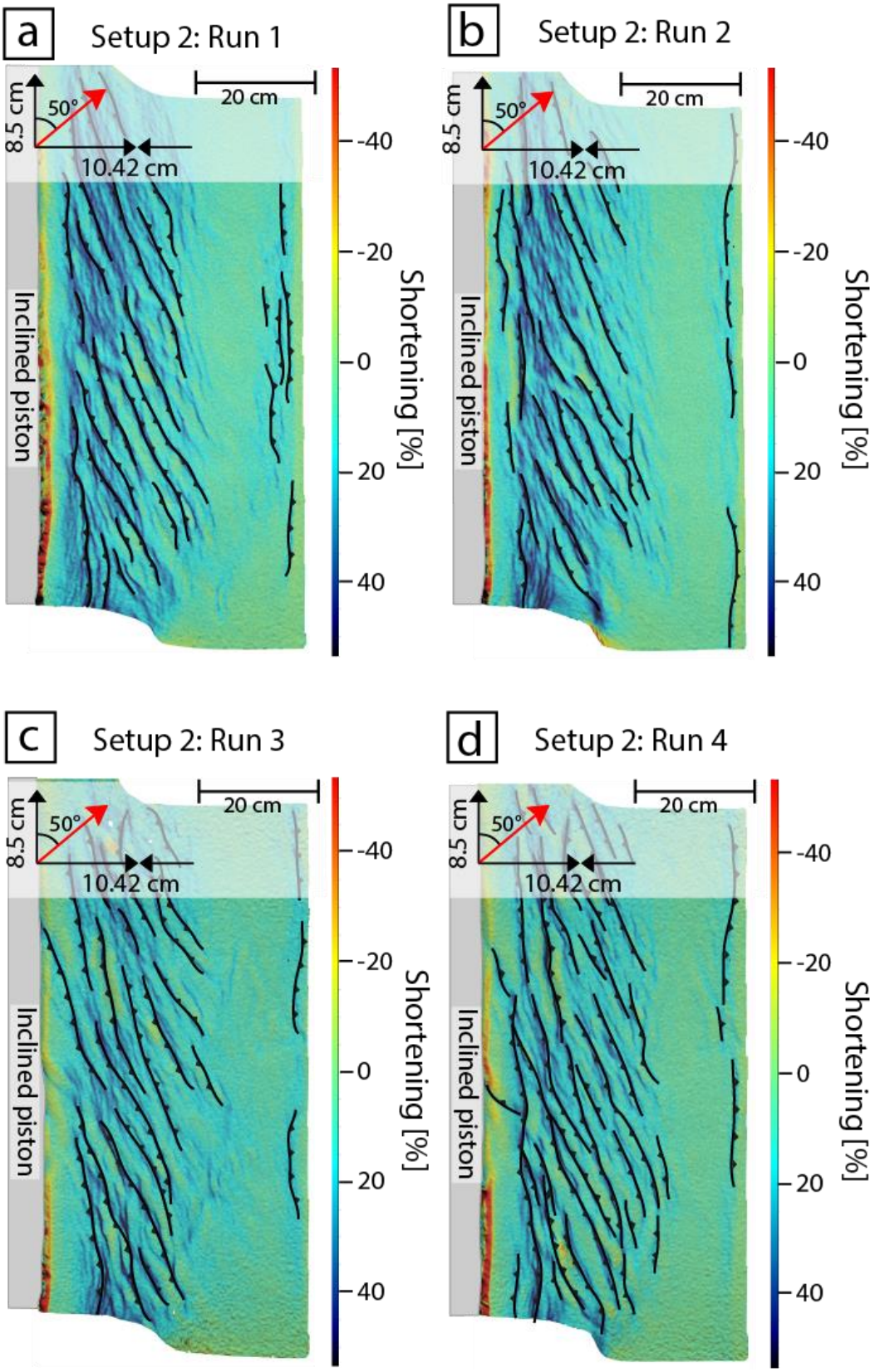

Supplementary figure S4: Cumulative shortening of all four setup 2 experimental runs after 80 minutes.

Versicherung an Eides statt

Affirmation on oath

Hiermit versichere ich an Eides statt, dass ich die vorliegende Dissertation mit dem Titel: „*Kinematic partitioning of deformation in the Southern Andes inferred from remote sensing, thermochronology, scaled analogue modelling, and field observations*“ selbstständig verfasst und keine anderen als die angegebenen Hilfsmittel – insbesondere keine im Quellenverzeichnis nicht benannten Internet-Quellen – benutzt habe. Alle Stellen, die wörtlich oder sinngemäß aus Veröffentlichungen entnommen wurden, sind als solche kenntlich gemacht. Ich versichere weiterhin, dass ich die Dissertation oder Teile davon vorher weder im In- noch im Ausland in einem anderen Prüfungsverfahren eingereicht habe und die eingereichte schriftliche Fassung der auf dem elektronischen Speichermedium entspricht.

I hereby declare an oath that I have written the present dissertation on my own with the title: "Kinematic partitioning of deformation in the Southern Andes inferred from remote sensing, thermochronology, scaled analogue modelling, and field observations" and have not used other than the acknowledge resources and aids. All passages taken literally or analogously from other publications are identified as such. I further declare that this thesis has not been submitted to any other German or foreign examination board and that the submitted written version corresponds to that on the electronic repository.

Hamburg, 08.02.2021 P. Göllner

Ort, Datum Unterschrift

Type set in: „TheSans UHH“ / LucasFonts